

# **Neuromorphological interpretation of clinical outcome**

Simon Fischer and Peter Skovgaard Nielsen

Kongens Lyngby 2007

Technical University of Denmark  
Informatics and Mathematical Modelling  
Building 321, DK-2800 Kongens Lyngby, Denmark  
Phone +45 45253351, Fax +45 45882673  
[reception@imm.dtu.dk](mailto:reception@imm.dtu.dk)  
[www.imm.dtu.dk](http://www.imm.dtu.dk)

# Summary

---

The purpose of this project is to investigate the possibility of analyzing the image data from a pan-European study of the elderly using neuromorphometry. A description of the prevalent methods is given and their individual advantages and disadvantages are analyzed. On the basis of this analysis a relatively new method, tensor-based morphometry (TBM), which still has many unexplored properties, is selected for further investigation.

To facilitate TBM analysis two frameworks are suggested — one for cross-sectional analysis and one for longitudinal analysis. Both frameworks share certain components: Registration, metric extraction, and statistical analysis.

The properties of the registration that are desirable for respectively the cross-sectional and longitudinal studies are analyzed and an image registration is applied.

Metrics for analyzing the registration results are described and the properties of two metrics are investigated and the usefulness in different settings evaluated.

It is shown that some group differences are detectable using the described methods. The metrics are correlated with clinical data both cross-sectionally and longitudinally.

Through the results it is concluded that the proposed framework of methods is viable for neuromorphometry. Through the framework it is possible to detect both general atrophy and pathologies in single subjects and differences between subjects which can be correlated with clinical parameters.



# Resumé

---

Formålet med dette projekt er at undersøge muligheden for at analysere billed-data fra et pan-europæisk studie af ældre mennesker ved brug af neuromorfometri. I denne rapport, gives en beskrivelse af de fremherskende metoder og hver metodes fordele og ulemper analyseres. På baggrund af dette udvælges en relativt ny metode, tensor-baseret morfometri (TBM), til videre undersøgelser.

Til brug for TBM fremlægges to procedurer — en der kan bruges til kryds-sektionel analyse, og en der kan anvendes til longitudinel analyse. Begge procedurer har visse komponenter til fælles: Registrering, metrik-ekstraktion og statistisk analyse.

De egenskaber, der for registrering er ønskelige i forbindelse med henholdsvis kryds-sektionelle og longitudinelle studier analyseres og registrering udføres.

Metrikker til analyse af registreringsresultaterne beskrives og egenskaberne for to metrikker undersøges. Ydermere evalueres metrikkernes brugbarhed i forskellige sammenhænge.

Det vises, at gruppeforskelle kan detekteres ved brug af de beskrevne metoder. Metrikkerne korreleres med kliniske data, både kryds-sektionelt og longitudinelt.

Gennem resultaterne konkluderes det, at de fremlagte procedurer er anvendelige til neuromorfometri. Gennem procedurerne er det muligt at detektere både generel atrofi og patologier i enkelte individer, og forskelle imellem individer, som kan korreleres med kliniske parametre.



# Preface

---

This thesis was prepared at Informatics Mathematical Modelling, the Technical University of Denmark in partial fulfillment of the requirements for acquiring the M.Sc. degree in engineering.

The thesis deals with tensor-based morphometry (TBM), a method for measuring differences and changes in the human brain. The main focus is on describing the methods used in TBM and carrying out an analysis of a data set using the methods.

Lyngby, August 2007

Simon Fischer and Peter Skovgaard Nielsen





# Acknowledgements

---

We would like to thank the researchers (especially Egill Rostrup and Charlotte Ryberg) at the DRCMR for providing the data for this thesis. Furthermore, we would like to thank our advisors, Rasmus Larsen and Karl Sjöstrand for providing answers for the questions we had through the project.



# Contents

---

<b>Summary</b>	<b>i</b>
<b>Resumé</b>	<b>iii</b>
<b>Preface</b>	<b>v</b>
<b>Acknowledgements</b>	<b>vii</b>
<b>1 Introduction</b>	<b>1</b>
1.1 Problem statement . . . . .	2
1.2 Structure . . . . .	2
<b>2 Background</b>	<b>3</b>
2.1 Magnetic Resonance Imaging . . . . .	3
2.2 Data . . . . .	7
2.3 Brain basics . . . . .	9

---

<b>3</b>	<b>Neuromorphometry</b>	<b>11</b>
3.1	Neuromorphometric methods . . . . .	11
3.2	Images . . . . .	16
3.3	Analysis frameworks . . . . .	16
3.4	Summary . . . . .	20
<b>4</b>	<b>Registration</b>	<b>21</b>
4.1	Global transformation . . . . .	21
4.2	Local transformation . . . . .	23
<b>5</b>	<b>Metric extraction</b>	<b>31</b>
5.1	The Jacobian matrix . . . . .	31
5.2	Relative volumes . . . . .	32
5.3	Log-Euclidean Metrics . . . . .	33
<b>6</b>	<b>Statistical analysis</b>	<b>35</b>
6.1	Principal component analysis . . . . .	35
6.2	Multivariate analysis of variance . . . . .	37
6.3	Correlation analysis . . . . .	40
6.4	Multiple regression . . . . .	40
<b>7</b>	<b>Results: Cross-sectional study</b>	<b>43</b>
7.1	Brain extraction . . . . .	43
7.2	Spatial normalization between subjects . . . . .	44

<b>CONTENTS</b>	<b>xi</b>
7.3 Metric extraction . . . . .	61
7.4 Statistical analysis . . . . .	63
7.5 Summary and discussion . . . . .	76
<b>8 Results: Longitudinal study</b>	<b>79</b>
8.1 Spatial normalization within subjects . . . . .	80
8.2 Metric extraction . . . . .	83
8.3 Statistical analysis . . . . .	90
8.4 Clinical correlation . . . . .	96
8.5 Discussion . . . . .	98
<b>9 Conclusion</b>	<b>101</b>
<b>A LADIS criteria</b>	<b>103</b>
A.1 Inclusion criteria . . . . .	103
A.2 Exclusion criteria . . . . .	103
<b>B Atlas images</b>	<b>105</b>
<b>C LPBA40 labels</b>	<b>109</b>
<b>D Cross-sectional correlations in the lobes</b>	<b>111</b>
<b>E Code listings</b>	<b>117</b>



## CHAPTER 1

# Introduction

---

Since the introduction of neuroimaging techniques (MR and CT) in the 1970s and 1980s an increasing number of studies have been made to investigate the wealth of data that these techniques produce. Along with improvements in imaging techniques, advances in computer technology have made increasingly complex analyses of the generated data possible.

An area of interest has been the study of the changes that occur in the human brain as we age and particularly the links between the physical pattern of aging and the pattern of cognitive decline and stability.

In 2000 a pan-European initiative was taken with the purpose of studying the aging population and their disabilities. The study, called Leukoaraiosis and Disability (LADIS), has the aim of evaluating Age-Related White Matter Changes (ARWMC), also called Leukoaraiosis, as an independent determinant of transition to disability in the elderly population.

Participants in the LADIS study undergo a series of examinations that include both clinical evaluations and MR scans.

## 1.1 Problem statement

One of the centers participating in the LADIS study is the Danish Research Centre for Magnetic Resonance (DRCMR). The DRCMR would like to investigate the possibility of analyzing the image data from the LADIS study using neuromorphometry to evaluate atrophy and pathologies and correlate the results with clinical measurements.

In this project, we examine the methods currently used for neuromorphometry, select a suitable method and apply it to the LADIS data with the objective of evaluating how well it is suited for measuring differences and changes in the brain and for correlation with clinical measurements. This is done both cross-sectionally and longitudinally.

## 1.2 Structure

This thesis will begin with some background information (chapter 2) summarizing the basics of MRI, a description of the data made available to us through the LADIS study, and a brief overview of brain anatomy.

An overview of the methods currently being used within the field of neuro-morphometry will be given, one method will be chosen (chapter 3) and theory behind it will be described in detail (chapters 4, 5). Following that the statistical analysis tools that are used will be described (chapter 6). After this the methods will be applied to the LADIS data set both cross-sectionally (chapter 7) and longitudinally (chapter 8) and the results will be discussed. The usefulness of TBM with regard to correlation with clinical data will be evaluated. A conclusion with a discussion of the obtained results concludes the thesis.

The appendix includes code listings (E).



# Background

---

To facilitate an understanding of the background of this project, this chapter briefly gives an overview of the basics of MRI, provides an overview of the LADIS data, and gives the reader an introduction to basic brain anatomy.

## 2.1 Magnetic Resonance Imaging

The imaging process used when acquiring magnetic resonance images is fairly complex. To get a better understanding of the process this section serves as a brief introduction to the subject. For a more in-depth discussion the reader is referred to [1].

### 2.1.1 Introduction

Magnetic resonance imaging (MRI) is a non-invasive imaging technique used primarily in medical settings to render images of the inside of the human body. The basis of the current MRI techniques was developed during the mid 1970s. In 1980 a demonstration of the imaging technique showed that a single image

could be acquired in approximately five minutes. During the following six years the imaging time was reduced to about five seconds.

One of the most obvious advantages of MRI and an important cofactor in its popularity is that no ionizing radiation is used. In contrast other non-invasive techniques like computed tomography (CT) and positron emission tomography (PET) involves exposure to ionizing radiation. With regard to neuroimaging, MRI's strength lies in the fact that it is well suited for distinguishing soft tissues.

### 2.1.2 Basic concept

When hydrogen nuclei are placed in a static magnetic field their spin axis is aligned with the magnetic field. The imaging process in MR works by exciting the nuclei to alter their spin axes and observe the time it takes for them to return to equilibrium. This makes the process especially well suited for imaging soft tissues which have high and varying water content.

### 2.1.3 Imaging hardware

When the image is acquired the subject is positioned in the center of a huge cylindrical magnet. An example of an MR scanner is shown in figure 2.1.



Figure 2.1: Siemens Magnetom Vision MR scanner

Besides the magnet the major components of an MR scanner is the gradient coil and the RF system.

### 2.1.4 Image properties

During the imaging process certain parameters, the echo time (TE) and the repetition time (TR), are chosen to alter the characteristics of the image. Two basic modes of operation result in the so-called  $T_1$ -weighted and  $T_2$ -weighted images. The main difference between the two lies in the contrast of the imaged tissue. Table 2.1 shows the values of TE and TR necessary to produce  $T_1$ - and  $T_2$ -weighted images.

Weighting	TR Value	TE Value
$T_1$	$\leq T_1$	$\ll T_2$
$T_2$	$\gg T_1$	$\geq T_2$

Table 2.1: Necessary TR and TE conditions to produce weighted images

In the brain,  $T_1$ -weighting causes the nerve connections of white matter to appear bright, and the congregations of neurons of gray matter to appear less bright, while cerebrospinal fluid (CSF) appears dark. With  $T_2$ -weighting the appearance of the tissue types is reversed, but at the same time the contrast between white and gray matter is reduced.

### 2.1.5 Image artifacts

An image artifact is a feature in the image which is not present in the imaged subject. Image artifacts can be the result of both improper operation and a consequence of natural properties or processes of the human body. Table 2.2 summarizes the most frequent of these.

An example of image artifacts can be seen in figure 2.2.

Artifact	Cause
RF offset and quadrature ghost	Failure of the RF detection circuitry
RF noise	Failure of the RF shielding
$B_o$ inhomogeneity	Metal object distorting the $B_o$ field
Gradient	Failure in a magnetic field gradient
Susceptibility	Objects in the FOV with a higher or lower magnetic susceptibility
RF inhomogeneity	Failure or normal operation of RF coil, and metal in the anatomy
Motion	Movement of the imaged object during the sequence
Flow	Movement of body fluids during the sequence
Chemical shift	Large $B_o$ and chemical shift difference between tissues
Partial Volume	Large voxel size
Wrap around	Improperly chosen field of view
Gibbs ringing	Small image matrix and sharp signal discontinuities in an image

Table 2.2: Summary of the most frequent MRI artifacts.

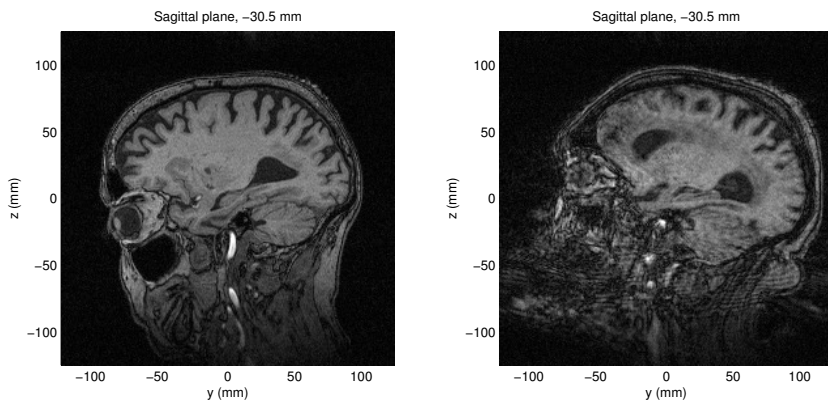


Figure 2.2: Example of artifacts in MR images: It can be seen that the noise from the image acquisition varies a lot. In the left image a clear difference between the white matter and the gray matter exists while the right image is very noisy making it difficult to distinguish between the two tissue types. In this case the artifact seems to be caused by motion of the subject during the image acquisition.

## 2.2 Data

The data for this project is provided by the Danish Research Centre for Magnetic Resonance (DRCMR). The DRCMR, located at Hvidovre Hospital near Copenhagen, is one of the twelve centres participating in the LADIS study.

The centre has examined 63 subjects of which 51 completed the whole study. All of the subjects have been followed over a period of three years with yearly clinical and functional assessments. Furthermore, at the initial and final examinations brain MR images are acquired.

The data provided to us by the DRCMR consists of MR images and clinical measurements from the Danish subjects. Because of drop-outs only partial data sets are available for some of the subjects.

The data represents a small subset of the entire LADIS set which contains 639 subjects.

### 2.2.1 MR images

The MR image data is composed of 50 images acquired at the initial examination (baseline images) and 27 images acquired at the final examination (followup images). All of the images are  $T_1$ -weighted MP-RAGE MR 3D brain scans with a spatial resolution of  $1 \times 0.997 \times 0.977 \text{ mm}^3$  resulting in images with  $150 \times 256 \times 256$  voxels (FOV =  $150 \times 250 \times 250 \text{ mm}^3$ ). The MR images were acquired on a 1.5 Tesla Siemens Magnetom Vision scanner used with TR = 13.5 ms, TE = 7.0 ms, TI = 100 ms, flip angle =  $15^\circ$ , and sagittal slice orientation.

Three 2D slices from a single 3D image volume can be seen in figure 2.3. The images are shown in the conventional way where the right hemisphere is pictured on the left side of the image and the left hemisphere on the right side. This is also the convention that is used in the rest of this thesis.

### 2.2.2 Clinical measurements

When the subjects are enrolled in the LADIS study a vast amount of clinical parameters are measured and recorded. These parameters can be split up into three categories:

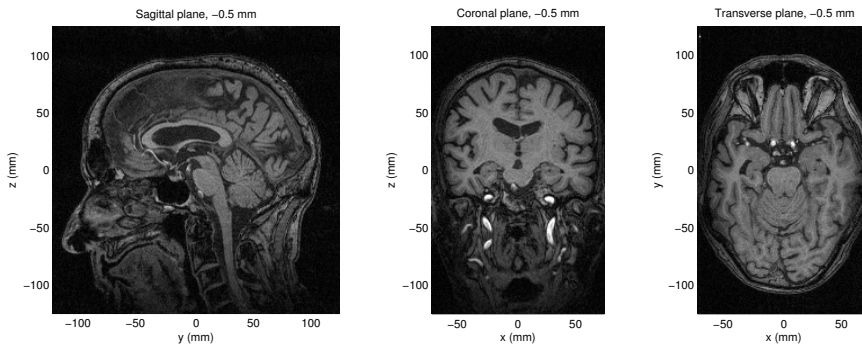


Figure 2.3: From left to right: Sagittal view, coronal view, transverse view.

- Personal data
- Historical data
- Functional and clinical evaluation

### 2.2.2.1 Personal data

The personal data recorded includes a range of parameters. Among these are age, sex, and race.

### 2.2.2.2 Historical data

Data is collected for determining the presence of the vascular risk factors and co-morbid conditions (e. g. heart failure, migraine, alcohol consumption, and cigarette smoking). The criteria for their definition and classification are listed in [2].

### 2.2.2.3 Functional and clinical evaluation

The functional and clinical parameters recorded include the following:

- *Standard vascular and neurologic examination*

- *Functional status:* Using the Instrumental Activities of Daily Living (IADL) scale.
- *Assessment of quality of life:* Using the Euro-QoL 5D
- *Cognitive assessment:* Mini-Mental State Examination (MMSE), Stroop test and Trail Making Test, part B.
- *Evaluation of mood/depression:* 15 item Geriatric Depression Scale (GDS-15), Cornell Scale for depression in Dementia, checklist for DSM-IV criteria for Major depressive episode, criteria for severity and psychotic features for current major depressive episode, criteria for melancholic features.
- *Motor assessment:* Using the Short Physical Performance Battery (SPPB) with slight modifications for evaluation of gait impairment in the elderly. In addition two very simple measurements for gait and balance will be performed.

## 2.3 Brain basics

Anatomically the human brain can be divided into three major areas: The hindbrain (rhombencephalon), the midbrain (mesencephalon), and the forebrain (prosencephalon). The hindbrain consists of the lower brain stem and cerebellum, the midbrain forms the upper brain stem and surrounding areas, while the forebrain, by far the largest part, consists of the two cerebral hemispheres (making up the cerebrum) that are connected by the corpus callosum. Figure 2.4 shows some of these structures.

The cerebrum consists mainly of the cerebral cortex (gray matter) and the interconnecting nerve strings (white matter). The brain is suspended in cerebrospinal fluid (CSF), a substance which is also found internally in the brain in the so-called ventricles. The cerebral cortex is made up of ridges (gyri) separated by furrows (sulci).

The cerebrum can be partitioned into four lobes: The frontal lobe, the parietal lobe, the occipital lobe, and the temporal lobe (see figure 2.5). To a degree, the lobes differ in which cognitive functions they perform.

The anatomy of brains from different subjects is on the large scale similar, but as more and more detailed views are taken, the differences that exist become clearer. This means that there does not necessarily exist a one to one correspondence between all structures in two different brains, but that the overall

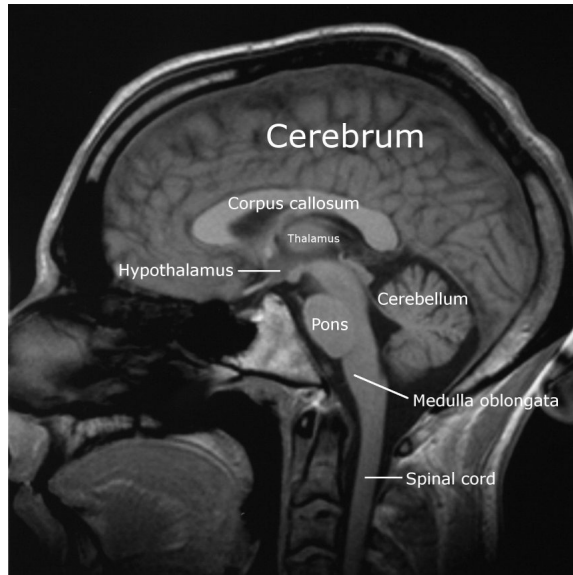


Figure 2.4: Areas of the human brain.

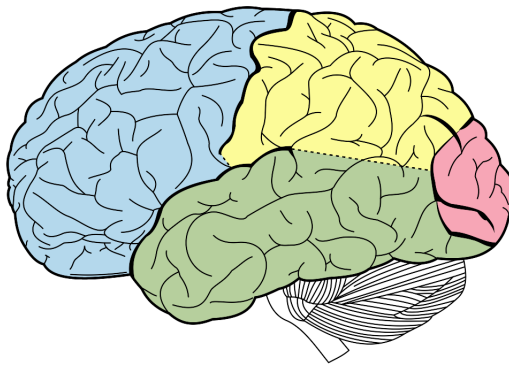


Figure 2.5: Lobes of the human cerebrum: Frontal lobe (blue), parietal lobe (yellow), occipital lobe (red), and temporal lobe (green).

structure is similar. For example, entities like the ventricles and deep sulci are found in all brains, while the finer (secondary and tertiary) sulci differ.



# Neuromorphometry

---

Morphometry, in general, is the measurement of shapes and forms. Within the field of neuroimaging, morphometry is applied to study both differences between and changes within subjects' brains.

In this chapter we explore the currently used methods within the field. The purpose of this is to choose a method that is suited for studying the LADIS data.

Once chosen, the method will be discussed in detail, and the specifics of our implementation will be described.

## 3.1 Neuromorphometric methods

Several methods for human neuromorphometry, both manual and automatic, are currently in use. The prevalent methods are:

- Model-based morphometry
- Voxel-based morphometry

- Deformation-based morphometry
- Tensor-based morphometry

Each method differs fundamentally from the others with regard to the data that they produce for further analysis.

### 3.1.1 Model-based morphometry

The idea behind model-based morphometry is to demarcate some region of interest and let further analysis be performed on the obtained model. Both manual and automatic approaches exist — the much used manual morphometry is an example of a model-based morphometric approach.

Manual morphometry (MM) is an extension into the digital realm of the classical direct measurement methods that have been in use since the 1920s. The basic idea is to let an expert annotate some area of interest within the brain. Often the annotation is done on separate 2D slices and gathered into a final 3D model. The obtained 3D model can then be analyzed.

The main strength in MM lies in the ability to directly utilize the knowledge and experience of the operator, thus eliminating the need for complex analysis tools.

Because of the nature of the method, however, MM can be very time consuming. Furthermore, because a human operator is involved, the reproducibility of results can be varying, especially if more than one operator is employed.

Due to this, MM is most often used to measure morphology of specific regions with limited size and clear boundaries, and as such is seldom used to measure global brain morphology.

MM has been applied in numerous studies, among these are studies of the hippocampus [3], infarctions [4], and the basal ganglia [5].

#### Summary:

- + Uses expert knowledge and experience directly
- + Comparatively simple to implement
- + Proven validity

- Very time consuming
- Suffers from inter- and intra-operator variability

Often used for studying limited structures with clear boundaries

### 3.1.2 Voxel-based morphometry

The basic idea behind voxel-based morphometry (VBM), introduced in 1995 [6], is to spatially normalize brain images (using both a linear and a low-dimensional non-linear warp), extract a tissue type of interest (e.g. gray matter), and apply some sort of smoothing. The result is an image that represents the concentration of the chosen tissue type in each voxel.

Because VBM is highly automated, it is practically possible to use for measuring global morphology. Another advantage is that reproducibility is increased because of the elimination of the human operator. Moreover, VBM has had time to mature and has proven its usefulness in a number of studies. It has also become increasingly fast.

A disadvantage to VBM is that it relies on the ability of a spatial normalization to map possibly fundamentally different brains into a common space. This is to some degree alleviated by smoothing and segmentation. Furthermore, the direct analysis of voxels makes VBM sensitive to changes in noise and imaging parameters [7].

Examples of the use of VBM are many. Among these are studies of both gray matter and white matter (e.g. [8]).

#### Summary:

- + Highly automated
- + Fast
- + Mature
- Needs a reliable spatial normalization algorithm to work
- Can be sensitive to noise and changes in imaging parameters

Often used for studying global morphology of certain tissue types

### 3.1.3 Deformation-based morphometry

The basic idea behind deformation-based morphometry (DBM) is to map a number of images (using both a linear and a high-dimensional non-linear warp) into a common space and let further analysis be performed on the resulting deformation fields.

One of the large advantages to DBM over VBM is that it allows analysis of shape and position of brain structures. Furthermore, as VBM it allows global analysis and is highly automated.

The fact that position is included in the result of DBM, can also be a disadvantage, however, because of the variability in general shape that exists within different brains. In some types of studies the position of structures is relevant while in others it is more useful only to measure size and shape. The speed of DBM also suffers from the need for computing a high-dimensional non-linear warp.

The inclusion of positional information has so far limited DBM's use. An example of a study using DBM can be found in [9].

#### Summary:

- + Highly automated
  - + Allows for analysis of the shape and position of brain structures
  - Includes possibly unwanted positional information
  - Slow
- Used for studying shape and position globally, regionally, or locally

### 3.1.4 Tensor-based morphometry

The basic idea behind tensor-based morphometry (TBM) is similar to that of DBM, except that the product used in further analysis is the spatial derivatives of the deformation field instead of the deformation field itself.

The advantage herein lies in the fact that information about shape and size can be extracted directly from the partial derivatives, without including information about position.

As with DBM, speed is also an issue for TBM, because of the need for computing a high-dimensional warp. The intermediate step of calculating spatial derivatives also requires additional computational resources — both processor time and memory.

TBM is still a relatively new technique compared to MM and VBM. This makes it especially interesting to investigate the properties of the method.

**Summary:**

- + Highly automated
- + Allows for analysis of the shape of brain structures
- + Removes positional information from analysis
- Slow
- Resource demanding

Comparatively new and untested

Used for studying shape globally, regionally, or locally

### 3.1.5 Summary

Each of the methods described above have their strengths and weaknesses. From our point of view, TBM is the most interesting of the methods, since the field of TBM is still relatively new and has potential to reveal properties of neuromorphology that are not possible to measure using the more traditional methods (manual morphometry and voxel-based morphometry).

For these reasons, TBM is the method we choose to apply to the LADIS data set.

## 3.2 Images

Before we proceed, it is useful to formalize a definition of what an image is. A three-dimensional image can be viewed as a mapping that assigns every spatial point  $(x, y, z)$  belonging to a compact set  $\Omega \subset \mathbb{R}^3$  a value  $I(x, y, z) \in \mathbb{R}$ .

For discrete images (such as MR images),  $\Omega \subset \mathbb{Z}^3$ . This set defines the *grid points* of the image. The collection of grid points forms a *grid*,  $\mathbf{G}$  (see figure 3.1). Each volume element  $I(x, y, z)$  is called a *voxel*.

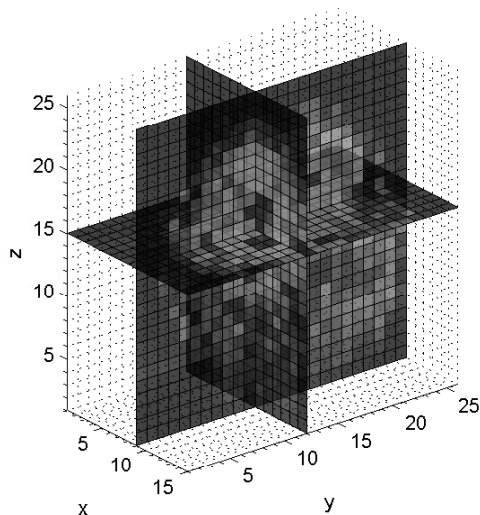


Figure 3.1: Image grid: Here  $x \in [1; 15]$ ,  $y \in [1; 26]$ , and  $z \in [1; 26]$ .  $I(x, y, z)$  is shown in three planes.

These definitions will be used throughout the rest of the text.

## 3.3 Analysis frameworks

For the purpose of the studies we wish to perform, TBM needs to be integrated into two larger analysis frameworks — one for cross-sectional analysis and one for longitudinal analysis.

### 3.3.1 Cross-sectional analysis

The purpose of a cross-sectional analysis is to evaluate differences between subjects. The framework for the cross-sectional analysis consists of several steps:

1. Brain extraction on baseline images.
2. Spatial normalization of baseline images to a common reference.
3. Metric extraction from the results from 2.
4. Statistical analysis of results.

#### 3.3.1.1 Brain extraction

To avoid influence from both the highly deformable soft tissue areas around the brain and the skull, the part of the image that contains the brain needs to be extracted from the rest of the image.

In this project we use the approach described in [10]. The process involves several steps including filtering and segmentation. A detailed description of the techniques used lies beyond the scope of this thesis. The used implementation is found in the software package called BrainSuite2.

The result of the brain extraction procedure is an image volume where everything but the cerebral white matter, gray matter and internal cerebrospinal fluid has been masked out.

#### 3.3.1.2 Spatial normalization

Spatial normalization is the process of mapping objects into a reference frame such that features in one object (to some feature level) are aligned with the corresponding features in the other objects.

Spatial normalization can be achieved by choosing a target object, finding a transformation that maps one source object into the target object, and repeating this for all of the objects.

In image analysis, finding a transformation that maps one image into another is called registration. Formalized, the registration problem can be stated as finding

a transformation  $\mathbf{T}(\mathbf{G}) : \mathbb{Z}^3 \mapsto \mathbb{Z}^3$  of the image grid, that maps every feature in a source image  $I_{source}$  into the corresponding features in a target image  $I_{target}$  such that

$$I_{target}(x, y, z) \sim I_{source}(\mathbf{T}(x, y, z)).$$

The degree to which the images should be registered is decided by the intended use of the result. The choice of this degree decides where information about the difference between the images is stored: In the images or in the transformation. At the extremes are two cases:

- $\mathbf{T}$  is the identity transformation and all difference information is stored in the images.
- $\mathbf{T}$  establishes a one to one correspondence between all image elements and all difference information is stored in the transformation.

In between these two extremes lie the registrations that are most often applied for actual analysis. Examples are registrations that account only for global movement (translation and rotation) and registrations that account for limited plastic differences.

For cross-sectional tensor-based morphometry, it would seem most useful to achieve a one to one correspondence between the images, since TBM involves analyzing the transformation. In practice, however, this is not the case, both because of the variability that exists between individual brains and because of image artifacts such as noise.

A plethora of registration techniques exist. In chapter 4 a detailed description of the methods we use for solving the registration problem for TBM is given.

For the three-dimensional registration problem solved in this project, the resulting transformation  $\mathbf{T}$  is a three-dimensional vector valued function over the image volume.

### 3.3.1.3 Metric extraction

Having found an optimal (in a sense that pertains to TBM) registration, analysis of the resulting transformation  $\mathbf{T}$  can proceed.

For TBM this analysis requires calculation of the spatial derivative matrix of



T. This is also called the Jacobian matrix  $\mathbf{J}$ , and is defined as

$$\mathbf{J} = \begin{bmatrix} \frac{\partial T_x}{\partial x} & \frac{\partial T_x}{\partial y} & \frac{\partial T_x}{\partial z} \\ \frac{\partial T_y}{\partial x} & \frac{\partial T_y}{\partial y} & \frac{\partial T_y}{\partial z} \\ \frac{\partial T_z}{\partial x} & \frac{\partial T_z}{\partial y} & \frac{\partial T_z}{\partial z} \end{bmatrix}$$

In practice using the Jacobian matrix directly is not feasible because it contains information that is not easily interpretable. Instead of using the Jacobian matrix directly, measures deriving from it are often used. These derivatives can be simple, for example encoding only relative volume change, or more complex, containing information about directional changes etc.

In chapter 5 a more detailed description of how we choose to extract metrics from the Jacobian matrix is given.

The result of the calculations is a tensor field over the image volume that incorporates shape information.

### 3.3.1.4 Statistical analysis

When the desired information has been extracted from the transformation, statistical analysis of the data can proceed. The goals of the statistical analysis can be manifold. Examples are analyses pertaining to the significance of detected differences and building models that relate external factors (such as age) to the differences.

There are many possible methods that can be used for the statistical analysis of the tensor fields. These include establishing parametric maps, point-wise regression and use of the general linear model.

In chapter 6 a description of the methods we use is given.

## 3.3.2 Longitudinal analysis

The second type of analysis is a longitudinal analysis where changes within subjects are evaluated. Compared to the cross-sectional analysis, the framework is somewhat more complicated:

1. Brain extraction on baseline images.

2. Spatial normalization of baseline images to a common reference.
3. Spatial normalization of followup images to their corresponding baseline image.
4. Transformation of the result from 3 into a common reference space using the results from 2.
5. Calculation of spatial derivatives (or measures derived from them) of the results from 4.
6. Statistical analysis of results.

To remove the effect that cross-sectional variability has on the longitudinal analysis, the transformation from the cross-sectional analysis is reused in step 4.

The methods used in each of the steps are the same as described for the cross-sectional analysis.

### 3.4 Summary

In this chapter we have introduced a number of methods used in neuromorphometry, introduced key concepts, and selected a method (tensor-based morphometry) for neuromorphometry that we will investigate. We have presented two frameworks — one that will be used for a cross-sectional analysis and one that will be used for a longitudinal analysis.

In the following chapters, the theory of the most important items in these frameworks will be described. These items are

- Registration
- Metric extraction
- Statistical analysis

# Registration

---

As described in chapter 3, to perform a registration is to solve the problem of finding a transformation that maps a set of features in one image into the corresponding features in another image.

The transformation  $\mathbf{T} : (x, y, z) \mapsto (x', y', z')$  which maps any point in the source image  $I_{source}$  into its corresponding point in the target image  $I_{target}$  is often viewed as a combination of a global transformation and a local transformation:

$$\mathbf{T}(x, y, z) = \mathbf{T}_{global}(x, y, z) + \mathbf{T}_{local}(x, y, z).$$

The two kinds of transformations will be described in the following sections.

## 4.1 Global transformation

The global transformation describes the overall transformation of the image and can be modelled as a combination of several linear transformations: Translation, rotation, scaling and shearing.

If the transformation is described only by a translation and a rotation, it is called a rigid transformation and can be parameterized with 6 degrees of freedom (3 translations and 3 rotations).

A more general transformation is the affine transformation which also includes scaling and shearing. The affine transformation is parameterized by 12 degrees of freedom (rigid, 3 scalings, and 3 shears). For a point in three-dimensional space written in homogeneous coordinates, the affine transformation can be written as a matrix:

$$\mathbf{T}_{\text{global\_affine}}(x, y, z) = \begin{bmatrix} a_{xx} & a_{xy} & a_{xz} & a_{xw} \\ a_{yx} & a_{yy} & a_{yz} & a_{yw} \\ a_{zx} & a_{zy} & a_{zz} & a_{zw} \\ 0 & 0 & 0 & 1 \end{bmatrix} \cdot \begin{bmatrix} x \\ y \\ z \\ 1 \end{bmatrix}$$

An example of a global registration can be seen in figure 4.1. Details about the global registration are found in [11].

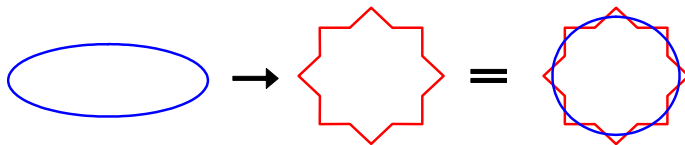


Figure 4.1: Example of a global transformation in 2D. The blue ellipse is registered to the red star. After the transformation the two shapes are aligned within the limits of an affine transformation.

## 4.2 Local transformation

The global transformation only accounts for differences in position, rotation, scale, and shear (see figure 4.1). To model the more local differences between images a free-form deformation (FFD), which is a local non-rigid transformation, is needed. Usually a FFD is represented by a three-dimensional deformable grid. Examples of 2D FFDs can be seen in figure 4.2.

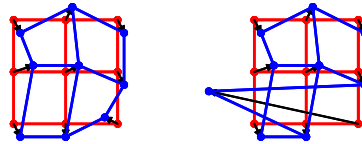


Figure 4.2: Example of free-form deformations in 2D. The left FFD is well-behaved while the right FFD appears to be in need of some constraints.

As figure 4.2 shows, FFDs often need behavioral restrictions or *regularization* as it is called. As image registration is an ill-posed problem [12], the need for regularization is twofold: To make the problem more well-posed and to make sure that the deformation is reasonable in a sense pertaining to the registration problem at hand. Over the time a range of regularized FFDs have been proposed:

- Elastic registration
- Fluid registration
- Diffuse registration
- Curvature registration

All of these regularized registrations are based on physical models that may or may not be related to the actual changes that take place in the human brain. So as not to limit the deformation to a physical model we choose to use a parametric registration which is implicitly regularized. This FFD is based on the tensor product B-spline approach proposed in [13] and [14].

### 4.2.1 B-splines

Before we describe what a tensor product B-spline is, it is useful to know some of the desirable properties (in the context of image registration) of the cubic

B-spline. The most important of these are [15]:

**$C^2$  continuity:** With knot multiplicity 1, it is guaranteed that the curve is  $C^2$  continuous in every point, which ensures smoothness and differentiability (the red curve in figure 4.3).

**Strong convex hull property:** The curve lies within the convex hull of the defining control points. This ensures better control of the curve and thereby better regularization (the shaded area in figure 4.3).

**Variation diminishing property:** No straight line intersects a B-spline curve more times than it intersects the curve's control poly-line. This prevents oscillations and thus gives better regularization (the green line in figure 4.3).

**Local modification property:** When a control point is changed the curve is only locally modified (illustrated in figure 4.4).

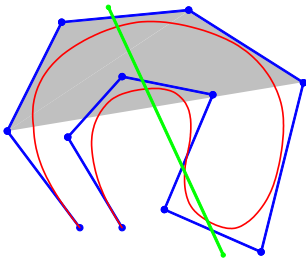


Figure 4.3: Example of a cubic B-spline. The blue connected points are the control points of the B-spline while the red curve is the corresponding B-spline. The shaded area depicts the strong convex hull property and the green line shows the variation diminishing property.

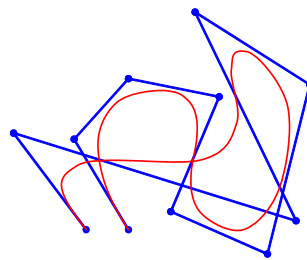


Figure 4.4: Same B-spline as figure 4.3 except that one control point is moved. Notice that the B-spline is only locally modified.

The idea is to deform the 3D image volume by manipulating an underlying 3D mesh of control points for a so-called tensor-product B-spline. Let  $\phi_{i,j,k}$  define the  $(n_x, n_y, n_z)$  mesh of control points,  $\Phi$ , with spacing  $(\delta_x, \delta_y, \delta_z)$ . Then the local

transformation can be written as the 3D tensor product of 1D cubic B-splines:

$$\mathbf{T}_{\text{local}}(x, y, z) = \sum_{l=0}^3 \sum_{m=0}^3 \sum_{n=0}^3 B_l(u)B_m(v)B_n(w)\phi_{i+l}\phi_{j+m}\phi_{k+n},$$

where  $i = \lfloor x/\delta_x \rfloor - 1$ ,  $j = \lfloor y/\delta_y \rfloor - 1$ ,  $k = \lfloor z/\delta_z \rfloor - 1$ ,  $u = x/\delta_x - i + 1$ ,  $v = y/\delta_y - j + 1$ ,  $w = z/\delta_z - k + 1$  and where  $B_l$  represent the  $l$ th basis function of the B-spline:

$$\begin{aligned} B_0(u) &= (1-u)^3/6 \\ B_1(u) &= (3u^3 - 6u^2 + 4)/6 \\ B_2(u) &= (-3u^3 + 3u^2 + 3u + 1)/6 \\ B_3(u) &= u^3/6 \end{aligned}$$

An additional advantage of using this representation is that the derivatives of the transformation are easily found simply by using the derivatives of the basis functions in the evaluation of the B-splines:

$$\begin{aligned} B'_0(u) &= -(1-u)^2/2 \\ B'_1(u) &= (9u^2 - 12u)/6 \\ B'_2(u) &= (-9u^2 + 6u + 3)/6 \\ B'_3(u) &= u^2/2 \end{aligned}$$

### 4.2.2 Multilevel

The spacing of the control points in the 3D mesh  $\Phi$  regulates the level at which the deformation takes place. A large control point spacing results in globally non-rigid deformations while a dense control point mesh allows modelling of very local deformations. By using a multilevel approach in which the resolution of the control point mesh is increased we are thereby able to model both global and more local differences.

The multiple resolutions of the control point mesh can be achieved in different ways. One way is to start with a coarse mesh and subdivide it using appropriate B-spline subdivision techniques, as described in [16]. Another approach is to use a hierarchy  $(\Phi^1, \dots, \Phi^L)$  of local deformation meshes as described in [17]. Multiresolution registration using this method is achieved by sequentially finding the best local transformation,  $\mathbf{T}_{\text{local}}^l$ , at each resolution level  $l$ , taking into account the deformations found for coarser resolution levels. The final control

point mesh and the associated local transformation is in this way given by the sum of local transformations:

$$\mathbf{T}_{\text{local}}(x, y, z) = \sum_{l=1}^L \mathbf{T}_{\text{local}}^l(x, y, z)$$

Figure 4.5 shows the advantage of using multiresolution meshes. FFDs using a single mesh resolution are locally not sufficiently pliant at low resolutions, while they are badly regularized at higher resolutions [14].

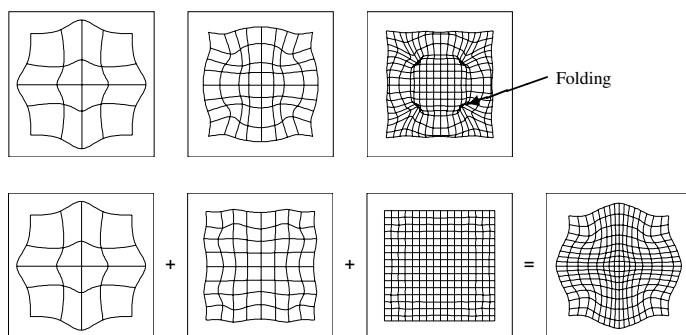


Figure 4.5: 2D slices from 3D FFDs. The top pictures shows modelling using single mesh resolution while the bottom pictures shows the corresponding modelling using multiresolution meshes.

In the optimization of the control points in order to maximize the two images' similarities a vast amount of local minima exist. To set the focus on the essential minima, a multilevel approach is also used with the image resolution in a coarse-to-fine fashion. This will also yield a better regularization of the FFD. In figure 4.6 the multilevel approach of the image resolution is illustrated.



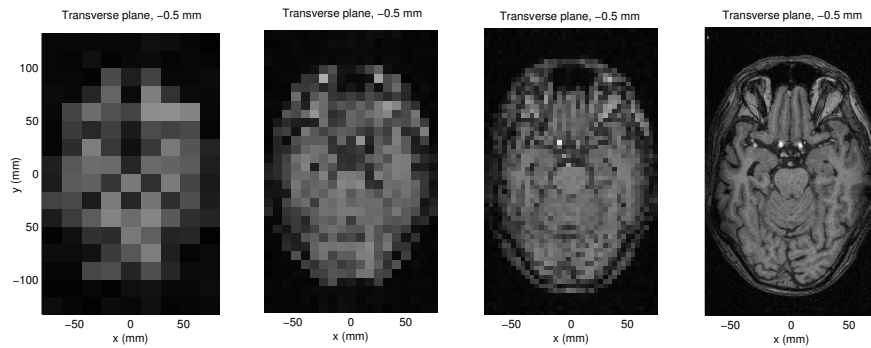


Figure 4.6: Transverse slices of the image volume. The image resolution is increased from left to right.

### 4.2.3 Cost function

To find the optimal control point grid  $\Phi$  it is necessary to define a similarity measure to compare the images with. Several types of similarity measures have been proposed over the time:

- Sum of squared differences (SSD)
- Correlation coefficient (CC)
- Mutual information (MI)
- Normalized mutual information (NMI)

A description of each of these and how to calculate them can be found in [18]. The purpose of the similarity measure is to evaluate how alike two images are.

In addition to the similarity measure it is reasonable to include a penalty term in the cost function. The reason for doing this is to allow control of the behavior of the FFD in such a way that it is adaptable to various contextual requirements. If prior knowledge exists about the deformation which is to be modelled, the transformation can be regularized by introducing a penalty term. The desired properties of the FFD could be:

- Smoothness
- Volume preservation
- Topology preservation

The smoothness penalty can be introduced by computing the bending energy of the 3D tensor product B-spline, while the volume and topology preservation penalties use the Jacobian determinant in the penalty term. The penalty term,  $\mathcal{P}$ , for each of these are:

*Smoothness:*

$$\mathcal{P}_{smooth} = \frac{1}{V} \int_0^X \int_0^Y \int_0^Z \left[ \left( \frac{\partial^2 \mathbf{T}}{\partial x^2} \right)^2 + \left( \frac{\partial^2 \mathbf{T}}{\partial y^2} \right)^2 + \left( \frac{\partial^2 \mathbf{T}}{\partial z^2} \right)^2 + 2 \left( \frac{\partial^2 \mathbf{T}}{\partial xy} \right)^2 + 2 \left( \frac{\partial^2 \mathbf{T}}{\partial xz} \right)^2 + 2 \left( \frac{\partial^2 \mathbf{T}}{\partial yz} \right)^2 \right] dx dy dz,$$

where  $V$  denotes the volume of the image domain.

*Volume preservation:*

$$\mathcal{P}_{vol} = \sum_{x=0}^X \sum_{y=0}^Y \sum_{z=0}^Z \text{abs}(\log(\det(\mathbf{J}(\mathbf{T}(x, y, z))))))$$

where  $\mathbf{J}$  is the Jacobian matrix a defined in section 3.3.1.3 on page 19.

*Topology preservation:*

$$\mathcal{P}_{top} = \sum_{x=0}^X \sum_{y=0}^Y \sum_{z=0}^Z \mathcal{F}(x, y, z),$$

where

$$\mathcal{F} = \begin{cases} 10\mathcal{J}^2 + 0.1\mathcal{J}^2 - 2 & \text{if } \mathcal{J} < 0.3 \\ 0 & \text{else,} \end{cases}$$

where

$$\mathcal{J} = \det(\mathbf{J}(\mathbf{T}(x, y, z))).$$

By combining the similarity measure with the regularizing penalty term the final cost function,  $\mathcal{C}$ , is obtained:

$$\mathcal{C} = -\text{Similarity}(I_{target}, I_{source}(\mathbf{T}(\mathbf{G}))) + \lambda_1 \mathcal{P}_{smooth} + \lambda_2 \mathcal{P}_{vol} + \lambda_3 \mathcal{P}_{top}.$$

The optimal local transformation is now found by minimizing the cost function. The minimization of the cost function is a combination of maximizing the similarity between the two images while still fulfilling the desired transformation property requirements. The weighting factors  $(\lambda_1, \lambda_2, \lambda_3)$  define the tradeoff between the two competing goals. Finding this optimum can be done using numerical optimization methods (such as gradient descent). A discussion of these methods lies beyond the scope of this thesis — the reader is referred to for example [19] for more information.

#### 4.2.4 Pseudocode

The pseudocode for the registration can now be sketched. If  $I_{RES}$  is the image resolution,  $\Phi$  the control point mesh,  $\Phi_{RES}$  the resolution of the control point mesh, and  $\mathcal{C}$  is the cost function, then the pseudocode can be written as:

```
DEFINE  $I_{RES,max}$ 
DEFINE  $\Phi_{RES,max}$ 
SET  $I_{RES}$  to  $I_{RES,min}$ 
SET  $\Phi_{RES}$  to  $\Phi_{RES,min}$ 
WHILE  $\Phi_{RES} \leq \Phi_{RES,max}$ 
  WHILE  $I_{RES} \leq I_{RES,max}$ 
    optimize  $\Phi$  to minimize  $\mathcal{C}$ 
    increase  $I_{RES}$ 
  END WHILE
  increase  $\Phi_{RES}$ 
END WHILE
```

The optimization of the global transformation and of the control point mesh defining the tensor-product B-spline as described above has been implemented by Daniel Rueckert in the Image Registration Toolkit (ITK), used under license from Ixico Ltd. Following the registration of the two images, ITK outputs the optimized control point mesh into a file.

# Metric extraction

---

As described in chapter 3, the goal of tensor-based morphometry is to extract metrics that describe differences and changes in shape. In this chapter we describe two methods that can be used for extracting information about shape from a transformation.

## 5.1 The Jacobian matrix

The measures used in TBM all derive from the spatial derivatives of the transformation, the Jacobian matrix (as described in chapter 3). To reiterate, the Jacobian  $\mathbf{J}$  matrix of a three-dimensional transformation  $\mathbf{T}$  is defined by

$$\mathbf{J} = \begin{bmatrix} \frac{\partial T_x}{\partial x} & \frac{\partial T_x}{\partial y} & \frac{\partial T_x}{\partial z} \\ \frac{\partial T_y}{\partial x} & \frac{\partial T_y}{\partial y} & \frac{\partial T_y}{\partial z} \\ \frac{\partial T_z}{\partial x} & \frac{\partial T_z}{\partial y} & \frac{\partial T_z}{\partial z} \end{bmatrix}$$

The operation of calculating the Jacobian matrix  $\mathbf{J}$  of a transformation  $\mathbf{T}$  is denoted  $\mathbf{J} = \mathcal{J}(\mathbf{T})$ .

Given the transformation  $\mathbf{T}$ , that has been found as described in chapter 4, both local shape and orientation is encoded in  $\mathbf{J}$  [20]. If we want to discount

the orientation information, we can instead use only the Jacobian of the local transformation  $\mathbf{T}_{\text{local}}$  described in section 4.2.

$\mathbf{T}_{\text{local}}$  is represented entirely by a tensor product B-spline. Using this representation of the local transformation gives us the advantage of being able to calculate the Jacobian exactly according to the equations given in section 4.2.1. The calculation of derivatives is implemented in the Matlab and C-functions `tb spline3` and `tb spline3c` (see appendix E, page 133).

Although information about shape can be found in the Jacobian, it is often not sensible to use the Jacobian directly. The reason for this is that the Jacobian is not very intuitive to interpret. Instead, measures deriving from the Jacobian are used.

In this thesis we study two measures:

- Relative volumes
- Log-Euclidean metrics

## 5.2 Relative volumes

An intuitive way of representing shape information is to consider only relative volumes. Relative volumes can be represented by

$$V_{\text{relative}} = \det(\mathbf{J} + I)$$

where  $I$  is a  $3 \times 3$  identity matrix. Adding the identity matrix is done to ensure that an identity deformation has  $V_{\text{relative}} = 1$ . If  $V_{\text{relative}} > 1$ , the volume of the source is larger than the target and vice versa for  $V_{\text{relative}} < 1$ . If  $V_{\text{relative}} < 0$ , the transformation has folded, resulting in a “negative” volume.

An advantage of using relative volumes is that they condense the information in the Jacobian matrix to an easily interpretable single value, thus making further analysis univariate.

The disadvantage of using the relative volumes is that much of the information contained within the Jacobian matrix is discarded in the calculation. Only the magnitude of the expansion or contraction is studied, while the anisotropy and directional components are disregarded. For example, volume-preserving deformations may not be recorded at all. As a very simple example of how

much of the shape information is lost when calculating the relative volume, the case where the eigenvalues of the  $\mathbf{J} + I$  are  $\lambda_{1,2,3} = \{1, 2, 0.5\}$  is considered. In this case the determinant of the matrix is 1, although the eigenvalues clearly indicate shape change.

The extraction of the relative volume metric is implemented in the Matlab-functions `detconvertinter` and `detconvert` (see appendix E, pages ?? and ??).

### 5.3 Log-Euclidean Metrics

In [21] and [22] a new method for TBM involving multivariate statistics on Log-Euclidean transformed strain matrices is described. The strain matrix used in this method is the right stretch tensor:

$$S = (J^T J)^{\frac{1}{2}}$$

where  $(M)^{\frac{1}{2}}$  denotes the matrix square root of the matrix  $M$ . For smooth transformations, however, the strain matrices are constrained to the space of positive definite matrices. This space does not form a vector space but a cone in the space of matrices.

This means that ordinary multivariate statistical quantities such as the mean can not be derived directly from the strain matrices. The statistical quantities have to be constrained to lie on the manifold as well. The solution to this is to transform to strain matrices from the manifold into a vector space. This Log-Euclidean transformation can be obtained using the Hencky tensor, which has many desirable properties [20]:

$$S_{LE} = \log(S),$$

where  $\log$  is the matrix logarithm. As  $S_{LE}$  in our case is a symmetric  $3 \times 3$  matrix it has six unique elements. To simplify the further computations, the matrices with six degrees of freedom can be represented as vectors with six elements:

$$\vec{S}_{LE} = (S_{LE_{1,1}}, S_{LE_{2,2}}, S_{LE_{3,3}}, \sqrt{2}S_{LE_{1,2}}, \sqrt{2}S_{LE_{1,3}}, \sqrt{2}S_{LE_{2,3}})$$

Now ordinary multivariate statistics can be used directly on these vectors to model their means and also their distribution about the mean using the covariance matrix. The calculation of Log-Euclidean metrics is implemented in the Matlab-functions `leconvert` and `leconvertinter` (see appendix E, pages ?? and ??).





## CHAPTER 6

# Statistical analysis

---

In this chapter we present a number of statistical analysis methods that will be used to analyze the TBM data. The reader is expected to be familiar with the basic concepts of uni- and multivariate statistics.

The methods that are introduced have different purposes, from dimensionality reduction, over differentiation between groups, to modelling.

## 6.1 Principal component analysis

Principal component analysis (PCA) is a technique that can be used to reduce the dimensionality of multivariate data. PCA transforms data to a new coordinate system where the greatest variance in the data comes to lie on the first axis (the first principal component), the second greatest variance on the second axis, and so on (see figure [6.1](#)).

By finding this transformation, pruning out the least explaining components, and transforming the data with it, the dimensionality of data can be reduced.

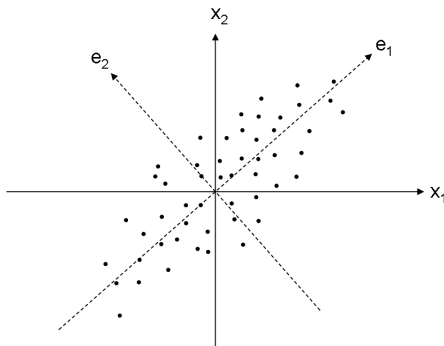


Figure 6.1: An example of PCA.  $\mathbf{e}_1$  and  $\mathbf{e}_2$  form the basis of the transformed coordinate system.

### 6.1.1 Definition

For a multidimensional, stochastic variable

$$\mathbf{X} = \begin{pmatrix} X_1 \\ \vdots \\ X_k \end{pmatrix}$$

with the covariance matrix  $\Sigma$  we can find the eigenvalues  $\lambda_1 \geq \dots \geq \lambda_k$  of  $\Sigma$  with the corresponding eigenvectors  $\mathbf{p}_1, \dots, \mathbf{p}_k$ . The  $i$ th principal axis of  $\mathbf{X}$  is then the direction of  $\mathbf{p}_i$  corresponding to the  $i$ th largest eigenvalue, while the  $i$ th principal component of  $\mathbf{X}$  is  $\mathbf{X}$ 's projection  $\mathbf{Y}_i = \mathbf{p}_i' \mathbf{X}$  onto the  $i$ th principal axis.

The principal components are uncorrelated and the variance of the  $i$ th component is  $\lambda_i$ . Furthermore, the sum of the variance of the principal components is equal to that of the original variables.

The first principal component is the linear combination of the original variables with the largest variance and the  $i$ th principal component is the linear combination of the original variables that is uncorrelated with the  $i - 1$  first principal components with the largest variance.

From this it is clear that if we want to reduce the original variables so that at least  $V$  of the variance is accounted for, we can select the  $m$  first principal components such that

$$\frac{\lambda_1 + \dots + \lambda_m}{\lambda_1 + \dots + \lambda_m + \dots + \lambda_i} \geq V$$

and project the original variables onto these components. This gives a new set of observations, each with  $m$  variables.

## 6.2 Multivariate analysis of variance

In general, the purpose of analysis of variance (ANOVA) is to test for significant differences between means of groups. It is often used to test whether one group differs significantly from another with regard to a variable. When analyzing multivariate data, using several ANOVA tests, one for each dependant variable, can lead to problems. First, the dependant variables are likely to be correlated with each other, making the results redundant and difficult to interpret. Second, the odds of finding significant differences simply because of chance rises with repeated use of the sample data.

Multivariate analysis of variance (MANOVA) is an extension of the univariate ANOVA into multiple dimensions where these issues are addressed. MANOVA transforms data to a new coordinate system where the separation between the dependant variables is maximized. If there are only two groups, MANOVA is equivalent to the Hotelling's  $T^2$  test.

### 6.2.1 Hotelling's $T^2$

As an analogue to the t-test in one dimension, Hotelling's  $T^2$  can be used to investigate whether samples from two normal populations can be assumed to have the same mean.

Having two independent stochastic variables  $\mathbf{X}_1, \dots, \mathbf{X}_n$  and  $\mathbf{Y}_1, \dots, \mathbf{Y}_m$  where

$$\begin{aligned} \mathbf{X}_i &\in N_p(\mu, \Sigma) \\ \mathbf{X}_i &\in N_p(\nu, \Sigma), \end{aligned}$$

we wish to test the null hypothesis  $H_0 : \mu = \nu$  against  $H_1 : \mu \neq \nu$ . Using

$$\begin{aligned}
\bar{\mathbf{X}} &= \frac{1}{n} \sum_{i=1}^n \mathbf{X}_i \\
\bar{\mathbf{Y}} &= \frac{1}{m} \sum_{i=1}^m \mathbf{Y}_i \\
\mathbf{S}_1 &= \frac{1}{n-1} \sum_{i=1}^n (X_i - \bar{X})(X_i - \bar{X})' \\
\mathbf{S}_2 &= \frac{1}{m-1} \sum_{i=1}^m (Y_i - \bar{Y})(Y_i - \bar{Y})' \\
\mathbf{S} &= \frac{(n-1)\mathbf{S}_1 + (m-1)\mathbf{S}_2}{n+m-2}
\end{aligned}$$

and

$$T^2 = \frac{nm}{n+m} (\bar{\mathbf{X}} - \bar{\mathbf{Y}})' \mathbf{S}_1^{-1} (\bar{\mathbf{X}} - \bar{\mathbf{Y}})$$

the critical area for testing  $H_0$  against  $H_1$  at the significance level  $\alpha$  is equal to

$$C = \{\mathbf{x}_1, \dots, \mathbf{x}_n, \mathbf{y}_1, \dots, \mathbf{y}_m \mid \frac{n+m-p-1}{(n+m-2)p} t^2 > F(p, n+m-p-1)_{1-\alpha}\}$$

where  $t^2$  is the observed value of  $T^2$ .

### 6.2.2 One-way MANOVA

One-way MANOVA is simply an extension of Hotelling's  $T^2$  test to more than two groups. In one-way MANOVA we have a single independent variable with more than two levels (for example right-handed, left-handed and mixed-handed) and multiple dependent variables, and wish to test whether or not the means of the groups can be assumed to be equal.

Having  $k$  independent, normally distributed stochastic variables

$$\begin{array}{ccc} X_{11}, & \dots, & X_{1n_1} \\ \vdots & & \vdots \\ X_{k1}, & \dots, & X_{kn_k} \end{array}$$

where  $\mathbf{X}_{ij} \in N_p(\mu_i, \Sigma)$ ,  $i = 1, \dots, k$ ;  $j = 1, \dots, n_i$ , we wish to test the null hypothesis  $H_0 : \mu_1 = \dots = \mu_k$  against  $H_1 : \exists i, j (\mu_i \neq \mu_j)$ . With

$$\begin{aligned} \mathbf{T} &= \sum_{i=1}^k \sum_{j=1}^{n_i} (\mathbf{Y}_{ij} - \bar{\mathbf{Y}})(\mathbf{Y}_{ij} - \bar{\mathbf{Y}})' \\ \mathbf{W} &= \sum_{i=1}^k \sum_{j=1}^{n_i} (\mathbf{Y}_{ij} - \bar{\mathbf{Y}}_i)(\mathbf{Y}_{ij} - \bar{\mathbf{Y}}_i)' \\ \mathbf{B} &= \sum_{i=1}^k n_i (\bar{\mathbf{Y}}_i - \bar{\mathbf{Y}})(\bar{\mathbf{Y}}_i - \bar{\mathbf{Y}})' \end{aligned}$$

where (with  $n = \sum_i n_i$ )

$$\begin{aligned} \bar{\mathbf{Y}}_i &= \frac{1}{n_i} \sum_{j=1}^{n_i} \bar{\mathbf{Y}}_{ij} \\ \bar{\mathbf{Y}} &= \frac{1}{n} \sum_{i=1}^k \sum_{j=1}^{n_i} \bar{\mathbf{Y}}_{ij} \end{aligned}$$

the critical area for testing  $H_0$  against  $H_1$  at the significance level  $\alpha$  is equal to

$$\{y_{11}, \dots, y_{kn_k} \mid \frac{\det(\mathbf{W})}{\det(\mathbf{t})} \leq U(p, k-1, n-k)_\alpha\}$$

where  $\mathbf{t}$  is the observed value of  $\mathbf{T}$ . As mentioned, MANOVA also yields the transformation of the dependent variables that maximizes the separation between groups — these are called the canonical components.

## 6.3 Correlation analysis

In statistics correlation analysis is used to quantify the relationship between two variables. A number of different coefficients are used for this. Two of the most commonly used are Pearson's correlation and Spearman's  $\rho$ .

Pearson's correlation reflects the degree of linear relationship between two variables. It ranges from -1 to +1 where a correlation of -1 means a perfect negative linear relationship between the two variables and a correlation of +1 means a perfect positive linear relationship. Pearson's correlation is denoted by  $r$  when computed in a sample. For a sample of  $n$  observations of  $x$  and  $y$  the correlation coefficient is calculated as:

$$r = \frac{1}{n-1} \sum_{i=1}^n \left( \frac{x_i - \bar{x}}{s_x} \right) \left( \frac{y_i - \bar{y}}{s_y} \right),$$

where  $\bar{x}$  and  $\bar{y}$  are the sample means of  $x$  and  $y$ , and  $s_x$  and  $s_y$  are the sample standard deviations.

To measure the significance of the correlation we can test the null hypothesis of no correlation by converting the Pearson's  $r$  to a normal distributed variable  $Z$  by the transformation:

$$Z = \frac{\sqrt{n-3}}{2} \ln \frac{1+r}{1-r}.$$

Spearman's  $\rho$  differs from Pearson's correlation in that the computations are done after the numbers are converted to ranks. This means that it does not assume that the relationship between the variables is linear, nor does it make any assumptions about the frequency distribution of the variables. This makes Spearman's  $\rho$  less sensitive to single outliers.

## 6.4 Multiple regression

Multiple regression is an extension of ordinary linear regression where only one variable is used as an explanatory factor. If we instead have  $k$  explanatory factors ( $x$ ) and  $n$  observations of  $Y$  the model can be written as:

$$\begin{bmatrix} Y_1 \\ \vdots \\ Y_n \end{bmatrix} = \begin{bmatrix} 1 & x_{11} & \dots & x_{k1} \\ \vdots & \vdots & & \vdots \\ 1 & x_{1n} & \dots & x_{kn} \end{bmatrix} \cdot \begin{bmatrix} \alpha \\ \beta_1 \\ \vdots \\ \beta_k \end{bmatrix} + \begin{bmatrix} \epsilon_1 \\ \vdots \\ \epsilon_k \end{bmatrix}$$

or for short:

$$\mathbf{Y} = \mathbf{x}\boldsymbol{\beta} + \boldsymbol{\epsilon}$$

Under the assumption of  $\boldsymbol{\epsilon} \in N(\mathbf{0}, \sigma^2 \mathbf{I})$  the least square estimate is:

$$\boldsymbol{\beta} = (\mathbf{x}'\mathbf{x})^{-1}\mathbf{x}'\mathbf{Y}$$

When choosing a model it often becomes a problem to limit the number of explanatory factors while still being able to describe the observations. A commonly used method for this is stepwise regression. By using this method we are able to decide which factors are significant and should be included in the model. The method uses an iterative approach, adding and removing dependent variables from the regression model as they come in and out of significance. The method is explained in figure 6.2.

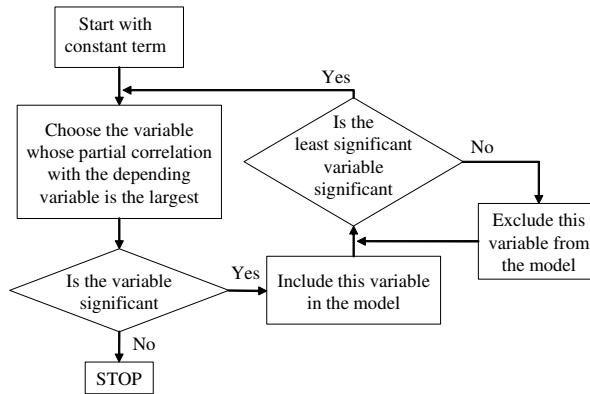


Figure 6.2: Flow chart for the stepwise regression method.

References: [23], [24].





# Results: Cross-sectional study

---

Having presented the methods we intend to use for the studies, this chapter puts the methods to use in the cross-sectional analysis of the LADIS data. For the cross-sectional analysis, a set of 50 images is available.

To reiterate, the steps we take in the cross-sectional analysis are:

1. Brain extraction on baseline images.
2. Spatial normalization of baseline images to a common reference.
3. Metric extraction from the results from 2.
4. Statistical analysis of results.

## 7.1 Brain extraction

Running the automatic brain extraction on the baseline images results in image volumes containing only gray matter, white matter, and internal cerebrospinal fluid (see figure 7.1). Visual inspection of the extracted images shows that for four of the volumes the automatic brain extraction has not succeeded. This

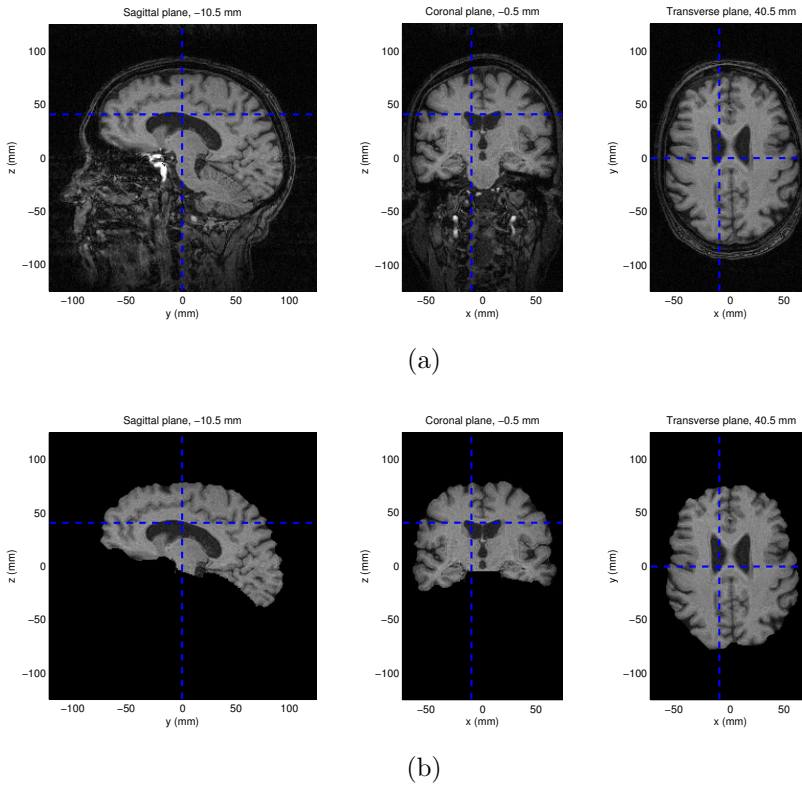


Figure 7.1: Slices from a single MR image before brain extraction (a) and after brain extraction (b).

has been corrected by means of manual intervention to yield a total of 50 brain extracted images.

## 7.2 Spatial normalization between subjects

Having extracted the brains from the images, we can proceed with the spatial normalization by registration. Several parameters have to be chosen for the registration:

- Registration target
- Image filtering parameters

- Similarity measure
- Global transformation parameters
- Multi-level grid size
- Regularization parameters

### 7.2.1 Registration target

There are two obvious options for the target image during the registration: An atlas or one of the source images.

An atlas is a mean image of several spatially normalized images. Advantages of using an atlas for registration are that it provides a reference that captures general variation of a population and that it often provides additional information such as region labels, tissue labels, etc.

On the other hand, using an atlas stemming from a population that is very different (in terms of brain morphology) from the source images, can introduce a need for an overly unconstrained transformation during the registration. Furthermore, because of natural variability between brains, an atlas tends to have less defined edges between structures (see figure 7.2) compared to a source image (see figure 7.1).

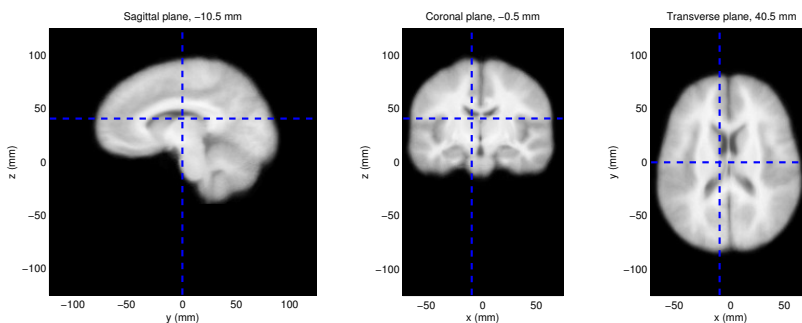


Figure 7.2: Image atlas: Three slices from the LONI LPBA40 atlas [25].

If a source image is used, it becomes important to choose a “normal” image — that is, an image whose features to some degree resemble those of the rest of the source images. If the target is chosen correctly, some of the population

tendencies (e.g. enlarged ventricles) will already be partially modelled, leading to the need for less unconstrained transformations.

Using a source image also has the advantage of providing an image with much more well defined edges between structures. This can lead to larger effect sizes in the later statistical analysis [26].

On the other hand, none of the additional information (such as labels) exists for our source images. This can however be remedied by registering an atlas with the label information to the chosen target and transforming the information into target space.

To assist in the choice, we have performed trial registrations to both an atlas and a subject image, and have concluded that the best choice is to use a subject image as the target. The reason for this is that the achieved spatial normalizations are more consistent (due to the better defined structures in a subject image).

For the above mentioned reasons, we choose to use one of the source images as the target in the registration. After some consideration, subject number 2 was chosen. This choice was based on image quality and a visual comparison with other subjects. Furthermore, a labelled atlas was amenable to registration to subject 2.

## 7.2.2 Image filtering

MR images are as mentioned in section 2.1.5 on page 5 affected by noise and other artifacts from the image acquisition. While some of the artifacts are very localized, others are more global.

To avoid that the registration models the noise in the images instead of the differences between the subjects and the target, a preprocessing of the images is necessary before the registration is initiated.

A simple but efficient way to remove the noise is to filter the images. How much filtering is needed is a balance between the noise removal and preserving the important features in the image. The images in figure 7.3 show different degrees of filtering using a gaussian kernel.

The images show that the noise is insufficiently removed when using a gaussian kernel with a FWHM of 0.5 mm. The noise in the image could potentially still disturb the registration yielding incorrect results. On the other hand, using a

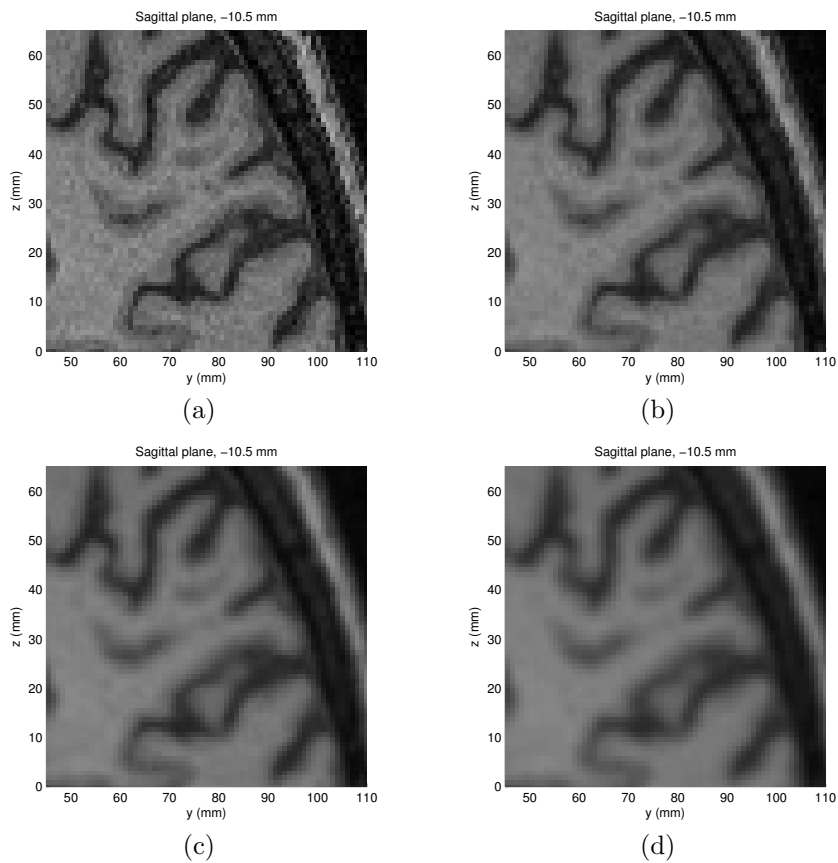


Figure 7.3: Crops from the same single sagittal slice. (a): The image without any filtering. The images shown in (b)-(d) are filtered using a gaussian kernel with a FWHM of: (b) 0.5 mm, (c) 0.75 mm, (d) 1.0 mm.

FWHM of 1.0 mm seems to eradicate the fine details in the image. We choose to filter with a gaussian kernel of FWHM 0.75 mm because it removes the noise while still preserving details in the image. Tests show that it is necessary to perform the filtering and that the chosen gaussian kernel width is appropriate.

### 7.2.3 Similarity measure

When measuring the image similarity a range of similarity measures are available (see section 4.2.3). The simplest and probably the most used of these is the sum of squared differences (SSD). To use this measure, it is required that the same tissue has the same image intensity across the images. One way to deal with this is to apply a bias field correction to the images but this method also has drawbacks [7].

However, bias field correction is only really necessary when the images are affected by spatially varying intensity. By visual inspection of the images this does not seem to be the case. The intensity difference between the images is on a more general level. An example of this is shown in figure 7.4. Although the difference is not very clear on the image, it is very evident when looking at the histograms of the images (figure 7.5).

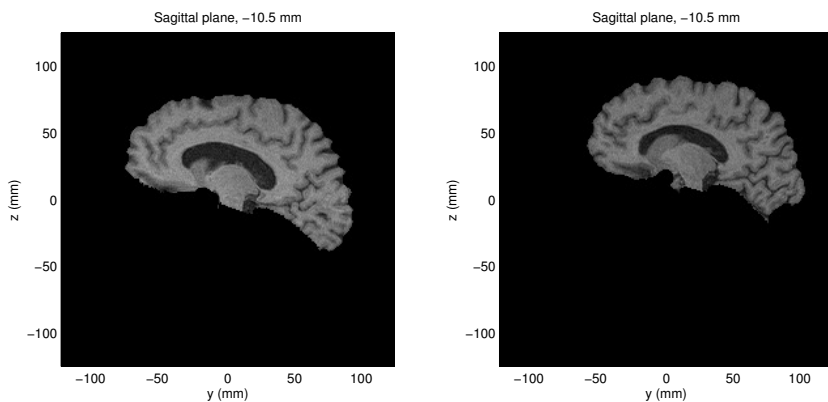


Figure 7.4: Sagittal slices from two subjects. The general intensity level is slightly lower in the right image than in the left.

Instead of using SSD we choose to use normalized mutual information (NMI) as the similarity measure. NMI has several advantages. One is that it is invariant to the mentioned intensity differences. Additionally it has proven itself very powerful in numerous applications and highly efficient in registration of neuroimages [26].

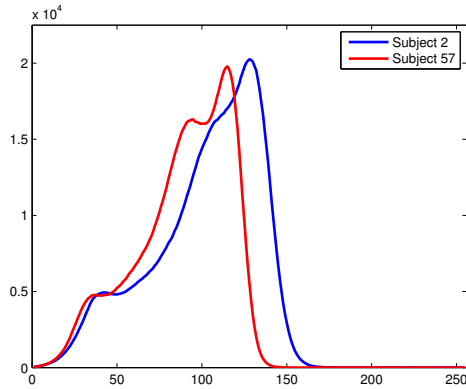


Figure 7.5: The histogram of the two brains depicted in figure 7.4. The blue curve corresponds to the left image.

### 7.2.4 Global registration

When doing the global registration the multi-resolution approach (described in section 4.2.2 on page 25) is especially useful. We find that three resolution levels is sufficient to ensure that the registration finds the correct minimum in the optimization.

To make sure that the following local registration has the best initial conditions possible, an affine registration with 12 degrees of freedom is chosen. Since scaling is a part of the affine registration there are three ways of doing the registration:

- Registration to the whole target head
- Registration to the target brain
- Registration to the target skull

The premise of the global registration is that “normal” brains have approximately the same relative size compared to the skull. The goal of the global registration is then to remove the influence of differences in skull size while retaining differences in brain size that are to be captured by the ensuing local registration.

If we registered to the target brain we would at the same time as removing the influence of the size of the brain also eliminate the possibilities for detecting

age-related atrophy in the later analysis. If the source was registered to the whole target head, the result would be a combination of trying to match the source brain to the target brain and the skull to the skull. This could change from subject to subject without indication, thus rendering the results less useful. Because of these reasons we choose to do the global registration to the target skull.

An example of an affine registration is shown in figure 7.6.

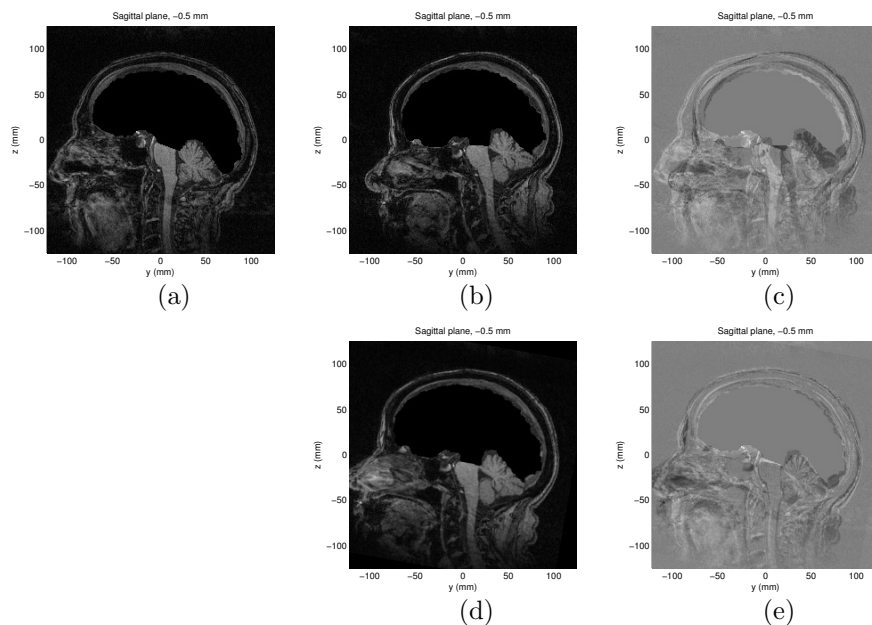


Figure 7.6: Affine registration: The source in (b) is registered to the target in (a). The result is shown in (d). The difference between the target and the source is shown in (c) before registration and in (e) after.

### 7.2.5 Multi-level grid

As mentioned in section 4.2.2 the spacing of the control points regulates the level at which the deformation takes place. A coarse deformation grid leads to registration of the large structures in the brain, e.g. ventricles and lobes, while finer grids result in spatial normalization of the smaller structures, e.g. the smaller gyri.



In the cross-sectional registration we need to take the large variability of the brains into account. Therefore it is necessary to initiate the registration with the use of a very coarse grid. To accommodate this we choose a starting grid spacing of 32 mm.

While it is possible to register the large structures in the brain, there is a limit on how fine a registration is possible (per section 2.3). Unlike the deep fissures which separate the lobes, the topology of the smaller sulci is very different between brains [27]. In fact, the same secondary and tertiary sulci are not even found in all subjects [28]. With that taken into consideration it does not make sense to use a smaller grid size than 4 mm. The control point mesh hierarchy we have chosen to use is visualized in figure 7.7.

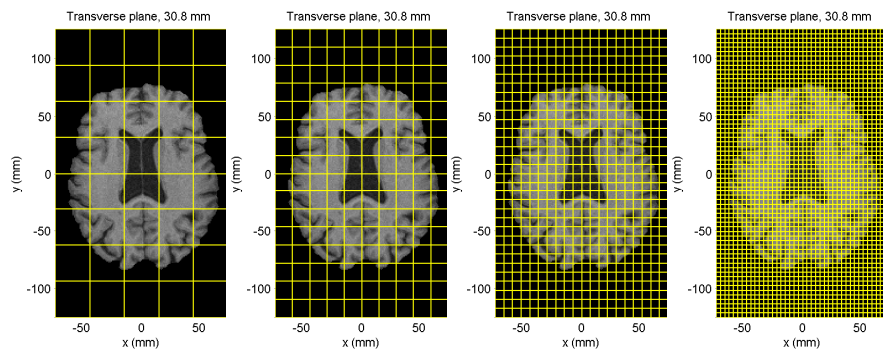


Figure 7.7: Transverse slices of the image volume shown with grids with decreasing spacing. From left to right: 32 mm, 16 mm, 8 mm, and 4 mm.

## 7.2.6 Regularization parameters

The choice of regularization parameters has a large influence on the achieved registration. As mentioned in chapter 4, we allow for three explicit types of regularization using three different penalties: A smoothness penalty, a volume penalty, and a topology penalty.

In the cross-sectional registration, objects with fundamentally different topologies are being registered. For this reason the topology preserving penalty is not used. Also, since we actually expect that different subjects have varying volumes of certain structures (and want to capture this in the registration), we choose not to use the volume preserving penalty.

Instead we choose to use only the smoothness preserving penalty. This is done to ensure that the registration does not descend into minima that result in unrealistic transformations.

The smoothness penalty is controlled by the parameter  $\lambda_1$ . Because of the nature of the multi-level grid approach,  $\lambda_1$  has to be chosen individually for each grid spacing  $\delta_\Phi$ . We choose the parameter by performing registrations with different values of  $\lambda_1$  and inspecting them visually (see figures 7.8 to 7.11).

The chosen parameter for each level is the one that allows the registration to achieve the highest correspondence between brain structures while still representing “realistic” transformations without large overlaps etc.

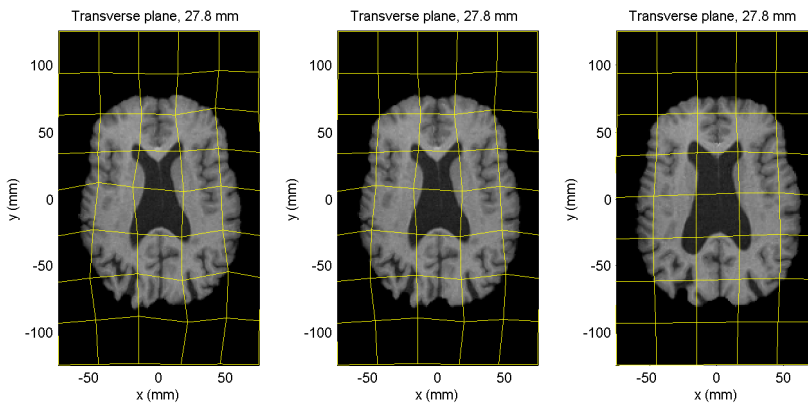


Figure 7.8: Choosing  $\lambda_1$  for  $\delta_\Phi = 32$  mm. From left to right:  $\lambda_1 = 0$ ,  $\lambda_1 = 0.0001$ ,  $\lambda_1 = 0.005$ .

The chosen parameter set is listed in table 7.1.

$\delta_\Phi$ (mm)	$\lambda_1$
32	0.0001
16	0.0001
8	0.0075
4	0.05

Table 7.1: Chosen values of  $\lambda_1$

These parameters are a good compromise between image similarity and transformation smoothness, from the coarsest level modelling the global differences

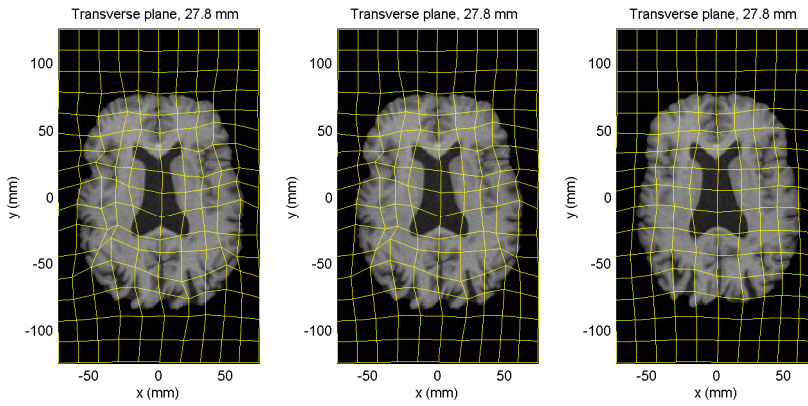


Figure 7.9: Choosing  $\lambda_1$  for  $\delta_\Phi = 16$  mm. From left to right:  $\lambda_1 = 0$ ,  $\lambda_1 = 0.001$ ,  $\lambda_1 = 0.005$ .

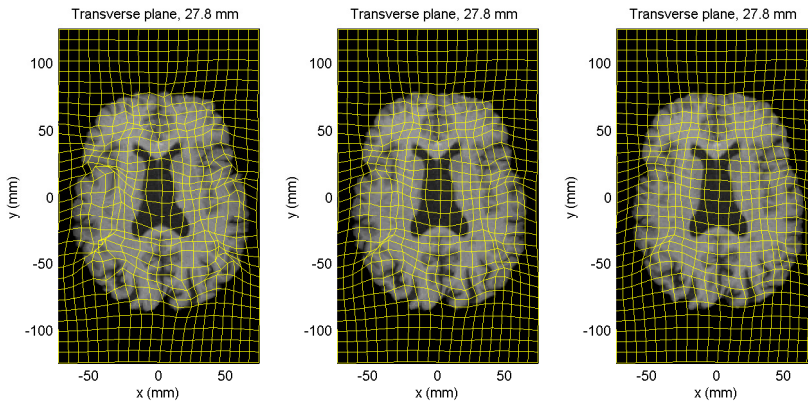


Figure 7.10: Choosing  $\lambda_1$  for  $\delta_\Phi = 8$  mm. From left to right:  $\lambda_1 = 0.002$ ,  $\lambda_1 = 0.0075$ ,  $\lambda_1 = 0.02$ .

to the finest level modelling detail differences (see figure 7.12). This effect can more clearly be seen in difference images (see figure 7.13).

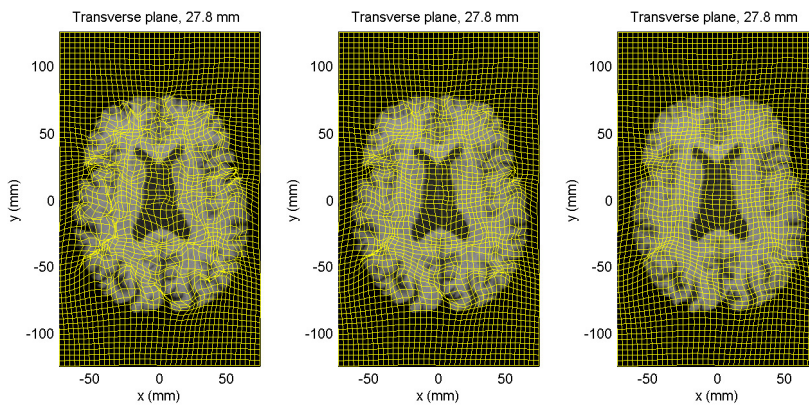


Figure 7.11: Choosing  $\lambda_1$  for  $\delta_\Phi = 4$  mm. From left to right:  $\lambda_1 = 0.01$ ,  $\lambda_1 = 0.05$ ,  $\lambda_1 = 0.2$ .

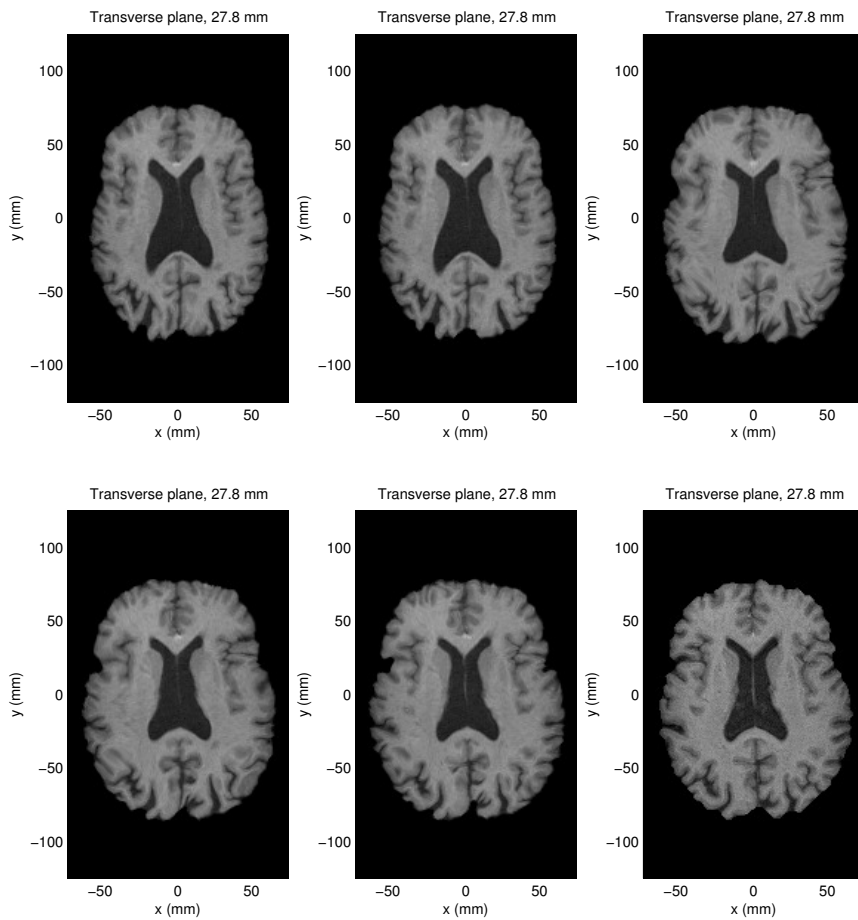


Figure 7.12: Step by step multi-level registration (subject 15 to subject 2). From top left to bottom right: Source image,  $\delta_{\Phi} = 32$  mm,  $\delta_{\Phi} = 16$  mm,  $\delta_{\Phi} = 8$  mm,  $\delta_{\Phi} = 4$  mm, target image. As the grid spacing decreases, the size of aligned structures decreases.

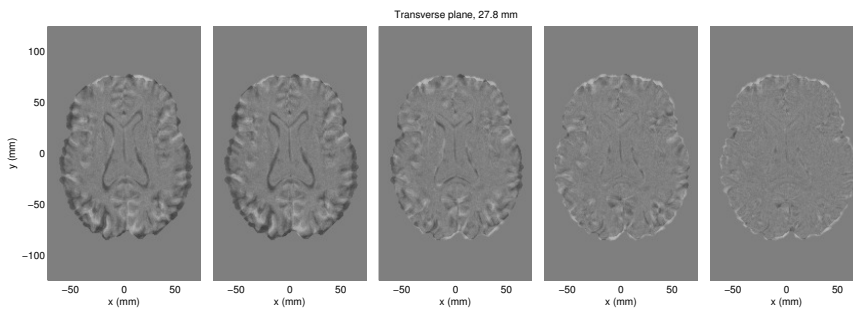


Figure 7.13: Step by step difference between registered image and target in multi-level registration (subject 15 to subject 2). From left to right: Source image,  $\delta_{\Phi} = 32$  mm,  $\delta_{\Phi} = 16$  mm,  $\delta_{\Phi} = 8$  mm,  $\delta_{\Phi} = 4$  mm. As the grid spacing decreases, the transformation models smaller structures, leading to smaller difference between the images.

### 7.2.7 Registration results

The result of the registrations are the transformations that transform source images into the target image (subject 2). We use several ways to ensure the validity of the registrations:

- Visual inspection of transformed images
- Visual inspection of deformation grids
- Atlas building

#### 7.2.7.1 Visual inspection of transformed images

The transformed images can be visually inspected to ensure that the registration has succeeded (see figure 7.14). Difference images provide an additional way to make sure that the images are correctly registered. Inspection of the images shows that all the registrations are satisfactory.

#### 7.2.7.2 Visual inspection of deformation grids

To ensure that the deformation grids represent plausible transformations, we inspect the grids. This inspection shows that the grids are all well behaved. A few examples can be seen in figure 7.15.

#### 7.2.7.3 Atlas building

Another way of validating the results of the registration is to build an atlas. As mentioned earlier, an atlas is a mean of several images — in this case registered images. As we progress down through the grid spacing sizes, the atlas should become increasingly well defined in decreasingly sized areas. This effect is seen in figure 7.16. More images from the atlases can be seen in appendix B on pages 105 to 107.

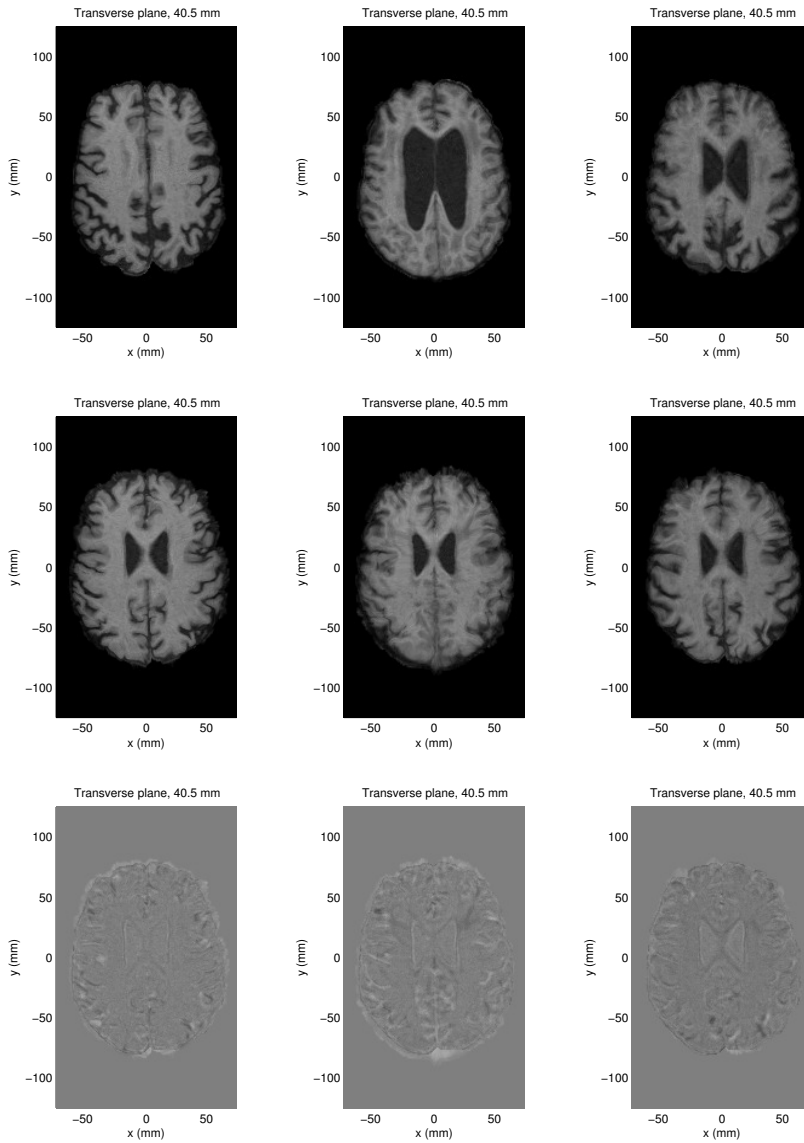


Figure 7.14: Registration of different subjects to target. From left to right: Subject 1, subject 16, subject 56. From top to bottom: Images after global registration, after local registration, difference compared to target.



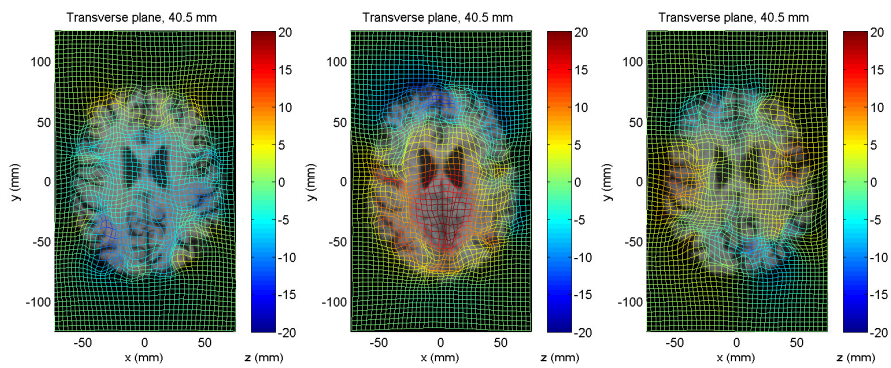


Figure 7.15: Deformation grids for registrations of different subjects to target. From left to right: Subject 1, subject 16, subject 56.

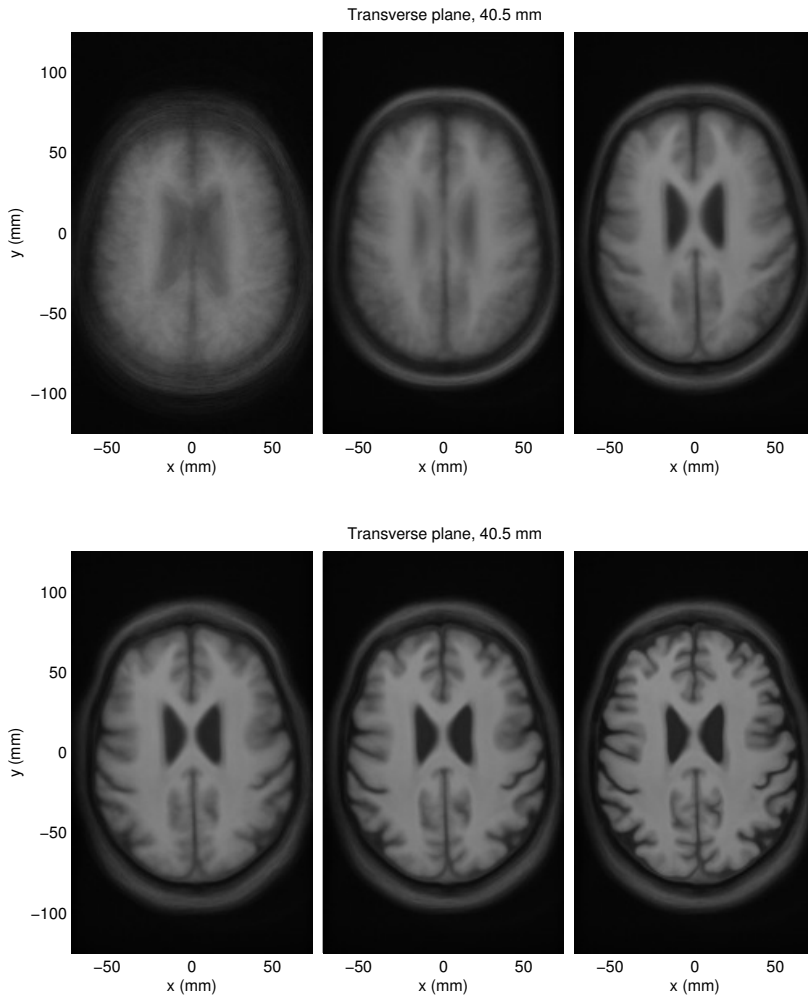


Figure 7.16: Transverse slice of atlas made from multi-level registration using increasingly fine grid spacings. From left to right the atlas is built from: Source images, globally registered images, locally registered images with  $\delta_{\Phi} = 32$  mm,  $\delta_{\Phi} = 16$  mm,  $\delta_{\Phi} = 8$  mm,  $\delta_{\Phi} = 4$  mm. As the grid spacing decreases, the transformation models smaller structures, leading to finer details being captured in the atlas.

## 7.3 Metric extraction

Using the control point fields from the registration, we can proceed to the metric extraction step. For the cross-sectional data we choose only to use the relative volume metric (and not the Log-Euclidean metrics). This choice is made because we expect between subject differences to be so large that relative volumes give enough information.

### 7.3.1 Relative volumes

As described in chapter 5 relative volumes can be used as a metric for differences. Following calculation of the Jacobian matrix in every voxel in each volume, we can generate complete volumes of containing relative volumes. A few examples are seen in figure 7.17.

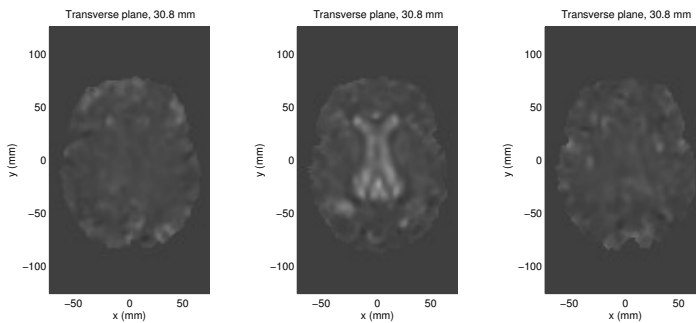


Figure 7.17: Slices from volumes of relative volumes. Bright represents areas which are larger in the source than in the target, and vice versa for dark areas. From left to right: Subject 1, subject 16, subject 56. It is clear that subject 16 has a much larger ventricular area than the target (subject 2).

After calculating the relative volumes as described, we start by inspecting their distribution and compare it to a simulated set to determine if the result is as expected. Under the assumption that the elements of the Jacobian matrix are normally distributed, the simulated values are generated as follows:

$$|\mathbf{V}_{relative,sim}| = \det \left( \begin{bmatrix} N(0, \sigma) & N(0, \sigma) & N(0, \sigma) \\ N(0, \sigma) & N(0, \sigma) & N(0, \sigma) \\ N(0, \sigma) & N(0, \sigma) & N(0, \sigma) \end{bmatrix} + \begin{bmatrix} 1 & 0 & 0 \\ 0 & 1 & 0 \\ 0 & 0 & 1 \end{bmatrix} \right),$$

where  $\sigma$  has been chosen to be 0.26. The difference between the simulated data and the actual observations may be explained by the fact that the brain of subject 2 is not a true “mean brain”. That taken into account the observed data is as expected. The distributions are shown in 7.18.

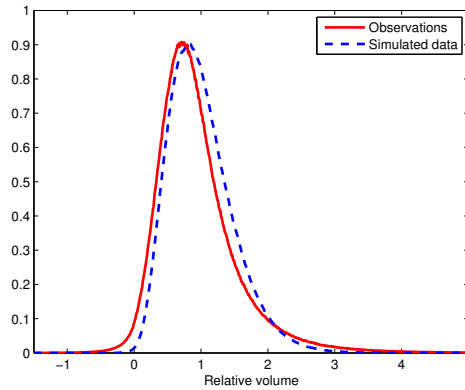


Figure 7.18: Histograms of relative volumes from all subjects except no. 2 along with simulated values.

A number of analyses have shown that atrophy takes place in the white and gray matter of the brain [29]. Since the degenerated matter has to be replaced by something the result is that the amount of CSF increases. Because of this CSF can be used as a measure of global brain atrophy. Figure shows the distribution of the relative volumes separated into gray and white matter, and CSF.

A look at the distributions show that they cannot be assumed to be normal. Normality is an important prerequisite for some of the statistical measures that will be used later. As indicated in [20], the distributions of the relative volumes can be expected to be more log-normally distributed. Transforming the data with a logarithmic transformation should then yield data that is more normally distributed. Histograms of the transformed data can be seen in figure 7.20.

Following the transformation, the data is much more normally distributed.

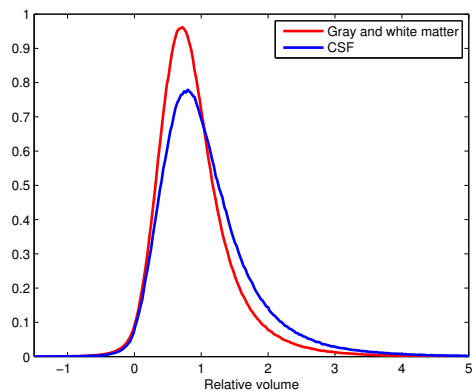


Figure 7.19: Relative volumes from all subjects except no. 2, separated into gray and white matter, and CSF.

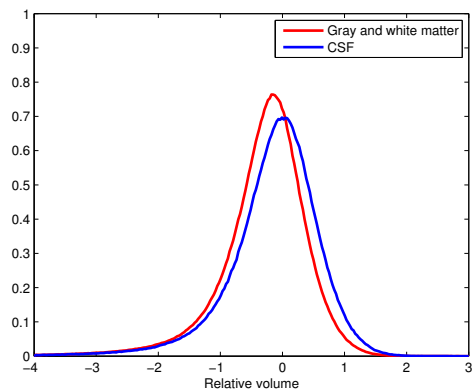


Figure 7.20: Logarithmically transformed relative volumes from all subjects except no. 2, separated into gray and white matter and CSF.

## 7.4 Statistical analysis

In this section we give some examples of how the data from the information extraction can be analyzed. In the cross-sectional analysis, the goal is to find differences between subjects. For this, several approaches to the analysis are possible:

- Per voxel test
- Regional test
- Global test
- Group test

In addition to these tests, we can test for correlation with some of the clinical measurements that are available from the LADIS study (age, BMI, etc.).

### 7.4.1 Per voxel test

In the per voxel test, each relative volume voxel is treated as a separate observation  $V_{rel}$ , and tested cross-sectionally across the 50 subjects for significance. Under the assumption that in each voxel, across the subjects, the data is normally distributed, each voxel can be assigned a Z score and a p-value can be found. Since we are interested in studying both significant expansions and contractions, a two-sided test is employed.

For each subject this gives a volume containing the probability that for a given relative volume voxel tells us how likely an outcome as or more extreme is to have happened compared to the rest of the subjects (see figure 7.21).

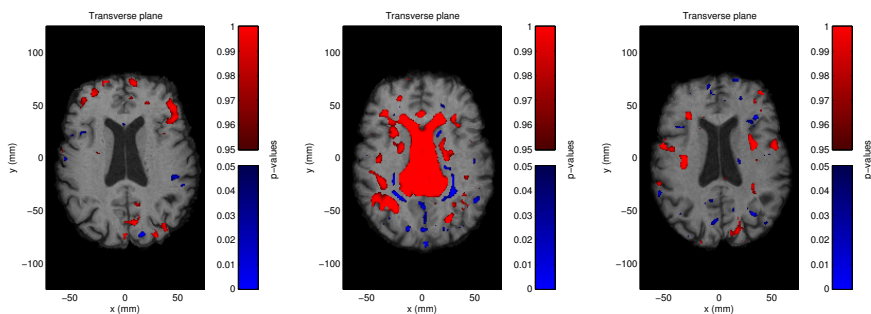


Figure 7.21: Significant differences in  $V_{rel}$  overlaid on normalized images. The overlay shows  $p < 0.05$  and  $p > 0.95$  in blue and red respectively. From left to right: Subject 1, subject 16, subject 56. It is clear that subject 1 has a large significant expansion in the ventricles (the large red area in the center).

As we discovered in section 7.3.1, assuming that the determinants are normally distributed may not be prudent. Transforming the relative volumes with a log-

arithmetic transformation results in more normally distributed data. Conducting the per voxel test on the transformed data yields results that are less likely to unfairly discount contraction effects. This effect can be seen in figure 7.22, where expanding areas become less significant and contracting areas become more significant.

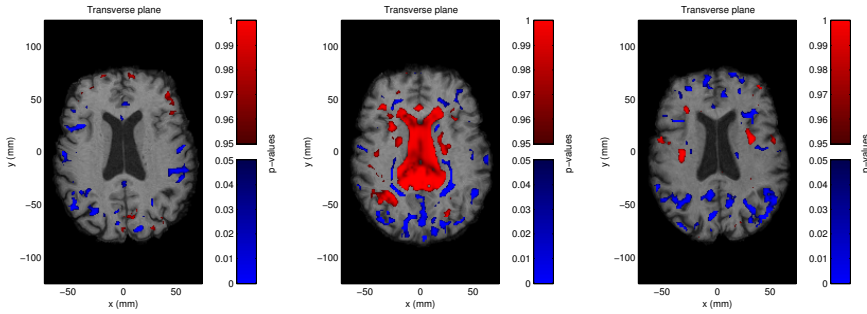


Figure 7.22: Significant differences in  $\log(V_{rel})$  overlaid on normalized images. The overlay shows  $p < 0.05$  and  $p > 0.95$  in blue and red respectively. From left to right: Subject 1, subject 16, subject 56. Compared to figure 7.21, the areas with contractions are more significant, while the areas with expansions are less significant.

Using direct voxelwise statistics on the relative volumes might not be a good idea because of the uncertainties that exist in the spatial normalization. These uncertainties can lead to small misalignments that result in falsely significant or insignificant values. Additionally, the estimate of the mean and variance used in the per voxel test are uncertain because of small sample sizes. Furthermore, it might not always be interesting to know whether a single voxel is significant.

### 7.4.2 Regional test

To alleviate the problems with the voxelwise test, we can divide each brain into a number of volumes of interest (VOIs) and for each of these compare a compound measure cross-sectionally.

There is, however, one problem with this: We need to be able to divide each volume into equivalent VOIs. One way of solving this problem is to let an expert manually segment out areas of interest in each image. Another manner is to register an atlas to each image and utilize the label information that is available for the atlas. With a modification, the latter approach is the one we take.

Instead of registering the atlas to each image, we choose to register the atlas to the target image for the spatial normalization (i.e. subject 2). Since all the other subjects are normalized to subject 2, we can use the label information directly following the registration.

The atlas we use is the LONI Probabilistic Brain Atlas (LPBA40) [25] which was generated by spatially aligning MRI scans of 40 healthy individuals, resulting in a T1-weighted intensity atlas. Furthermore, each of the images were assigned labels for several structures (approximately 50), allowing both maximum probability and label volumes to be constructed (see appendix C for a complete list of labels). Unfortunately, the LPBA40 atlas does not provide labels for the entire brain — large parts of both the white matter and cerebrospinal fluid are not labelled at all. This limits the regional analysis to the labelled areas.

After registration of the intensity atlas to subject number 2, we use the label volume to partition our images into VOIs. A slice from both the intensity volume and the label volume is shown in figure 7.23.

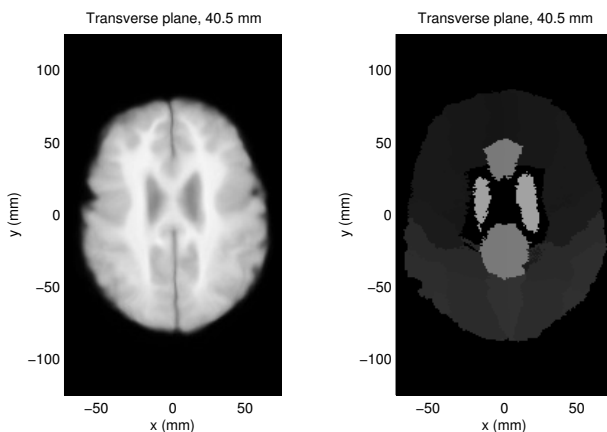


Figure 7.23: LPBA40 atlas after registration to subject 2. Intensity volume to the left, label volume to the right.

Having partitioned every image into VOIs, we can proceed with the construction of a compound measure that characterizes the relative volume change in each VOI. We choose to calculate the mean of all relative volumes within each VOI. This measure is effectively the relative volume of the VOI.

As in the per voxel test, we transform the data with a logarithmic transformation



to approach normality. The result is volumes with p-values assigned to each label (see figure 7.24).

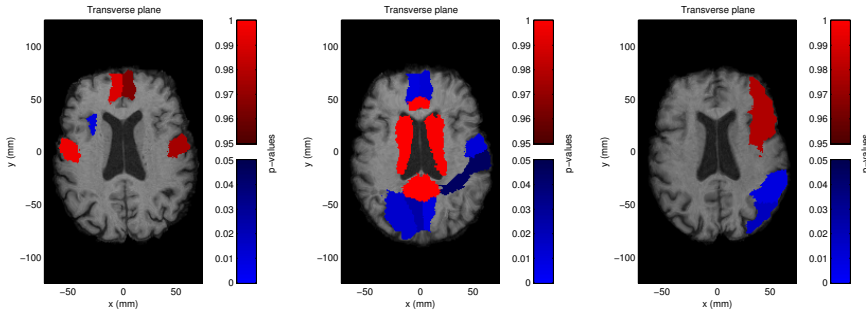


Figure 7.24: Significant differences in mean of regional  $\log(V_{rel})$  overlaid on normalized images. The overlay shows  $p < 0.05$  and  $p > 0.95$  in blue and red respectively. From left to right: Subject 1, subject 16, subject 56.

The tendencies from the voxelwise test are also evident in the regional test.

This is just one example of a regional approach to the tests. It might be beneficial to use larger regions instead of the in some cases very small LPBA40 regions — an example could be to divide the brain into lobes and perform the tests on them instead.

### 7.4.3 Group test

The results of the two previous tests were maps that showed in what areas a single subject was different from the rest of the subject. Another interesting thing to study is whether TBM can reveal differences between groups. We might, for example, expect there to be a general difference between males and females.

Several grouping parameters are available from the LADIS data set. We select three of these for analysis: Sex, handedness and Fazekas score. The Fazekas score evaluates white matter lesions on a discrete scale  $[0, 1, 2, 3]$  — for the subjects available to us, all the scores are between 1 and 3.

For each of these grouping parameters we wish to find out whether the regional relative volumes can be used to differentiate one group from another. As described in section 6.2 on page 37, this can be done using a one-way multivariate

analysis of variance (MANOVA), where the null hypothesis is that the means of the groups are equal to that of the others.

First, however, we reduce the data using principal component analysis (as described in section 6.1 on page 35). Following PCA, linear combinations of the data that represent 80% of the total variance in the data are chosen, resulting in the first 13 principal components being used. After projecting the data onto the selected principal components, we can conduct MANOVA for each of the grouping parameters. Table 7.2 shows the p-values for the hypothesis that the means lie in a space of dimension  $d = 0, 1$ , etc. From the table it can be inferred

Sex		Handedness		Fazekas	
$d$	p-value	$d$	p-value	$d$	p-value
0	0.0162	0	0.137	0	0.004
-	-	1	0.356	1	0.487

Table 7.2: MANOVA results

that the means of males and females are most likely different ( $p = 0.0162$ ). For handedness the results indicate that there is no significant difference between right, left and both-handers. This is perhaps to be expected since there are only four left-handers and five both-handers in the group of 50. The p-values for the Fazekas score indicate that the three groups are not discernable using the means of the regional relative volumes. They are, however, unlikely to belong to only one group ( $p = 0.004$ ).

A projection of the data onto the first two canonical components (the linear combinations that yield the largest separation between groups) can be seen in figure 7.25.

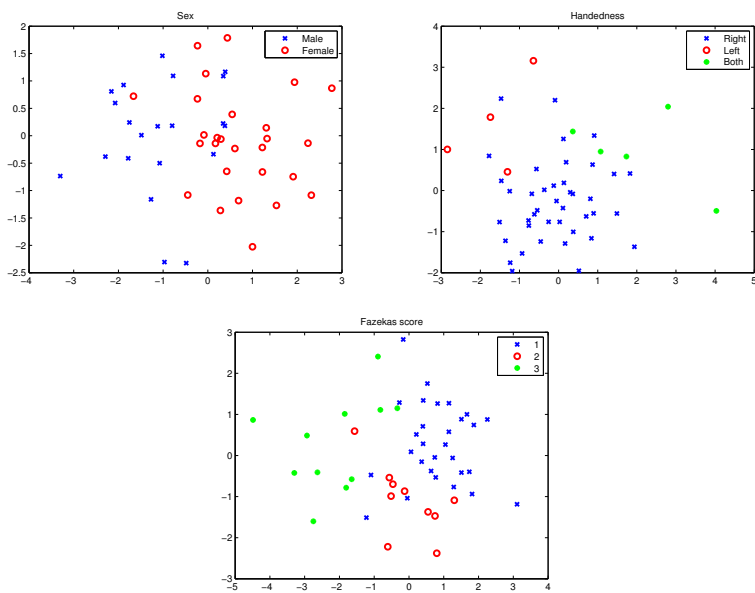


Figure 7.25: Data projected onto the first two canonical components from MANOVA. Separation between groups can be seen in the male/female plot, while it is less evident in the handedness and Fazekas score plots.

#### 7.4.4 Clinical correlation

Following the extraction of the relative volumes from the transformation it is possible to compare these to the clinical parameters. Doing this enables us to investigate the correlation between the atrophy and possible explanatory factors.

An intuitive way is to correlate the global differences with the most obviously related parameters. As described in chapter 2 the LADIS study provides a large number of clinical parameters. To limit the extent of the analysis and results, we have chosen to use the following parameters:

- Age
- Systolic blood pressure (BP<sub>sys</sub>)
- Diastolic blood pressure (BP<sub>dia</sub>)
- Body mass index (BMI)
- Stroop test, form 2 (Stroop2s, s)
- Trail making, part A (Trail1s, s)
- Verbal fluency, VADAS-cog (Verbal)
- Gait Velocity (Walking speed m/s)

Atrophy can as mentioned be measured as loss of gray and white matter volume but also as an increase of CSF volume. Combining these two measures provides a single valued measure for atrophy. This combined measure may even reveal information about atrophy only evident in either CSF or gray and white matter. The combined measure  $\mathcal{A}$  is calculated as the weighted mean:

$$\mathcal{A} = w \cdot \mu_{gw} + (1 - w) \cdot (2 - \mu_{csf}),$$

where  $w$  is ratio of gray and white matter compared to CSF, and  $\mu_{gw}$  and  $\mu_{csf}$  are the relative volume of respectively gray and white matter, and CSF.

In figure 7.26 the three atrophy measures are shown versus the age of the patients. Additionally the result of a linear regression is shown. The top left figure shows a small negative correlation between the relative volume of gray and white matter, and age. A larger positive correlation between the relative volume of CSF and age can be seen in the top right figure. Of the three measures the largest magnitude of correlation is between the combined atrophy measure and age. This negative correlation is shown in the bottom figure.

These correlations are all as expected since they follow the theory that brain atrophy is related to age.

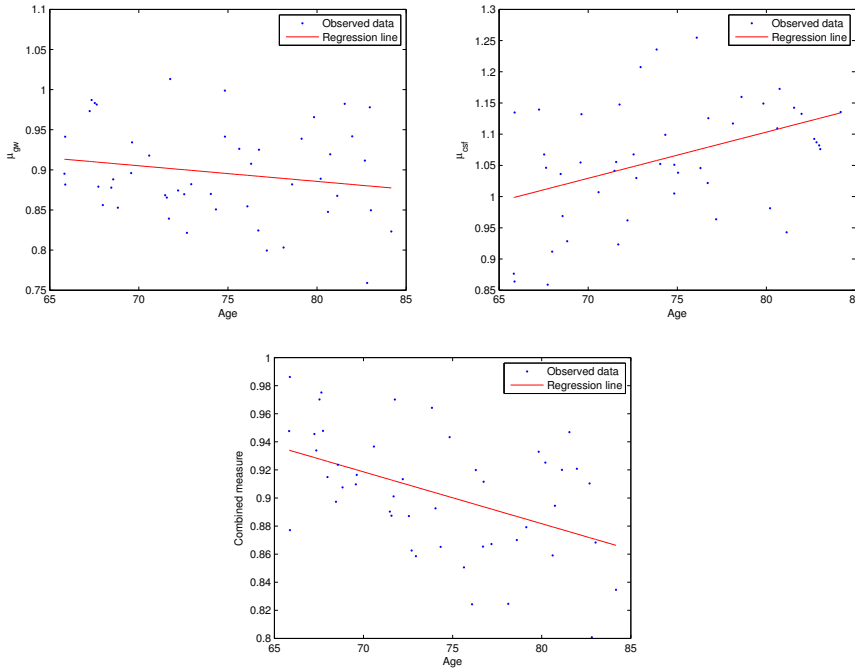


Figure 7.26: Scatter plot of age versus relative volumes of gray and white matter and CSF. The right figure shows the combined atrophy measure. Linear regressions are shown with red lines.

To measure the degree of correlation two different measures are calculated: Pearson's  $r$  and Spearman's  $\rho$  as described in section 6.3.

Table 7.3 lists the correlations between the three atrophy measures and the eight above mentioned parameters. Many of the parameters show significant correlations while some of them (systolic and diastolic blood pressures) do not.

While some changes in the brain take place on a global level it is possible that some changes only happen locally. Having the information from the registered anatomical atlas available allows us to test this hypothesis by dividing the brain into the lobes. The lobe volume is constructed by combining the appropriate VOIs into the frontal, parietal, occipital, and temporal lobes (see appendix C). These subvolumes only contain gray and white matter and not CSF.

Clinical parameter	$\mu_{gw}$		$\mu_{csf}$		$\mathcal{A}_{combined}$	
	Pearson	Spearman	Pearson	Spearman	Pearson	Spearman
Age	$r=-0.187$ $p=2.02e-1$	$\rho=-0.194$ $p=1.85e-1$	$r=0.414$ $p=3.40e-3$	$\rho=0.407$ $p=4.39e-3$	$r=-0.475$ $p=7.41e-4$	$\rho=-0.453$ $p=1.54e-3$
BP <sub>sys</sub>	$r=0.055$ $p=7.13e-1$	$\rho=0.097$ $p=5.15e-1$	$r=0.214$ $p=1.48e-1$	$\rho=0.260$ $p=7.74e-2$	$r=0.013$ $p=9.30e-1$	$\rho=-0.040$ $p=7.87e-1$
BP <sub>dia</sub>	$r=-0.055$ $p=7.13e-1$	$\rho=-0.061$ $p=6.82e-1$	$r=-0.210$ $p=1.47e-1$	$\rho=-0.407$ $p=2.00e-1$	$r=-0.475$ $p=3.59e-1$	$\rho=-0.453$ $p=5.16e-1$
BMI	$r=-0.475$ $p=7.31e-4$	$\rho=-0.458$ $p=1.21e-3$	$r=-0.135$ $p=3.66e-1$	$\rho=-0.185$ $p=2.12e-1$	$r=-0.479$ $p=6.55e-4$	$\rho=-0.451$ $p=1.45e-3$
Stroop2s	$r=-0.233$ $p=1.15e-1$	$\rho=-0.153$ $p=3.03e-1$	$r=0.097$ $p=5.12e-1$	$\rho=0.117$ $p=4.27e-1$	$r=-0.400$ $p=5.92e-3$	$\rho=-0.343$ $p=1.97e-2$
Trail1s	$r=-0.127$ $p=3.96e-1$	$\rho=-0.255$ $p=8.33e-2$	$r=0.471$ $p=6.38e-4$	$\rho=0.450$ $p=1.19e-3$	$r=-0.400$ $p=4.40e-3$	$\rho=-0.575$ $p=1.57e-4$
Verbal	$r=0.036$ $p=8.11e-1$	$\rho=-0.021$ $p=8.91e-1$	$r=-0.390$ $p=6.74e-3$	$\rho=-0.422$ $p=3.09e-3$	$r=0.398$ $p=6.18e-3$	$\rho=0.325$ $p=2.74e-2$
Walking speed	$r=0.199$ $p=1.85e-1$	$\rho=0.123$ $p=4.17e-1$	$r=-0.297$ $p=4.24e-2$	$\rho=-0.356$ $p=1.41e-2$	$r=0.420$ $p=3.63e-3$	$\rho=0.349$ $p=1.73e-2$

Table 7.3: Correlation coefficients between clinical parameters and relative volume of gray and white matter ( $\mu_{gw}$ ), CSF ( $\mu_{csf}$ ), and the combined atrophy measure ( $\mathcal{A}_{combined}$ ). The shaded areas shows where the p-values for testing the hypothesis of no correlation against the alternative that there is a non-zero correlation is below 0.05.

Additionally we can investigate if there are any differences in correlation with regard to sex. An example of the correlation is shown in figure 7.27, where age is plotted against the relative volume of the left and right occipital lobes. The figure indicates that the regression coefficient is apparently different for men and women.

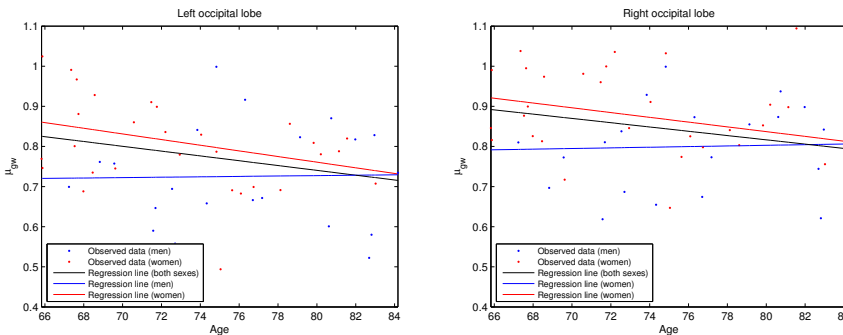


Figure 7.27: Scatter plot of age versus relative volumes of the occipital lobes. Additionally the linear regressions are shown for both sexes together and separately.

Scatter plots for the three other lobes are shown in appendix D. Table 7.4 summarizes the correlation coefficients for the relationship between age and the relative volumes of the lobes. Notice that the correlation is primarily present for women and not in all of the lobes. This suggests that the hypothesis that some changes in the brain are located locally, is correct.

Lobe	$\mu_{gw}$ (both sexes)		$\mu_{gw}$ (men)		$\mu_{gw}$ (women)	
	Pearson	Spearman	Pearson	Spearman	Pearson	Spearman
Left frontal	$r=-0.334$ $p=1.91e-2$	$\rho=-0.338$ $p=1.81e-2$	$r=-0.211$ $p=3.71e-1$	$\rho=-0.271$ $p=2.47e-1$	$r=-0.314$ $p=9.67e-2$	$\rho=-0.336$ $p=7.48e-2$
Right frontal	$r=-0.280$ $p=5.10e-2$	$\rho=-0.314$ $p=2.85e-2$	$r=-0.081$ $p=7.35e-1$	$\rho=-0.192$ $p=4.14e-1$	$r=-0.313$ $p=9.87e-2$	$\rho=-0.379$ $p=4.32e-2$
Left parietal	$r=-0.248$ $p=8.87e-2$	$\rho=-0.264$ $p=7.01e-2$	$r=-0.108$ $p=6.60e-1$	$\rho=-0.005$ $p=9.86e-1$	$r=-0.283$ $p=1.37e-1$	$\rho=-0.312$ $p=9.93e-2$
Right parietal	$r=-0.418$ $p=3.83e-3$	$\rho=-0.403$ $p=5.88e-3$	$r=-0.190$ $p=4.37e-1$	$\rho=-0.193$ $p=4.27e-1$	$r=-0.522$ $p=5.22e-3$	$\rho=-0.476$ $p=1.30e-2$
Left occipital	$r=-0.284$ $p=4.82e-2$	$\rho=-0.236$ $p=1.03e-1$	$r=0.020$ $p=9.30e-1$	$\rho=0.042$ $p=8.59e-1$	$r=-0.398$ $p=3.59e-2$	$\rho=-0.324$ $p=9.29e-2$
Right occipital	$r=-0.267$ $p=6.65e-2$	$\rho=-0.257$ $p=7.77e-2$	$r=0.040$ $p=8.68e-1$	$\rho=0.071$ $p=7.67e-1$	$r=-0.301$ $p=1.19e-1$	$\rho=-0.322$ $p=9.52e-2$
Left temporal	$r=-0.400$ $p=4.83e-3$	$\rho=-0.407$ $p=4.39e-3$	$r=-0.493$ $p=3.19e-2$	$\rho=-0.444$ $p=5.85e-2$	$r=-0.340$ $p=7.12e-2$	$\rho=-0.347$ $p=6.59e-2$
Right temporal	$r=-0.469$ $p=7.68e-4$	$\rho=-0.482$ $p=6.09e-4$	$r=-0.342$ $p=1.52e-1$	$\rho=-0.372$ $p=1.18e-1$	$r=-0.510$ $p=4.73e-3$	$\rho=-0.533$ $p=3.33e-3$

Table 7.4: Correlation coefficients between age and the relative volume of gray and white matter ( $\mu_{gw}$ )

The correlation coefficients for the other seven clinical parameters are listed in appendix D, where the same tendency to exhibit local changes is apparent. For instance correlations with verbal fluency and walking speed seem to be restricted to the temporal lobe. Others, such as BMI, are defined more globally. All of the strong correlations are as expected with regard to their sign.

Having concluded that the differences in the brain are locally defined, we can investigate if it is possible to narrow down the location of the differences even further. This is done by using the VOIs in the LPBA40 atlas separately (appendix C).

Table 7.5 summarizes the most significant correlations with  $p < 0.001$ . The table only lists the correlation coefficient for men and women together. As it can be seen many strong correlations can be derived from the registrations.

Having observed that a significant correlation between the relative volumes and the clinical parameters exists we can extend the modelling to multiple regression.

For this we will use the stepwise regression as described in section 6.4. In the model only linear terms are included since the quadratic terms in general did

Parameter	Label ID	$\mu_{gw}$ (both sexes)		Label ID	$\mu_{gw}$ (both sexes)	
		Pearson	Spearman		Pearson	Spearman
Age	23	$r=-0.594$ $p=2.67e-5$	$\rho=-0.587$ $p=4.97e-5$	65	$r=-0.620$ $p=2.61e-6$	$\rho=-0.606$ $p=8.05e-6$
	81	$r=-0.576$ $p=6.61e-5$	$\rho=-0.561$ $p=1.43e-4$	83	$r=-0.637$ $p=2.52e-6$	$\rho=-0.621$ $p=8.72e-6$
	84	$r=-0.468$ $p=7.97e-4$	$\rho=-0.473$ $p=7.92e-4$	164	$r=-0.496$ $p=5.25e-4$	$\rho=-0.483$ $p=8.94e-4$
BP <sub>sys</sub>	84	$r=-0.537$ $p=1.69e-4$	$\rho=-0.511$ $p=3.88e-4$			
BMI	27	$r=-0.473$ $p=8.90e-4$	$\rho=-0.469$ $p=1.02e-3$	28	$r=-0.469$ $p=8.78e-4$	$\rho=-0.510$ $p=2.52e-4$
	30	$r=-0.722$ $p=2.22e-8$	$\rho=-0.664$ $p=6.66e-7$	85	$r=-0.491$ $p=4.64e-4$	$\rho=-0.458$ $p=1.22e-3$
	86	$r=-0.569$ $p=5.68e-5$	$\rho=-0.528$ $p=2.32e-4$	91	$r=-0.519$ $p=3.08e-4$	$\rho=-0.501$ $p=5.40e-4$
	164	$r=-0.535$ $p=1.82e-4$	$\rho=-0.551$ $p=1.05e-4$			
Stroop2s	27	$r=-0.555$ $p=9.18e-5$	$\rho=-0.402$ $p=6.80e-3$			
Trail1s	65	$r=-0.622$ $p=3.01e-6$	$\rho=-0.507$ $p=2.72e-4$	86	$r=-0.620$ $r=-0.509$	$\rho=-0.606$ $\rho=-0.498$
	88	$r=-0.692$ $p=2.82e-7$	$\rho=-0.514$ $p=4.16e-4$	92	$r=-0.516$ $p=2.07e-4$	$\rho=-0.514$ $p=2.22e-4$
	101	$r=-0.491$ $p=3.96e-4$	$\rho=-0.454$ $p=1.19e-3$			
Verbal	29	$r=0.478$ $p=9.05e-4$	$\rho=0.485$ $p=7.37e-4$	86	$r=0.538$ $p=1.40e-4$	$\rho=0.514$ $p=3.06e-4$
Walking speed	49	$r=0.479$ $p=9.91e-4$	$\rho=0.476$ $p=1.09e-3$	65	$r=0.541$ $p=5.98e-5$	$\rho=0.533$ $p=8.03e-5$
	81	$r=0.609$ $p=6.32e-5$	$\rho=0.573$ $p=2.12e-4$	86	$r=0.577$ $p=3.30e-5$	$\rho=0.493$ $p=5.75e-4$
	91	$r=0.572$ $p=3.22e-5$	$\rho=0.560$ $p=5.14e-5$	92	$r=0.576$ $p=3.47e-5$	$\rho=0.540$ $p=1.27e-4$

Table 7.5: Correlation coefficients clinical parameters and the relative volumes ( $\mu_{gw}$ ) of VOIs from the LPBA40 atlas.

not yield significantly better results. This will also simplify the interpretation of the resulting model.

First we establish a model for explaining the global atrophy as defined by the combined measure. Which of the eight clinical parameters should be included is decided by performing a stepwise regression. The result is, that age, BMI, and the Trail making test yields an  $R^2$  of 0.41. The found model is:

$$\mathcal{A}_{combined} = -3.18e-3 \cdot \text{Age} - 4.72e-3 \cdot \text{BMI} - 6.50e-4 \cdot \text{Trail1s}$$

The p-values for each of the parameters and for the model are listed in tabel 7.6. This method is also applied to find a model for describing the relative volume in each of the eight lobes. The result of this is listed in table 7.7.



Parameter	$\mathcal{A}_{combined}$
Age	2.5401e-3
BMI	1.1958e-3
Trail1s	1.2947e-2
$R^2$	0.41
adj. $R^2$	0.36
$p$ -value	4.05e-5

Table 7.6:  $p$ -values for the atrophy model.

Parameter	Lobe			
	Left frontal	Right frontal	Left parietal	Right parietal
Age	3.6023e-3	5.9872e-3		4.2067e-2
BPsys	6.4132e-2	5.7342e-2		
BPdia				
BMI	4.4045e-4	4.8939e-3	1.6473e-2	7.9244e-2
Stroop2s				
Trail1s	7.7186e-3			
Verbal				
Walking speed				
$R^2$	0.45	0.27	0.12	0.13
adj. $R^2$	0.38	0.20	0.08	0.08
$p$ -value	4.21e-5	3.61e-3	1.65e-2	4.25e-2
Parameter	Left occipital	Right occipital	Left temporal	Right temporal
Age	3.3377e-2		7.9322e-2	5.7370e-3
BPsys			7.0199e-5	
BPdia		7.5350e-2		
BMI	2.3624e-2	6.0559e-2		3.0563e-3
Stroop2s		1.3102e-2		
Trail1s	3.1888e-2			6.6140e-4
Verbal			6.3785e-3	
Walking speed				
$R^2$	0.27	0.25	0.42	0.44
adj. $R^2$	0.20	0.18	0.37	0.39
$p$ -value	3.15e-3	6.20e-3	2.52e-5	1.27e-5

Table 7.7:  $p$ -values for the significant ( $p < 0.1$ ) parameters and for the models describing the relative volumes ( $\mu_{gw}$ ) of the lobes.

From this it can be concluded that it is possible to make a decent model for some of the lobes while it is harder for others. It can also be derived that some of the parameters, such as age and BMI, are more describing than other, e.g. walking speed.

While a model can be made for describing the relative volumes by the clinical parameters, the opposite approach is also possible (i.e. modelling clinical parameters by relative volumes).

If we want to model age we can try to describe this by the relative volume of the lobes. This turns out, however, not to be a good model ( $R^2 = 0.10$ ). Instead we use the 52 VOIs in the LPBA40 atlas as possible describing parameters. The result of this is a model with 5 explanatory factors (as listed in tabel 7.4) and  $R^2 = 0.55$ .

Label ID	Age
44	9.6290e-002
65	4.5140e-007
67	3.6921e-004
85	4.4948e-002
122	5.7232e-002
$R^2$	0.55
<i>adj. R</i> <sup>2</sup>	0.49
<i>p</i> -value	8.57e-7

Table 7.8: p-values for the age model.

## 7.5 Summary and discussion

In this chapter we have analyzed the LADIS images and clinical data for 50 subjects cross-sectionally. This has been accomplished using the framework presented in chapter 3. A brief summary and discussion of the key points follows.

### 7.5.1 Spatial normalization

We used the registration procedure outlined in chapter 4. The tensor B-spline approach used is a partially implicitly regularized approach that does not rely on a physical model for the registration. Using explicit regularization terms the regularization can be modified to the accommodate specific requirements that exist for the cross-sectional analysis. Because the registration has no physical model as a basis, the need for explicit regularization terms necessitates some parameter estimation.

The target for the registration was chosen to be one of the subjects.

The registration algorithm was able to capture the fundamental differences between subjects as visually inspected. At the same time, visual inspection showed that the deformations represented feasible transformations. Because of fundamentally different topology between subjects, the registration was unable to completely model differences in the finest brain structures, but the overall differences were modelled.

Artifacts were present in some of the images, however this seems to have affected the registration only to a small degree. The choice of a preprocessing filtering of the images appears to have been a good choice and has diminished the effect of the artifacts on the registration.

Because of the mentioned characteristics of the registration method, it is our opinion that it is well suited for registering one T1-weighted MR image to another, thereby capturing differences between brains with the goal of performing TBM.

### 7.5.2 Metric extraction

For the cross-sectional analysis, only the relative volume metric was employed. This was done due to the fact that the differences are so large that we expect the relative volume metric to be able to capture them in a satisfying manner. Additionally, the relative volume metric is directly interpretable.

With this, an atlas was generated, confirming that the registration approach is valid.

### 7.5.3 Statistical analysis

In the statistical analysis we have shown that TBM can be used to detect differences between subjects. Voxelwise tests have shown very localized effects that are to a degree affected by misalignments in the registration, despite the implicit smoothing of the B-spline representation. Using regional tests we have overcome this problem, however this provided less localized results.

Using a group test, we were able to examine differences in the mean of the relative volume metric for three grouping parameters.

The achieved results were correlated with a selection of clinical parameters, of which several showed significant correlation. For the global measures of differences in the volumes of CSF and gray/white matter, we observed the expected relationships: The amount of gray/white matter decreased with age and vice versa for CSF. Most of the clinical parameters exhibited correlation with a combined global atrophy measure.

Some of the clinical parameters seemed to be more regionally correlated. This suggests both that dividing the brain into volumes of interest and that the

approach using an atlas to achieve this is valid.

Visual inspection of the data showed large variations. One can imagine numerous reasons for this, and with a data set as small as the one we have worked with it is to be expected. For example, the anatomical atlas that we use does not provide direct functional information about the brain. If a more precise functional mapping of the brains could be provided, improved results would likely be seen.

The interpretation of the specific significant regional results are left to persons with a background within medicine. As is often the case with statistical results, causal inferences cannot necessarily be extracted from the results. This requires more knowledge of the specific relationships between cause and effect and ideally a controlled experiment.

We have shown models explaining both morphological changes with clinical parameters and vice versa. With the number of observations and dependent variables available to us, the results should be interpreted with some caution. There is a risk of obtaining spuriously significant results. This could be corrected for using several techniques (e.g. Bonferroni adjustment).

The modelling approach could be expanded to the so-called General Linear Model, including both multiple independent and dependent variables, to gain more insight into the relationships between the morphological differences and external factors.

# Results: Longitudinal study

---

In this chapter we apply the the methods described in earlier chapters to a longitudinal analysis of the LADIS data. The goal of the longitudinal analysis is to gauge changes to each of the subjects and compare these changes cross-sectionally.

To reiterate, the steps we take in the longitudinal analysis are:

1. Brain extraction on baseline images.
2. Spatial normalization of baseline images to a common reference.
3. Spatial normalization of followup images to their corresponding baseline image.
4. Transformation of the result from 3 into a common reference space using the results from 2.
5. Calculation of spatial derivatives (or measures derived from them) of the results from 4.
6. Statistical analysis of results.

Items 1 and 2 are already covered in chapter 7, so in this chapter we concentrate on the steps that are unique or different for the longitudinal analysis.

For the longitudinal analysis only 27 image pairs are available. This is due to data availability issues. It is also worth noting that the followup images are of a generally worse quality than the baseline images, many of them exhibiting clear signs of motion artifacts and general noise (see section 2.1.5 on page 5).

## 8.1 Spatial normalization within subjects

Having completed the preceding steps, we can proceed with the spatial normalization by registration. Much of the registration process is similar to that of the cross-sectional analysis. There are however a few key points that need to be discussed.

### 8.1.1 Registration target

The target image is naturally one of the two that are available for each subject. We choose to use the baseline image as the target. Doing this allows us to use the already existing cross-sectional registrations described in chapter 7 to negate the effects of between subject variability when comparing longitudinal changes cross-sectionally (see section 8.2).

### 8.1.2 Image filtering and similarity measure

As in the cross-sectional analysis we choose to filter the images with a gaussian kernel to achieve less influence from noise. Because we are working with the same images the kernel width is chosen to be the same with a FWHM of 0.75 mm. For the same reasons as given in the cross-sectional analysis, we choose to use NMI as the similarity measure.

### 8.1.3 Global registration

For the global registration it is important to choose which part of the images to base the registration on. As for the cross-sectional registration, there are a few obvious possibilities: Brain to brain, skull to skull, and head to head.

Because the registration is being performed within the same subjects, and the skulls can be expected to remain the same size for these subjects, the skull to skull registration is the natural choice.

A simple rigid registration is appropriate for the global registration — again because the skulls of grown adults can be expected to remain the same over a three year period and we wish to measure changes that might not be possible to detect if a complete affine transformation (including scaling) was used.

As for the global registration *between* subjects, the multi-resolution approach is well suited to ensure convergence to a global optimum.

#### 8.1.4 Local registration

Unlike in the cross-sectional registration we can expect the brains of the subjects to be very alike, since they are elderly subjects with completely developed brains. On the other hand we can expect that smaller changes have taken place, which means that the registration must be able model these small changes. For these reasons we choose to use a single level deformation grid with a control point spacing of 2 mm.

Furthermore, we expect that in general, topological changes will not occur (i.e. no folding of tissue). Because of this, we choose to use only the topology preserving penalty during the registration. The topology penalty is controlled by the parameter  $\lambda_3$ . We choose the parameter by performing registrations with different values of  $\lambda_3$  and calculating the relative volumes over the entire deformation field. If a field results in negative values of the relative volume (i.e. has a fold), the corresponding  $\lambda_3$  is rejected, and a higher one is chosen. This is repeated for a number of the images to ensure stability (see figure 8.1).

The value chosen for the registration is  $\lambda_3 = 0.00025$ , which lies well above the values where there are no longer any negative relative volumes. Choosing  $\lambda_3$  this high limits the pliability of the registration to a degree, but not more than is acceptable.

#### 8.1.5 Registration results

The result of the registrations are the transformations that transform each of the followup images into the corresponding baseline image. The validity of the registrations is verified by means of visual inspection of the transformed images

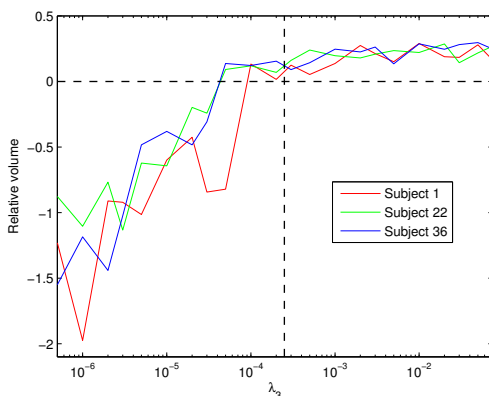


Figure 8.1: Choosing  $\lambda_3$  for the within subject registration. Three followup images have been registered to the corresponding baseline images with different values of  $\lambda_3$ . As  $\lambda_3$  increases, the magnitude of the smallest relative volume decreases. The dashed vertical line shows the chosen value of  $\lambda_3 = 0.00025$ .

and the deformation grids.

#### 8.1.5.1 Visual inspection of transformed images

Since the differences within subjects are so small, it is not very easy to inspect the images directly. Instead, we can inspect the difference between the baseline image and the transformed followup image. Examples of this can be seen in figure 8.2.

The inspection reveals some differences, but these are expected due to both noise, the implicit regularization of the B-spline and the topology preserving regularization. It is however clear that the transformation has to a high degree been able to model the actual changes. For example, the large expansions in the ventricular area of subject 1 have clearly been modelled.

#### 8.1.5.2 Visual inspection of deformation grids

To ensure that the deformation grids represent plausible transformations, we inspect the grids. This inspection shows that the grids are all well behaved (no folds etc.). A few examples can be seen in figure 8.3.



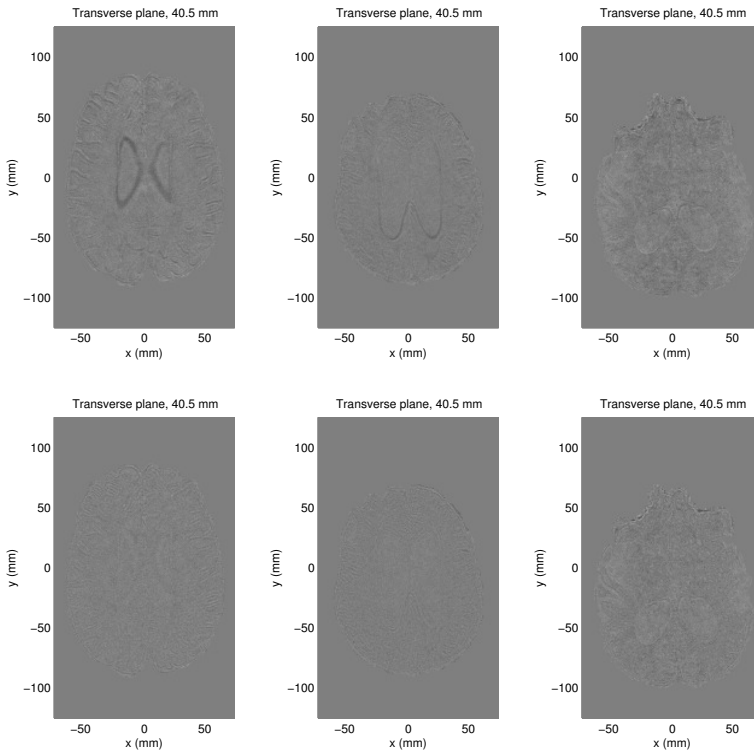


Figure 8.2: Registration of different subjects to target. Top row: Difference images after global registration. Bottom row: Difference images after local registration. From left to right: Subject 1, subject 16, subject 38.

Visual inspection reveals that all of the deformation grids are well behaved.

## 8.2 Metric extraction

For the longitudinal data we choose to use both the relative volume metric and the Log-Euclidean metrics. This choice is made because we expect within subject changes to be small and perhaps exhibit anisotropy, and as such the relative volumes might not be sufficient to detect changes fully.

The longitudinal registration results can be analyzed using two different approaches: In the space of each baseline image or in the space of the target in

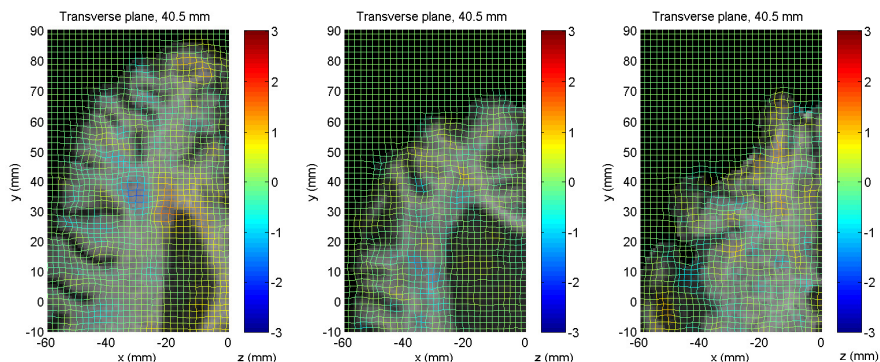


Figure 8.3: Crop of deformation grids for registrations of different subjects to target overlaid on the transformed images. From left to right: Subject 1, subject 16, subject 38.

the cross-sectional analysis (subject 2). Each approach has its advantages and disadvantages.

Extracting the information to baseline space has the advantage of preserving spatial information about deformations, so that we can relate the information directly to the subject image. However, taking this approach makes it impossible to compare changes between subjects.

Extracting the information to the cross-sectional target space has the advantage of normalizing the information to a common spatial frame, so that we can make cross-sectional inferences about changes within subjects. This does however introduce a need for transforming the within subject transformation, such that it is difficult to spatially relate the changes to the subject images.

To ensure the best outcome of the longitudinal analysis, we take both approaches, choosing the appropriate one for specific tasks.

### 8.2.1 Extracting to baseline space

Since the longitudinal transformations exist in the space of the baseline images, extracting the Jacobian to baseline space is equivalent to the extraction into target space for the cross-sectional registrations.

Following calculation of the Jacobian matrix, both the relative volumes and the

Log-Euclidean metrics can be extracted. For the relative volumes, this is done in the same way as for the cross-sectional study. The idea is basically the same for the Log-Euclidean metrics, except that the end result is a tensor field where a six-dimensional vector is associated with every point in space.

### 8.2.2 Extracting to cross-sectionally normalized space

As described in the previous section, the transformations exist in the coordinate space of the baseline images. To enable us to make cross-sectional inferences on the longitudinal data, we can transform the transformations into the space of baseline subject 2, using the transformations obtained in the cross-sectional analysis.

The order in which we accomplish this is crucial to the precision of the results. We could elect to first extract the Jacobians from the longitudinal transformations, and then transform these with the cross-sectional transformations. This would, however, result in a need for interpolation, which in turn would lead to lower precision in the results. A suitable interpolation algorithm would also need to be chosen, and the correct choice is not trivially obvious.

Instead, we choose to transform a sampling grid located in the space of subject 2 into the space of each baseline image (using the cross-sectional transformations), and calculate the Jacobian of the longitudinal transformation in each transformed grid point. Using the notation introduced in chapter 3, this becomes

$$\mathbf{J}_{total} = \mathcal{J}(\mathbf{T}_{total}) = \mathcal{J}(\mathbf{T}_{cross}(\mathbf{T}_{long})),$$

where  $\mathbf{J}_{total}$  is in the same space as the cross-sectional target (subject 2). The process is illustrated in figure 8.4.

Following this, both the relative volume metric and Log-Euclidean metric can be extracted from the calculated Jacobians.

### 8.2.3 Distributions

After calculating the relative volumes as described, we start by inspecting their distribution to evaluate the assumptions about normality that will be used in the later analysis. First, we view histograms of both the raw data and the logarithmically transformed data (figure 8.5).

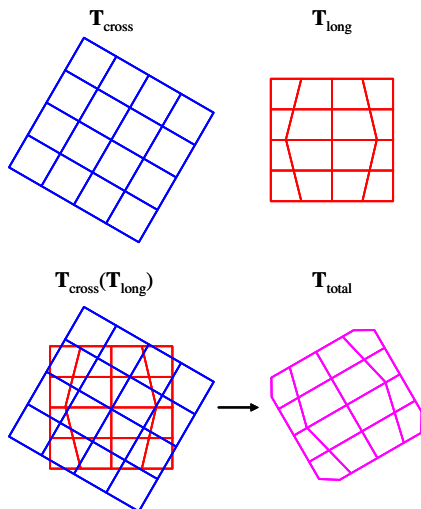


Figure 8.4: Transforming the within subject transformation into a common space.

From the histograms it is not clear which is most normally distributed. Using probability plots, we inspect this more closely (figure 8.6).

From the probability plots it is clear that the normal distribution is not a good match. Although the plots show clear signs of tails when comparing to the lognormal distribution, it is clearly more evenly distributed and as such a better choice for the further analysis. Because of this, we choose to transform the raw relative volume data with a logarithmic transformation, even though it will give some falsely significant values in the later statistical analysis.

For the Log-Euclidean metrics, we can inspect the histogram of each of the six vector components (figure 8.7).

The histograms all exhibit normal tendencies, making the assumptions in the later statistical tests valid.

## 8.2.4 Building a change atlas

There are many ways to visualize the data collected in the information extraction. An intuitive way is to construct a change atlas — an atlas that captures the “mean” change of the population. This can be done using the cross-sectionally

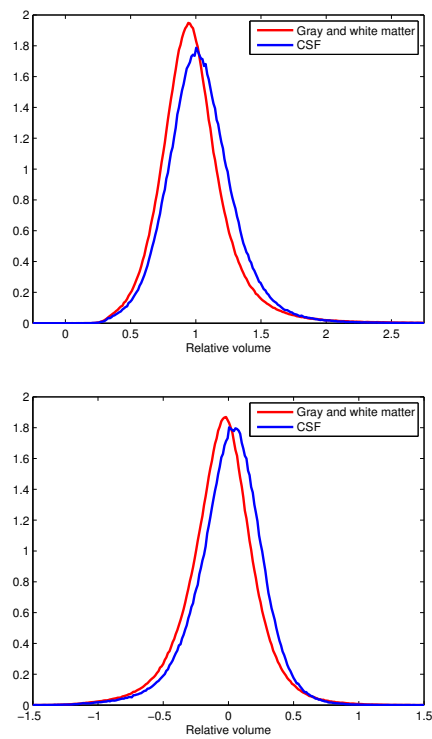


Figure 8.5: Histograms of relative volumes.

normalized relative volume data. This reveals some useful results (see figure 8.8).

The most noticeable changes happen in the CSF of the ventricular system, where a clear tendency for expansion is seen. To a lesser degree contractions in gray and white matter can be seen, especially in the area surrounding the ventricles.

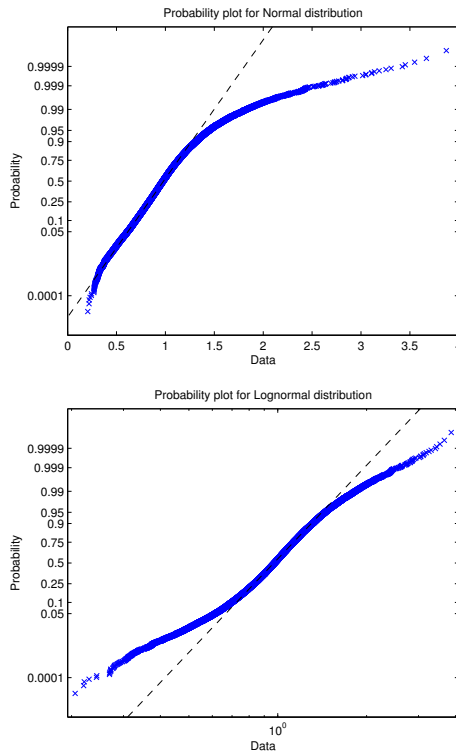


Figure 8.6: Probability plot against the normal distribution (left) and lognormal distribution (right).

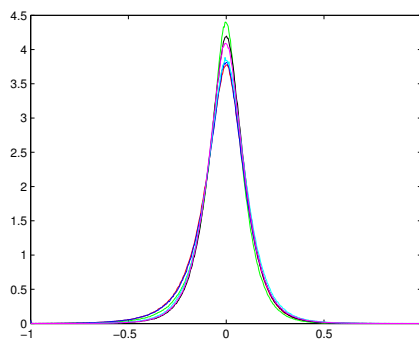


Figure 8.7: Histograms of each of the six Log-Euclidean components.

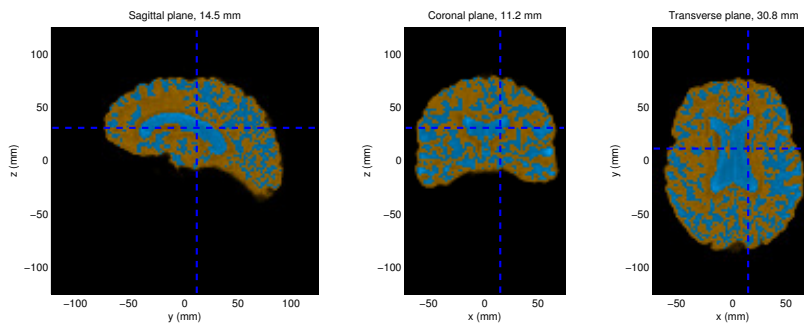


Figure 8.8: Three slices of a change atlas. The mean of the normalized volumes of relative volumes of all 27 subjects. Blue indicates expansion, brown indicates contraction.

## 8.3 Statistical analysis

In this section we give some examples of how the data from the metric extraction can be analyzed. As mentioned above, the goal is twofold: To find changes within subjects and to compare these changes cross-sectionally. From the metric extraction step two sets of data are available - one in baseline space and one in cross-sectionally normalized space.

The difference might not be obvious, but there is a distinction in the results that are achieved. The first will find areas of significant changes compared to the general changes that happen in the same subject, while the second will find areas of significant changes compared to the changes that happen in the same area of all the subjects.

### 8.3.1 Data in baseline space

For the data in baseline space, we carry out a per voxel test. In the per voxel test, each subject is tested individually for significant changes on the assumption that the norm is that nothing happens within a subject brain. In this way, statistics are calculated for the entire volume of a single subject, and each voxel is tested using these statistics. This can be done both within the relative volume framework and the Log-Euclidean framework.

#### 8.3.1.1 Relative volumes

For each of the subjects, statistics (mean and standard deviation) are calculated, and every voxel is assigned a  $Z$  score and a p-value according to these statistics. The result is, for each subject, a volume of p-values that indicates how likely the change in each voxel is to have happened compared to the changes in all the other voxels of the same subject.

Figure 8.9 shows an example of a baseline and followup image from one subject where a significant change has taken place during the period between the baseline and the followup assessment. The morphological change is captured by the registration procedure and the volume of p-values is calculated (see figure 8.10). Although the area around the infarction is found to be significant the result is quite noisy and scattered and the effects are not very evident.



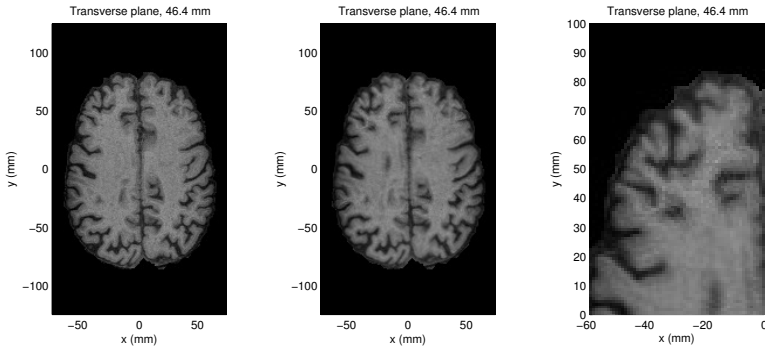


Figure 8.9: The left image shows the baseline data from subject 1 and the corresponding followup image and shown in the middle. The right image is a crop of the followup image focused on the significant change. Notice the cortical infarction (the black spot that has appeared in the followup image at  $(-30, 35)$ ).

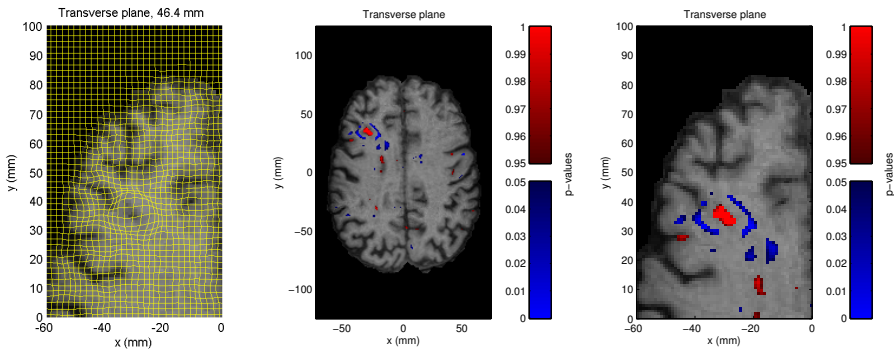


Figure 8.10: Left image: The deformation grid shown together with the transformed image. Middle image: Significant differences in  $\log(V_{rel})$  overlaid on the transformed image. The overlay shows  $p < 0.05$  and  $p > 0.95$  in blue and red respectively. Right image: Crop of the middle image.

### 8.3.1.2 Log-Euclidean metrics

To improve this result, we employ the Log-Euclidean metrics. To calculate the p-values as we did in the relative volume framework we use the Hotelling  $T^2$  statistics using the mean and covariance matrix of the six-dimensional Log-Euclidean vectors. This reduces the data to one-dimensional sizes. By a logarithmic transformation the distribution becomes approximately normal (see figure 8.11). This is implemented in the Matlab script `makelestats.m` (see

appendix E, page 120).

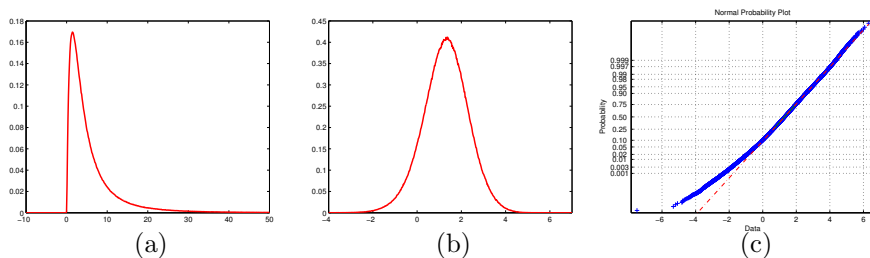


Figure 8.11: (a): The distribution of the  $T^2$ -values. (b): The distribution of the logarithmic transformed  $T^2$ -values. (c): Normal probability plot of the logarithmic transformed  $T^2$ -values.

In contrast to the relative volume, values smaller than the mean no longer represents contraction. In the Log-Euclidian framework they represent that nothing happens. This means that the test for significant changes is one-sided and not two-sided as in the relative volume framework. Applying this multivariate statistical test to the example above gives different results (see figure 8.12) Because

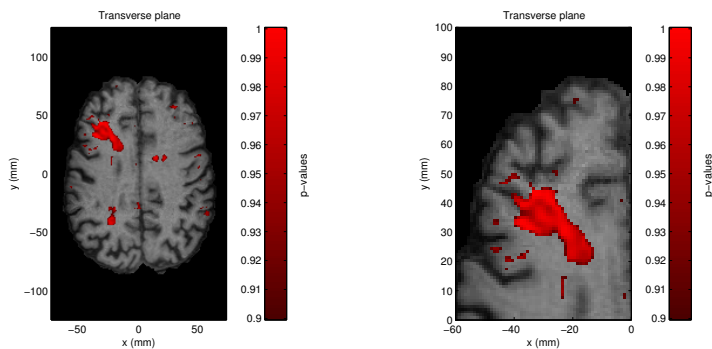


Figure 8.12: Left image: Significant differences in using the Log-Euclidean framework overlaid on the transformed image. Right image: Crop from of left image. The overlay shows  $p > 0.9$ . Compare this to figure 8.10

of the increased significance of previously insignificant values the area around the infarction appears as one connected component. The morphological change becomes very clear using this method.

To further investigate the differences between the Log-Euclidean framework and the relative volume framework two more cases are studied: Subject 11 and 22. As subject 1 these two subjects exhibit large changes in the selected areas.

## Subject 11

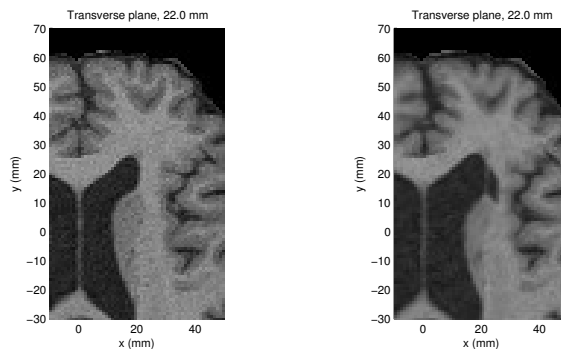


Figure 8.13: Crop from transverse slice in subject 11. The left image shows the baseline data and the right shows the followup. Notice the periventricular infarction (the black extension of the ventricle at (20, 20) of the followup image).

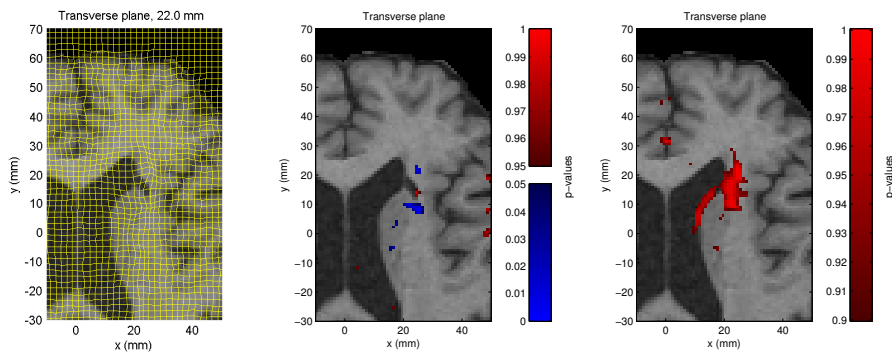


Figure 8.14: Left image: The deformation grid shown together with the transformed image. Middle image: p-values using the relative volume framework. Right image: p-values using the Log-Euclidean framework.

As can be seen in both the image and to some degree in the overlaid deformation grid a large change has occurred. The relative volume framework does not capture this very well. In contrast the morphological change is detected as significant by the Log-Euclidean framework.

## Subject 22

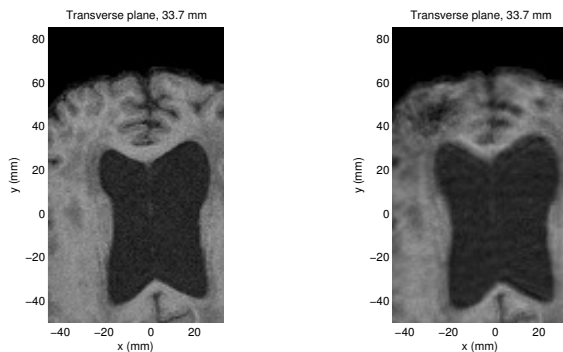


Figure 8.15: Crop from transverse slice in subject 22. The left image shows the baseline data and the right shows the followup. Notice the major infarction at  $(-30, 40)$  in the followup image and the enlargement of the ventricles.

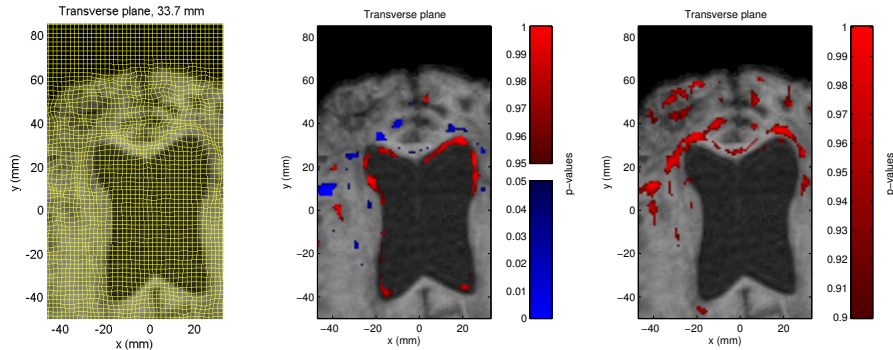


Figure 8.16: Left image: The deformation grid shown together with the transformed image. Middle image: p-values using the relative volume framework. Right image: p-values using the Log-Euclidean framework.

In this case both the image and the deformation grid also show a clear change, however, the captured effects are different between the two frameworks. The relative volume framework seems to capture the expansion of the ventricles well while being unable to detect the infarction. Using the Log-Euclidean framework both the infarction and the expansion of the ventricles are detected.

### 8.3.2 Cross-sectionally aligned data

For the cross-sectionally aligned data, two analyses are carried out:

- Per voxel test
- Regional test

In addition to these tests, we can test for correlation with some of the clinical measurements that are available from the LADIS study (age, BMI, etc.).

#### 8.3.2.1 Per voxel test

In the per voxel test, each relative volume voxel is treated as a separate observation  $V_{rel}$ , and is tested cross-sectionally across the 27 subjects for significance. Under the assumption that in each voxel, across the subjects, the data is log-normally distributed (as investigated in section 8.2), each voxel can be assigned a  $Z$  score and a  $p$ -value can be found. Since we are interested in studying both significant expansions and contractions, a two-sided test is employed.

For each subject this gives a volume containing the probability that for a given relative volume voxel tells us how likely an outcome as or more extreme is to have happened compared to the rest of the subjects (see figure 8.17).

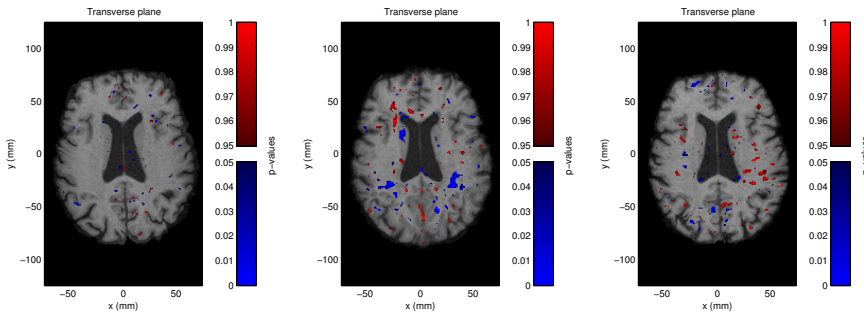


Figure 8.17: Significant changes in  $\log(V_{rel})$  overlaid on normalized images. The overlay shows  $p < 0.05$  and  $p > 0.95$  in blue and red respectively. From left to right: Subject 1, subject 16, subject 38.

The results seem somewhat noisy. Due to the fact that the within subject changes are quite small and localized, the noise could be an artifact from the

between subject normalization. A small shift in the location of a voxel can result in a large change in a p-value because the calculation of the p-value is based on the assumption that every corresponding voxel is spatially coinciding.

For the above reason, we elect not to use the Log-Euclidean metric for this test, since it is unlikely to yield less noisy results.

### 8.3.2.2 Regional test

To alleviate the problems with the voxelwise test, we can (as for the cross-sectional analysis) divide the brain into a number of VOIs, and for each of these compare the mean relative volume cross-sectionally.

As for the cross-sectional analysis, the LPBA40 atlas is used to partition the images into VOIs. For details on how the partitioning is accomplished, see section 7.4.2 on page 65. Example results are shown in figure 8.18. It is obvious

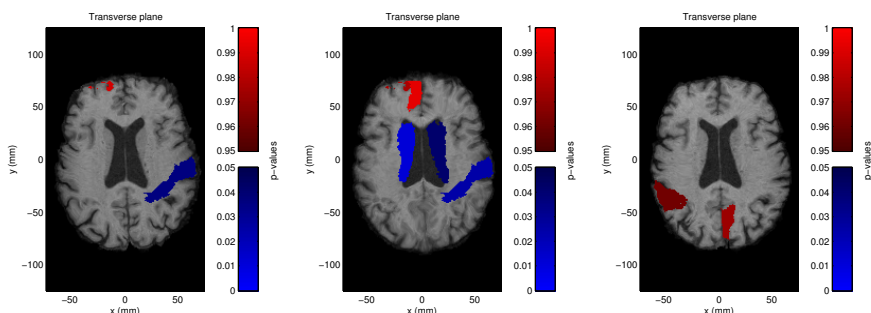


Figure 8.18: Significant changes in regional  $\log(V_{rel})$  overlaid on normalized images. The overlay shows  $p < 0.05$  and  $p > 0.95$  in blue and red respectively. From left to right: Subject 1, subject 16, subject 38.

that the noise is reduced, however it is difficult to compare the result directly to the per voxel test because of the influence of the third dimension. The maps do however give a good indication of areas where changes have happened.

## 8.4 Clinical correlation

As we did in the analysis of the cross-sectional registrations we can correlate the data from the longitudinal registrations with the clinical parameters. We now

correlate the clinical parameters with the morphological changes within each subject as opposed to the cross-sectional analysis where we correlated clinical parameters with differences *between* subjects.

A number of options for which parameters should be chosen are available: The baseline parameters, the followup parameters, the difference between the baseline and followup parameters, etc. An intuitive choice is to select the difference between the baseline and followup parameters. This way we can correlate the changes in the brain with the changes in the clinical parameters. For the eight parameters we have chosen, however, this is not feasible for all of them.

When the clinical parameters are measured during the third year followup session it is the fourth time the patients are evaluated. This means that the subjects are familiar with the tests compared to the baseline evaluations. For example the mean of the walking speed has increased during the three years. This is certainly not to be expected for elderly subjects.

To get a meaningful parameter measure that represents the period over which the longitudinal changes has taken place we calculate the mean of the baseline and the followup assessment. The means of these parameters are then correlated with the global atrophy. The result of this is summarized in table 8.1.

Clinical parameter	$\mu_{gw}$		$\mu_{csf}$		$\mathcal{A}_{combined}$	
	Pearson	Spearman	Pearson	Spearman	Pearson	Spearman
Age	$r=0.100$ $p=6.21e-1$	$\rho=0.045$ $p=8.25e-1$	$r=-0.101$ $p=6.18e-1$	$\rho=-0.034$ $p=8.68e-1$	$r=0.106$ $p=6.00e-1$	$\rho=0.037$ $p=8.56e-1$
BP <sub>sys</sub>	$r=-0.094$ $p=6.42e-1$	$\rho=-0.193$ $p=3.35e-1$	$r=0.436$ $p=2.31e-2$	$\rho=0.458$ $p=1.64e-2$	$r=-0.248$ $p=2.13e-1$	$\rho=-0.337$ $p=8.53e-2$
BP <sub>dia</sub>	$r=-0.015$ $p=9.42e-1$	$\rho=-0.054$ $p=7.90e-1$	$r=0.360$ $p=6.50e-2$	$\rho=0.321$ $p=1.02e-1$	$r=-0.156$ $p=4.36e-1$	$\rho=-0.150$ $p=4.54e-1$
BMI	$r=-0.038$ $p=8.50e-1$	$\rho=0.051$ $p=7.99e-1$	$r=-0.186$ $p=3.53e-1$	$\rho=-0.202$ $p=3.11e-1$	$r=0.056$ $p=7.83e-1$	$\rho=0.096$ $p=6.33e-1$
Stroop2s	$r=-0.491$ $p=1.47e-2$	$\rho=-0.403$ $p=5.06e-2$	$r=0.269$ $p=2.04e-1$	$\rho=0.197$ $p=3.57e-1$	$r=-0.444$ $p=2.96e-2$	$\rho=-0.357$ $p=8.69e-2$
Trail1s	$r=-0.264$ $p=1.92e-1$	$\rho=-0.105$ $p=6.08e-1$	$r=0.133$ $p=5.18e-1$	$\rho=0.039$ $p=8.50e-1$	$r=-0.226$ $p=2.67e-1$	$\rho=-0.088$ $p=6.69e-1$
Verbal	$r=0.357$ $p=6.72e-2$	$\rho=0.369$ $p=5.82e-2$	$r=-0.246$ $p=2.16e-1$	$\rho=-0.244$ $p=2.21e-1$	$r=0.344$ $p=7.87e-2$	$\rho=0.368$ $p=5.87e-2$
Walking speed	$r=-0.208$ $p=3.08e-1$	$\rho=-0.155$ $p=4.50e-1$	$r=0.354$ $p=7.62e-2$	$\rho=0.306$ $p=1.29e-1$	$r=-0.291$ $p=1.49e-1$	$\rho=-0.223$ $p=2.74e-1$

Table 8.1: Correlation coefficients between the mean of the clinical baseline and the followup parameters, and relative volume changes of gray and white matter ( $\mu_{gw}$ ), CSF ( $\mu_{csf}$ ), and the combined atrophy measure ( $\mathcal{A}_{combined}$ ). The correlation coefficients,  $r$ , with a magnitude  $> 0.25$  is shaded in addition to the  $p$ -values  $< 0.05$

Only a few correlations turn out to be significant ( $p < 0.05$ ). This may be due

to the decreased number of subjects in the longitudinal analysis (27 vs. 50 in the cross-sectional analysis) combined with a large variance of the parameters.

In the correlation between CSF and blood pressure a positive correlation is found. For the combined atrophy measure a negative correlation with the stroop parameter and a positive correlation with the verbal parameter is found. All of these result is according to what could be expected. More surprising is it that a negative correlation between atrophy and walking speed is found.

As for the cross-sectional analysis we can subdivide the brain volume into lobe volumes to inspect if this can reveal additional information. In general the result of doing this is that no significant correlations are found. The few significant correlations found might as well have been obtained by chance because of the high number of correlation tests rather than because of actual correlation.

## 8.5 Discussion

In this chapter we have analyzed the LADIS images and clinical data longitudinally. This has been accomplished using the framework presented in chapter 3. A brief summary and discussion of the key points follows.

### 8.5.1 Spatial normalization

As for the cross-sectional analysis, the tensor product B-spline approach was taken to the registration problem. Due to the expected changes we have chosen to use an explicit regularizer that ensures topology preservation. To ensure that the registration was not overregularized, we chose the penalty parameter as low as possible. However, because of the resulting non-monotonicity as a function of the penalty parameter, we had to choose a relatively large regularizing penalty. Despite this, the registration was able to sufficiently model the observed changes.

Due to the implicit regularization of the tensor product B-spline approach very sharp and localized changes are not fully modelled.



### 8.5.2 Metric extraction

Two approaches to extracting the Jacobian were presented, one where the results were located in the baseline space of each subject and one where all of the results were spatially normalized to one of the subjects. Each has its uses — the former can be used to accurately gauge changes in one subject, while the latter can be used to conduct cross-sectional change comparisons.

The magnitude and shape of the changes that are expected longitudinally are such that we chose to investigate both the relative volume metric and the Log-Euclidean metric.

With the relative volume metric, we constructed a change atlas, showing where contractions and expansions are most likely to happen. The atlas confirms the validity of both the registration approach and the relative volume metric in showing a general tendency for expansion in the ventricular system.

### 8.5.3 Statistical analysis

In the statistical analysis we have shown that TBM can be used to detect changes within subjects. In baseline subject space, we compared changes voxelwise to the general changes within the same subject. Doing this enabled us to locate areas showing significant changes. In this context, the Log-Euclidean approach was better at capturing significant changes (e.g. infarctions). In the Log-Euclidean framework it was possible to detect changes even when the deformation apparently did not fully model the change. A drawback to the Log-Euclidean metric is that it is not as intuitively interpretable as the relative volume metric.

For the between subject analysis we showed that the voxelwise test yielded very noisy results, that were influenced by both the low number of subjects and the possible small misalignments from the cross-sectional registration. This was to a large degree alleviated by the use of regional testing.

The achieved results were correlated with a selection of clinical parameters. Some of these showed correlation, however most of the correlations were not significant. The lack of correlation is likely to be caused by the comparatively low number of subjects that was analyzed. Because of the lack of significant correlations, we elected not to study more complex models to avoid obtaining spuriously significant models.



# Conclusion

---

The purpose of this project has been to investigate the possibility of analyzing the image data from the pan-European LADIS study using neuromorphometry. We have described the prevalent methods and analyzed their individual advantages and disadvantages. On the basis of this analysis we have selected a relatively new method, tensor-based morphometry (TBM), which still has many unexplored properties.

To facilitate TBM analysis two frameworks have been suggested — one for cross-sectional analysis and one for longitudinal analysis. Both frameworks share certain components: Registration, metric extraction, and statistical analysis.

For the registration, both a global method based on an affine transformation and a local free form deformation method based on an explicitly and implicitly regularized tensor product B-spline have been described. This approach was selected to avoid basing the registration on a physical model which might have introduced undesirable properties in the resulting deformation.

The properties of the registration that are desirable for respectively the cross-sectional and longitudinal studies have been analyzed. The registration method has been adapted to satisfy each of these requirement sets and applied successfully to each study type. The registration method has proven itself sufficiently robust to prevalent MRI artifacts. From the cross-sectional registrations an

atlas has been constructed.

Two different metrics for analyzing the registration results have been chosen and described: Relative volumes and Log-Euclidean metrics. The relative volume metric is easily interpretable as it reduces the available information to a single value describing contractions and expansions. This, however, also removes shape information (e.g. anisotropy). The Log-Euclidean metric preserves this information while remaining in a vector space where ordinary multivariate statistics can be used for analysis.

The properties of each of the metrics have been investigated and the usefulness in different settings evaluated. Compared to the relative volume metric, the Log-Euclidean metric results in better detection of neuromorphological changes. From the relative volume metric a change atlas has been constructed.

We have shown that differences between the sexes are possible to detect using the described methods, while other grouping parameters (e.g. handedness) revealed no significant separation.

The relative volume metric has been correlated with clinical data in a number of ways, both in the cross-sectional and longitudinal study. The largest and most significant correlations were observed in the cross-sectional analysis, while the longitudinal analysis revealed less decisive results.

Through the results we conclude that the proposed framework of methods is viable for neuromorphometry. Through the framework it is possible to detect both general atrophy and pathologies in single subjects and differences between subjects which can be correlated with clinical parameters.

It would be interesting to apply the proposed frameworks to the complete LADIS data set. We expect that doing this would reveal much more significant correlations with clinical data and that more useful and revealing models could be established.

Of further interest could be the use of others metrics in the framework. The best choice of a metric is likely to depend on the developmental process that is being analyzed.

# LADIS criteria

---

## A.1 Inclusion criteria

- Age between 65 and 84
- Changes of cerebral subcortical white matter on CT/MRI, of any degree, from mild to severe according to the categorization into the 3 severity classes of the Fazekas et al.'s scale [30]
- No or mild disability as assessed by the Instrumental Activities Daily Living (IADL) scale [31], (IADL score =1 in all the items or =1 in all the items except one > 1)
- Presence of a regularly contactable informant

## A.2 Exclusion criteria

- Subjects likely prone to drop-out in relation to the presence of severe illnesses (cardiac, hepatic, or renal failure, neoplastic, or other relevant systemic disease) possibly interfering with follow-up assessment
- Severe unrelated neurological diseases

- Leukoencephalopathies revealed by brain imaging, that turn out to be of non-vascular origin (immunologic- demyelinating, metabolic, toxic, infectious)
- Severe psychiatric disorders
- Inability to give informed consent
- Inability or refusal to undergo cranial MRI scanning

# APPENDIX B

## Atlas images

---

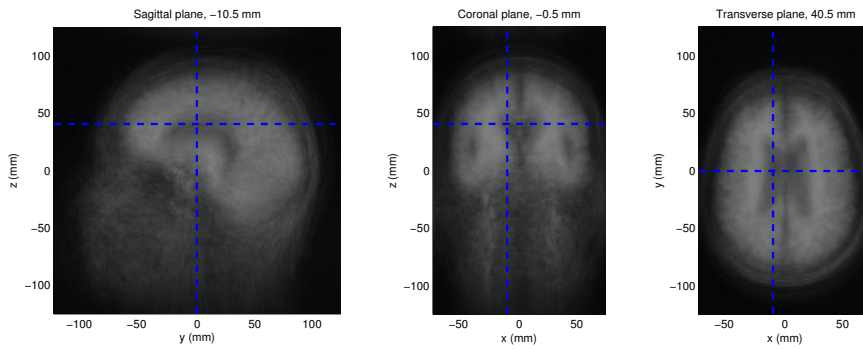


Figure B.1: Atlas made from source images.

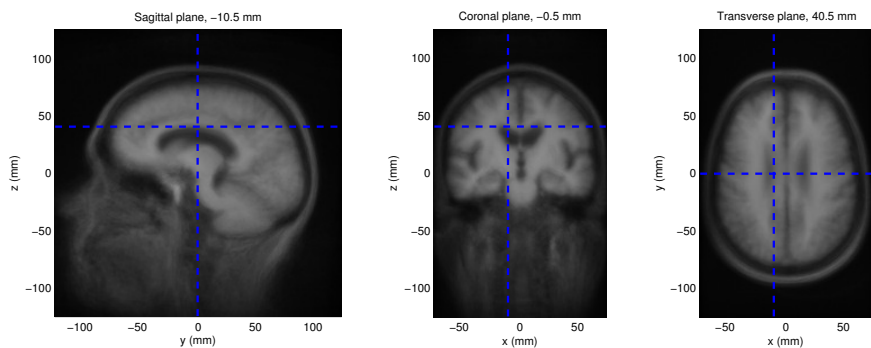


Figure B.2: Atlas made from globally registered images.

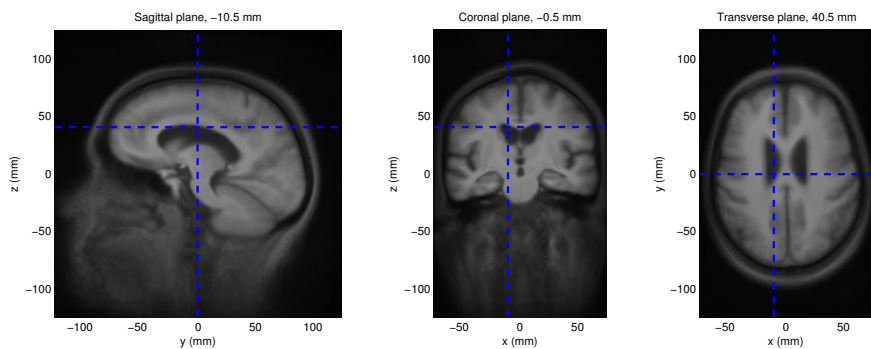


Figure B.3: Atlas made from locally registered images with a grid spacing of 32 mm.

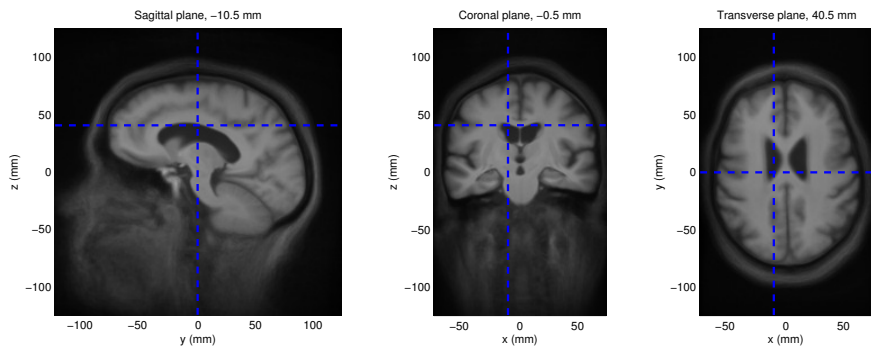


Figure B.4: Atlas made from locally registered images with a grid spacing of 16 mm.



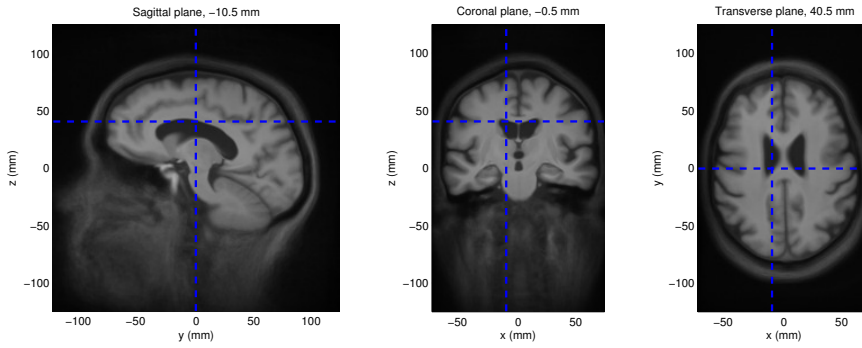


Figure B.5: Atlas made from locally registered images with a grid spacing of 8 mm.

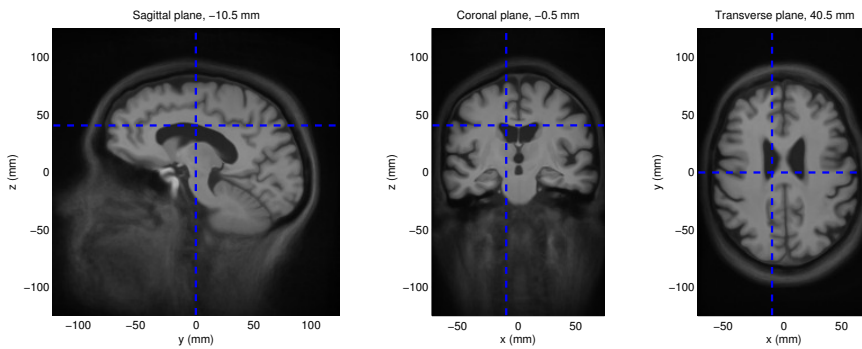


Figure B.6: Atlas made from locally registered images with a grid spacing of 4 mm.



## APPENDIX C

**LPBA40 labels**

---

ID	Area	Lobe
0	unlabeled	-
21	left superior frontal gyrus	Frontal
22	right superior frontal gyrus	Frontal
23	left middle frontal gyrus	Frontal
24	right middle frontal gyrus	Frontal
25	left inferior frontal gyrus	Frontal
26	right inferior frontal gyrus	Frontal
27	left precentral gyrus	Frontal
28	right precentral gyrus	Frontal
29	left middle fronto orbital gyrus	Frontal
30	right middle fronto orbital gyrus	Frontal
31	left lateral fronto orbital gyrus	Frontal
32	right lateral fronto orbital gyrus	Frontal
33	left gyrus rectus	Frontal
34	right gyrus rectus	Frontal
41	left postcentral gyrus	Parietal
42	right postcentral gyrus	Parietal
43	left superior parietal gyrus	Parietal
44	right superior parietal gyrus	Parietal
45	left supramarginal gyrus	Parietal
46	right supramarginal gyrus	Parietal

47	left angular gyrus	Parietal
48	right angular gyrus	Parietal
49	left precuneus	Parietal
50	right precuneus	Parietal
61	left superior occipital gyrus	Occipital
62	right superior occipital gyrus	Occipital
63	left middle occipital gyrus	Occipital
64	right middle occipital gyrus	Occipital
65	left inferior occipital gyrus	Occipital
66	right inferior occipital gyrus	Occipital
67	left cuneus	Occipital
68	right cuneus	Occipital
81	left superior temporal gyrus	Temporal
82	right superior temporal gyrus	Temporal
83	left middle temporal gyrus	Temporal
84	right middle temporal gyrus	Temporal
85	left inferior temporal gyrus	Temporal
86	right inferior temporal gyrus	Temporal
87	left parahippocampal gyrus	Temporal
88	right parahippocampal gyrus	Temporal
89	left lingual gyrus	-
90	right lingual gyrus	-
91	left fusiform gyrus	Temporal
92	right fusiform gyrus	Temporal
101	left insular cortex	-
102	right insular cortex	-
121	left cingulate gyrus	-
122	right cingulate gyrus	-
161	left caudate	-
162	right caudate	-
163	left putamen	-
164	right putamen	-
181	cerebellum	-
182	brainstem	-

APPENDIX D

# Cross-sectional correlations in the lobes

---

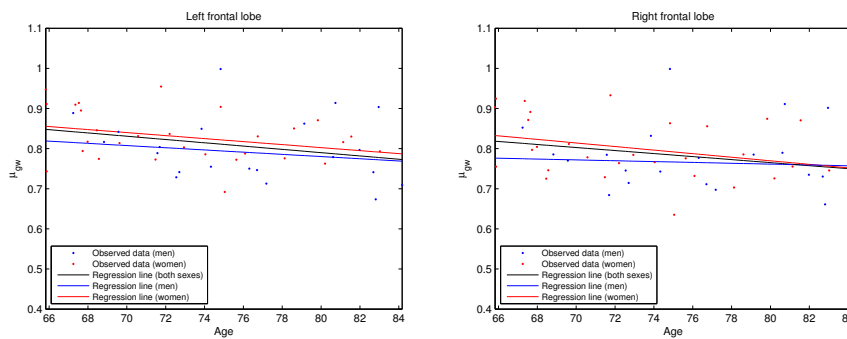


Figure D.1: Correlation between age and the relative volumes of the frontal lobes.

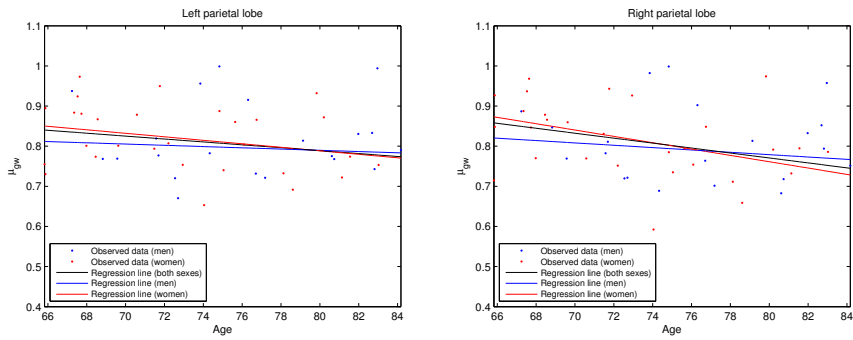


Figure D.2: Correlation between age and the relative volumes of the parietal lobes.

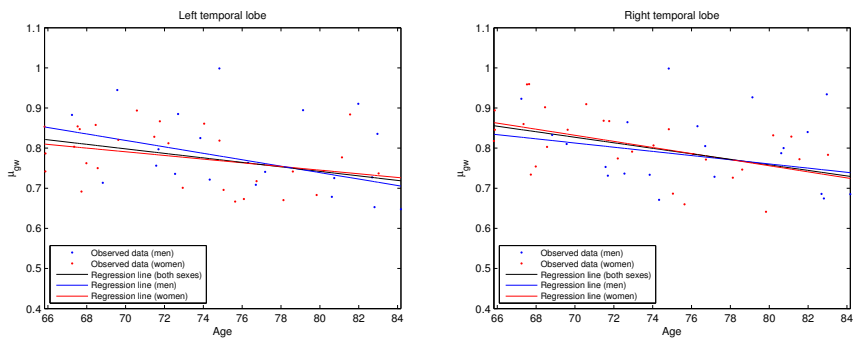


Figure D.3: Correlation between age and the relative volumes of the temporal lobes.

Lobe	$\mu_{gw}$ (both sexes)		$\mu_{gw}$ (men)		$\mu_{gw}$ (women)	
	Pearson	Spearman	Pearson	Spearman	Pearson	Spearman
Left frontal	$r=0.069$ $p=6.40e-1$	$\rho=0.082$ $p=5.76e-1$	$r=-0.030$ $p=9.01e-1$	$\rho=0.032$ $p=8.94e-1$	$r=0.226$ $p=2.39e-1$	$\rho=0.205$ $p=2.85e-1$
Right frontal	$r=0.092$ $p=5.29e-1$	$\rho=0.045$ $p=7.57e-1$	$r=0.010$ $p=9.66e-1$	$\rho=-0.194$ $p=4.12e-1$	$r=0.210$ $p=2.75e-1$	$\rho=0.167$ $p=3.86e-1$
Left parietal	$r=-0.081$ $p=5.83e-1$	$\rho=-0.021$ $p=8.87e-1$	$r=-0.310$ $p=1.96e-1$	$\rho=-0.163$ $p=5.04e-1$	$r=0.061$ $p=7.52e-1$	$\rho=0.095$ $p=6.26e-1$
Right parietal	$r=-0.024$ $p=8.69e-1$	$\rho=-0.053$ $p=7.20e-1$	$r=-0.033$ $p=8.88e-1$	$\rho=-0.118$ $p=6.10e-1$	$r=0.003$ $p=9.88e-1$	$\rho=0.014$ $p=9.43e-1$
Left occipital	$r=-0.068$ $p=6.52e-1$	$\rho=-0.057$ $p=7.01e-1$	$r=-0.071$ $p=7.67e-1$	$\rho=-0.206$ $p=3.84e-1$	$r=-0.001$ $p=9.96e-1$	$\rho=0.050$ $p=8.05e-1$
Right occipital	$r=0.102$ $p=4.97e-1$	$\rho=0.118$ $p=4.29e-1$	$r=0.117$ $p=6.33e-1$	$\rho=0.126$ $p=6.07e-1$	$r=0.178$ $p=3.66e-1$	$\rho=0.156$ $p=4.29e-1$
Left temporal	$r=-0.041$ $p=7.80e-1$	$\rho=-0.004$ $p=9.79e-1$	$r=-0.002$ $p=9.94e-1$	$\rho=0.141$ $p=5.54e-1$	$r=-0.079$ $p=6.85e-1$	$\rho=-0.055$ $p=7.77e-1$
Right temporal	$r=-0.316$ $p=2.89e-2$	$\rho=-0.225$ $p=1.24e-1$	$r=-0.462$ $p=4.65e-2$	$\rho=-0.223$ $p=3.60e-1$	$r=-0.215$ $p=2.63e-1$	$\rho=-0.226$ $p=2.39e-1$

Table D.1: Correlation coefficients between blood pressure (systolic) and the relative volume of gray and white matter ( $\mu_{gw}$ ).

Lobe	$\mu_{gw}$ (both sexes)		$\mu_{gw}$ (men)		$\mu_{gw}$ (women)	
	Pearson	Spearman	Pearson	Spearman	Pearson	Spearman
Left frontal	$r=0.071$ $p=6.30e-1$	$\rho=0.033$ $p=8.22e-1$	$r=-0.039$ $p=8.69e-1$	$\rho=-0.121$ $p=6.11e-1$	$r=0.217$ $p=2.58e-1$	$\rho=0.213$ $p=2.67e-1$
Right frontal	$r=0.085$ $p=5.63e-1$	$\rho=-0.045$ $p=7.57e-1$	$r=-0.028$ $p=9.06e-1$	$\rho=-0.290$ $p=2.16e-1$	$r=0.209$ $p=2.76e-1$	$\rho=0.103$ $p=5.97e-1$
Left parietal	$r=-0.103$ $p=4.82e-1$	$\rho=-0.112$ $p=4.43e-1$	$r=-0.392$ $p=8.75e-2$	$\rho=-0.452$ $p=4.56e-2$	$r=0.115$ $p=5.52e-1$	$\rho=0.195$ $p=3.10e-1$
Right parietal	$r=0.042$ $p=7.72e-1$	$\rho=-0.030$ $p=8.40e-1$	$r=-0.034$ $p=8.84e-1$	$\rho=-0.184$ $p=4.24e-1$	$r=0.132$ $p=5.02e-1$	$\rho=0.127$ $p=5.21e-1$
Left occipital	$r=0.018$ $p=9.08e-1$	$\rho=-0.038$ $p=8.01e-1$	$r=-0.115$ $p=6.40e-1$	$\rho=-0.229$ $p=3.45e-1$	$r=0.186$ $p=3.53e-1$	$\rho=0.182$ $p=3.65e-1$
Right occipital	$r=0.165$ $p=2.51e-1$	$\rho=0.129$ $p=3.72e-1$	$r=-0.059$ $p=8.01e-1$	$\rho=-0.158$ $p=4.93e-1$	$r=0.454$ $p=1.33e-2$	$\rho=0.472$ $p=9.76e-3$
Left temporal	$r=-0.073$ $p=6.19e-1$	$\rho=-0.042$ $p=7.77e-1$	$r=-0.092$ $p=7.01e-1$	$\rho=-0.029$ $p=9.04e-1$	$r=-0.053$ $p=7.87e-1$	$\rho=0.038$ $p=8.44e-1$
Right temporal	$r=-0.258$ $p=7.63e-2$	$\rho=-0.191$ $p=1.93e-1$	$r=-0.487$ $p=3.45e-2$	$\rho=-0.333$ $p=1.64e-1$	$r=-0.108$ $p=5.78e-1$	$\rho=-0.041$ $p=8.32e-1$

Table D.2: Correlation coefficients between blood pressure (diastolic) and the relative volume of gray and white matter ( $\mu_{gw}$ ).

Lobe	$\mu_{gw}$ (both sexes)		$\mu_{gw}$ (men)		$\mu_{gw}$ (women)	
	Pearson	Spearman	Pearson	Spearman	Pearson	Spearman
Left frontal	$r=-0.398$ $p=4.67e-3$	$\rho=-0.383$ $p=6.54e-3$	$r=-0.690$ $p=5.42e-4$	$\rho=-0.660$ $p=1.50e-3$	$r=-0.239$ $p=2.21e-1$	$\rho=-0.147$ $p=4.53e-1$
Right frontal	$r=-0.334$ $p=2.03e-2$	$\rho=-0.341$ $p=1.78e-2$	$r=-0.602$ $p=4.95e-3$	$\rho=-0.651$ $p=2.40e-3$	$r=-0.233$ $p=2.32e-1$	$\rho=-0.169$ $p=3.89e-1$
Left parietal	$r=-0.426$ $p=2.30e-3$	$\rho=-0.406$ $p=3.84e-3$	$r=-0.632$ $p=2.12e-3$	$\rho=-0.586$ $p=6.14e-3$	$r=-0.310$ $p=1.08e-1$	$\rho=-0.270$ $p=1.64e-1$
Right parietal	$r=-0.433$ $p=2.12e-3$	$\rho=-0.454$ $p=1.19e-3$	$r=-0.596$ $p=4.36e-3$	$\rho=-0.621$ $p=3.28e-3$	$r=-0.328$ $p=9.47e-2$	$\rho=-0.338$ $p=8.49e-2$
Left occipital	$r=-0.421$ $p=3.23e-3$	$\rho=-0.449$ $p=1.53e-3$	$r=-0.573$ $p=8.31e-3$	$\rho=-0.594$ $p=6.72e-3$	$r=-0.381$ $p=4.99e-2$	$\rho=-0.365$ $p=6.19e-2$
Right occipital	$r=-0.308$ $p=2.93e-2$	$\rho=-0.308$ $p=2.98e-2$	$r=-0.467$ $p=3.29e-2$	$\rho=-0.414$ $p=6.31e-2$	$r=-0.362$ $p=5.36e-2$	$\rho=-0.348$ $p=6.51e-2$
Left temporal	$r=-0.482$ $p=6.10e-4$	$\rho=-0.494$ $p=4.13e-4$	$r=-0.583$ $p=8.76e-3$	$\rho=-0.611$ $p=6.52e-3$	$r=-0.456$ $p=1.48e-2$	$\rho=-0.441$ $p=1.97e-2$
Right temporal	$r=-0.398$ $p=4.64e-3$	$\rho=-0.402$ $p=4.18e-3$	$r=-0.636$ $p=1.95e-3$	$\rho=-0.675$ $p=1.06e-3$	$r=-0.264$ $p=1.75e-1$	$\rho=-0.238$ $p=2.23e-1$

Table D.3: Correlation coefficients between BMI and the relative volume of gray and white matter ( $\mu_{gw}$ ).

Lobe	$\mu_{gw}$ (both sexes)		$\mu_{gw}$ (men)		$\mu_{gw}$ (women)	
	Pearson	Spearman	Pearson	Spearman	Pearson	Spearman
Left frontal	$r=-0.255$ $p=8.02e-2$	$\rho=-0.266$ $p=6.74e-2$	$r=0.052$ $p=8.32e-1$	$\rho=-0.106$ $p=6.66e-1$	$r=-0.331$ $p=7.97e-2$	$\rho=-0.155$ $p=4.21e-1$
Right frontal	$r=-0.209$ $p=1.54e-1$	$\rho=-0.218$ $p=1.37e-1$	$r=0.150$ $p=5.39e-1$	$\rho=-0.106$ $p=6.66e-1$	$r=-0.292$ $p=1.24e-1$	$\rho=-0.107$ $p=5.80e-1$
Left parietal	$r=-0.129$ $p=3.87e-1$	$\rho=-0.138$ $p=3.56e-1$	$r=0.039$ $p=8.77e-1$	$\rho=-0.067$ $p=7.91e-1$	$r=-0.129$ $p=5.06e-1$	$\rho=-0.059$ $p=7.62e-1$
Right parietal	$r=-0.386$ $p=8.83e-3$	$\rho=-0.374$ $p=1.14e-2$	$r=-0.472$ $p=5.56e-2$	$\rho=-0.367$ $p=1.47e-1$	$r=-0.296$ $p=1.26e-1$	$\rho=-0.265$ $p=1.73e-1$
Left occipital	$r=-0.408$ $p=5.42e-3$	$\rho=-0.325$ $p=2.95e-2$	$r=0.148$ $p=5.57e-1$	$\rho=0.094$ $p=7.11e-1$	$r=-0.596$ $p=1.04e-3$	$\rho=-0.414$ $p=3.20e-2$
Right occipital	$r=-0.368$ $p=1.00e-2$	$\rho=-0.289$ $p=4.62e-2$	$r=0.041$ $p=8.66e-1$	$\rho=0.099$ $p=6.88e-1$	$r=-0.424$ $p=2.18e-2$	$\rho=-0.286$ $p=1.33e-1$
Left temporal	$r=-0.261$ $p=7.37e-2$	$\rho=-0.284$ $p=5.06e-2$	$r=0.000$ $p=1.00e+0$	$\rho=0.008$ $p=9.74e-1$	$r=-0.476$ $p=9.11e-3$	$\rho=-0.536$ $p=2.74e-3$
Right temporal	$r=-0.524$ $p=1.84e-4$	$\rho=-0.487$ $p=6.07e-4$	$r=-0.419$ $p=8.37e-2$	$\rho=-0.465$ $p=5.20e-2$	$r=-0.541$ $p=2.98e-3$	$\rho=-0.469$ $p=1.17e-2$

Table D.4: Correlation coefficients between the Stroop test (form2) and the relative volume of gray and white matter ( $\mu_{gw}$ ).



Lobe	$\mu_{gw}$ (both sexes)		$\mu_{gw}$ (men)		$\mu_{gw}$ (women)	
	Pearson	Spearman	Pearson	Spearman	Pearson	Spearman
Left frontal	$r=-0.409$ $p=3.92e-3$	$\rho=-0.495$ $p=3.51e-4$	$r=-0.301$ $p=2.11e-1$	$\rho=-0.345$ $p=1.48e-1$	$r=-0.464$ $p=1.13e-2$	$\rho=-0.547$ $p=2.12e-3$
Right frontal	$r=-0.258$ $p=7.37e-2$	$\rho=-0.284$ $p=4.76e-2$	$r=-0.146$ $p=5.40e-1$	$\rho=-0.051$ $p=8.30e-1$	$r=-0.305$ $p=1.08e-1$	$\rho=-0.341$ $p=7.06e-2$
Left parietal	$r=-0.149$ $p=3.08e-1$	$\rho=-0.289$ $p=4.43e-2$	$r=-0.114$ $p=6.33e-1$	$\rho=-0.114$ $p=6.31e-1$	$r=-0.163$ $p=3.98e-1$	$\rho=-0.316$ $p=9.53e-2$
Right parietal	$r=-0.141$ $p=3.39e-1$	$\rho=-0.236$ $p=1.06e-1$	$r=-0.147$ $p=5.36e-1$	$\rho=-0.339$ $p=1.43e-1$	$r=-0.121$ $p=5.39e-1$	$\rho=-0.084$ $p=6.71e-1$
Left occipital	$r=-0.305$ $p=3.31e-2$	$\rho=-0.200$ $p=1.68e-1$	$r=-0.393$ $p=7.80e-2$	$\rho=-0.189$ $p=4.12e-1$	$r=-0.232$ $p=2.34e-1$	$\rho=-0.107$ $p=5.87e-1$
Right occipital	$r=-0.334$ $p=2.85e-2$	$\rho=-0.360$ $p=1.77e-2$	$r=-0.227$ $p=3.65e-1$	$\rho=-0.182$ $p=4.70e-1$	$r=-0.393$ $p=5.22e-2$	$\rho=-0.414$ $p=3.98e-2$
Left temporal	$r=-0.331$ $p=2.17e-2$	$\rho=-0.378$ $p=8.04e-3$	$r=-0.306$ $p=2.02e-1$	$\rho=-0.427$ $p=6.85e-2$	$r=-0.346$ $p=6.59e-2$	$\rho=-0.331$ $p=7.90e-2$
Right temporal	$r=-0.576$ $p=4.23e-5$	$\rho=-0.522$ $p=2.81e-4$	$r=-0.585$ $p=1.36e-2$	$\rho=-0.575$ $p=1.56e-2$	$r=-0.571$ $p=1.87e-3$	$\rho=-0.489$ $p=9.69e-3$

Table D.5: Correlation coefficients between the Trail making (part A) and the relative volume of gray and white matter ( $\mu_{gw}$ ).

Lobe	$\mu_{gw}$ (both sexes)		$\mu_{gw}$ (men)		$\mu_{gw}$ (women)	
	Pearson	Spearman	Pearson	Spearman	Pearson	Spearman
Left frontal	$r=0.168$ $p=2.54e-1$	$\rho=0.199$ $p=1.75e-1$	$r=-0.231$ $p=3.42e-1$	$\rho=-0.247$ $p=3.07e-1$	$r=0.367$ $p=5.94e-2$	$\rho=0.356$ $p=6.83e-2$
Right frontal	$r=0.100$ $p=5.03e-1$	$\rho=0.120$ $p=4.23e-1$	$r=-0.350$ $p=1.42e-1$	$\rho=-0.313$ $p=1.93e-1$	$r=0.321$ $p=9.58e-2$	$\rho=0.319$ $p=9.77e-2$
Left parietal	$r=0.041$ $p=7.89e-1$	$\rho=0.036$ $p=8.14e-1$	$r=-0.010$ $p=9.69e-1$	$\rho=-0.079$ $p=7.56e-1$	$r=0.081$ $p=6.88e-1$	$\rho=0.065$ $p=7.48e-1$
Right parietal	$r=0.071$ $p=6.45e-1$	$\rho=0.052$ $p=7.35e-1$	$r=0.091$ $p=7.20e-1$	$\rho=0.053$ $p=8.35e-1$	$r=0.067$ $p=7.41e-1$	$\rho=0.084$ $p=6.77e-1$
Left occipital	$r=0.174$ $p=2.54e-1$	$\rho=0.108$ $p=4.82e-1$	$r=0.051$ $p=8.40e-1$	$\rho=-0.199$ $p=4.29e-1$	$r=0.318$ $p=1.06e-1$	$\rho=0.243$ $p=2.23e-1$
Right occipital	$r=0.063$ $p=6.82e-1$	$\rho=0.061$ $p=6.88e-1$	$r=0.101$ $p=6.91e-1$	$\rho=-0.085$ $p=7.38e-1$	$r=0.086$ $p=6.70e-1$	$\rho=0.048$ $p=8.12e-1$
Left temporal	$r=0.410$ $p=3.79e-3$	$\rho=0.365$ $p=1.09e-2$	$r=0.317$ $p=1.86e-1$	$\rho=0.132$ $p=5.90e-1$	$r=0.500$ $p=5.78e-3$	$\rho=0.466$ $p=1.07e-2$
Right temporal	$r=0.477$ $p=6.10e-4$	$\rho=0.384$ $p=7.08e-3$	$r=0.382$ $p=1.07e-1$	$\rho=0.217$ $p=3.73e-1$	$r=0.565$ $p=1.42e-3$	$\rho=0.469$ $p=1.02e-2$

Table D.6: Correlation coefficients between verbal fluency (VADAS cog.) and the relative volume of gray and white matter ( $\mu_{gw}$ ).

Lobe	$\mu_{gw}$ (both sexes)		$\mu_{gw}$ (men)		$\mu_{gw}$ (women)	
	Pearson	Spearman	Pearson	Spearman	Pearson	Spearman
Left frontal	$r=0.204$ $p=1.96e-1$	$\rho=0.155$ $p=3.28e-1$	$r=0.193$ $p=4.29e-1$	$\rho=0.154$ $p=5.28e-1$	$r=0.221$ $p=3.11e-1$	$\rho=0.137$ $p=5.32e-1$
Right frontal	$r=0.130$ $p=4.11e-1$	$\rho=0.014$ $p=9.29e-1$	$r=0.089$ $p=7.18e-1$	$\rho=-0.013$ $p=9.57e-1$	$r=0.163$ $p=4.58e-1$	$\rho=0.044$ $p=8.40e-1$
Left parietal	$r=0.276$ $p=5.77e-2$	$\rho=0.197$ $p=1.80e-1$	$r=0.168$ $p=4.91e-1$	$\rho=0.091$ $p=7.10e-1$	$r=0.334$ $p=7.61e-2$	$\rho=0.309$ $p=1.03e-1$
Right parietal	$r=0.256$ $p=7.05e-2$	$\rho=0.229$ $p=1.21e-1$	$r=0.105$ $p=6.60e-1$	$\rho=0.083$ $p=7.26e-1$	$r=0.382$ $p=5.13e-2$	$\rho=0.380$ $p=5.06e-2$
Left occipital	$r=0.224$ $p=1.31e-1$	$\rho=0.152$ $p=3.09e-1$	$r=0.191$ $p=4.19e-1$	$\rho=0.113$ $p=6.36e-1$	$r=0.284$ $p=1.51e-1$	$\rho=0.213$ $p=2.86e-1$
Right occipital	$r=0.146$ $p=3.58e-1$	$\rho=0.124$ $p=4.33e-1$	$r=-0.142$ $p=5.62e-1$	$\rho=-0.196$ $p=4.22e-1$	$r=0.311$ $p=1.48e-1$	$\rho=0.294$ $p=1.74e-1$
Left temporal	$r=0.406$ $p=4.59e-3$	$\rho=0.399$ $p=5.43e-3$	$r=0.289$ $p=2.45e-1$	$\rho=0.154$ $p=5.42e-1$	$r=0.481$ $p=8.27e-3$	$\rho=0.456$ $p=1.29e-2$
Right temporal	$r=0.598$ $p=1.13e-5$	$\rho=0.557$ $p=5.77e-5$	$r=0.562$ $p=1.89e-2$	$\rho=0.382$ $p=1.31e-1$	$r=0.625$ $p=2.88e-4$	$\rho=0.600$ $p=5.84e-4$

Table D.7: Correlation coefficients between walking speed and the relative volume of gray and white matter ( $\mu_{gw}$ ).

## APPENDIX E

# Code listings

---

Listing E.1: areastat.m

```
1 % Script for extracting metrics from registrations
2
3 det=1; %Set to 1 for Jacobian determinants and to 0 for Log-
   Euclidian
4 lobes=1; %Set to 1 for subdivision into lobes and to 0 if LPBA
   zones
5 cross=0; %Set to 1 for cross-sectional and to 0 for longitudinal
6 if cross
7     fdir = 'z:/dofs/inter/gmwm/';
8 else
9     fdir = 'z:/dofs/intra/gmwm/';
10 end
11 files = dir([fdir , 'det\whole\*.mat']);
12 if lobes
13     load z:/atlas_02/lobes.mat
14     brainlabels=lobes;
15     labels=1:8;
16 else
17     load z:/atlas_02/brainlabels.mat
18     load z:/atlas/arealabels.mat
```

```

19 end
20
21 if det
22     mdet = zeros(length(labels),1);
23     stddet = zeros(length(labels),1);
24     meanarea = zeros(length(labels),length(files),1);
25 else
26     mle = zeros([6 length(labels)]);
27     cle = zeros([6 6 length(labels)]);
28     meanarea = zeros(length(labels),length(files),6);
29 end
30
31 for r=1:length(labels)
32     fprintf('%d\n', labels(r))
33     if det
34         labeldatadet = [];
35     else
36         labeldatale = [];
37     end
38     for s=1:length(files)
39         fprintf('%s\n', files(s).name)
40         %load, and anatomical sort the data
41         if det
42             load(strcat(fdir, 'det/whole/', files(s).name))
43             meanarea(r,s)=mean(d(brainlabels==labels(r)));
44             labeldatadet = [labeldatadet; d((brainlabels==labels(r)
45                 )&d~=0)];
46         else
47             load(strcat(fdir, 'le/whole/', files(s).name))
48             labeldataletemp=le(repmat((brainlabels==labels(r))&le
49                 (:,:,1)~=0,[1 1 1 6]));
50             labeldataletemp=reshape(labeldataletemp, length(
51                 labeldataletemp)/6,6);
52             labeldatale = [labeldatale; labeldataletemp];
53             meanarea(r,s,:)=reshape(mean(labeldataletemp),[1 1 6]);
54         end
55     end
56     if det
57         mdet(r) = mean(labeldatadet);
58         stddet(r) = cov(labeldatadet);
59         md = mdet(r);
60         stdd = stddet(r);

```

---

```
58     %save the data
59     if lobes
60         save(sprintf('%sdet/lobes/%03d.mat', fdir, labels(r)), '
            labeldatadet', 'md', 'std');
61     else
62         save(sprintf('%sdet/zones/%03d.mat', fdir, labels(r)), '
            labeldatadet', 'md', 'std');
63     end
64     else
65         mle(:, r) = mean(labeldatale);
66         cle(:, :, r) = cov(labeldatale);
67         ml = mle(:, r);
68         cl = cle(:, :, r);
69         %save the data
70         if lobes
71             save(sprintf('%sdet/lobes/%03d.mat', fdir, labels(r)), '
                labeldatale', 'mle', 'std');
72         else
73             save(sprintf('%sdet/zones/%03d.mat', fdir, labels(r)), '
                labeldatale', 'ml', 'cl');
74         end
75     end
76 end
77 %save the statistics
78 if det
79     save('z:/dofs/intra/gmwm/det/zones/stats.mat', 'mdet', 'stddet',
        'meanarea');
80 else
81     save('z:/dofs/intra/gmwm/le/zones/stats.mat', 'mle', 'cle', '
        meanarea');
82 end
```

Listing E.2: makelestats.m

```

1  %Script for making the probability volumes using Log-Euclidean
    statistics
2
3  %%
4  %Make the distribution of Log-Euclidean
5  files = dir('z:\dofs\intra\gmwm\le\whole\*.mat');
6  les=[];
7  for i=1:length(files)
8      fprintf('%d ',i)
9      load(['z:\dofs\intra\gmwm\le\whole\' , files(i).name]) %(from
        le_convert.m)
10     letemp=le(repmat(le(:, :, : , 1)~=0,[1 1 1 6]));
11     letemp=reshape(letemp, length(letemp)/6,6);
12     les=[les; letemp];
13 end
14 fprintf('\n')
15 meanle = mean(les);
16 covle = cov(les);
17
18 %%
19 %Make the distribution of Hotelling's T-square statistics.
20 tsqs=zeros(length(les),1);
21 for i=1:size(les,1)
22     tsqs(i)=(les(i,:) - meanle)/covle*(les(i,:) - meanle)';
23 end
24 meantsq=mean(log(tsqs));
25 stdtsq=std(log(tsqs));
26
27 %%
28 %Transform the Log-Euclidean volume to p-values via Hotelling's T-
    square
29 %statistic
30 %For whole volumes:
31 files = dir('z:\dofs\intra\gmwm\le\whole\*.mat');
32 for f=1:length(files)
33     load(['z:\dofs\intra\gmwm\le\whole\' , files(f).name]) %(from
        le_convert.m)
34     pvol=zeros([75 128 128]);
35     for i=1:size(le,1)
36         for j=1:size(le,2)
37             for k=1:size(le,3)

```

---

```

38         if (le(i,j,k,1)~=0)
39             let=squeeze(le(i,j,k,:));
40             %Calculate T-squared statistics
41             tsq=(let'-meanle)/covle*(let'-meanle)';
42             %Transform into normal distribution
43             Z=(log(tsq)-meantsq)/stdtsq;
44             pvol(i,j,k)=normcdf(Z);
45         end
46     end
47 end
48     fprintf('%d ',i)
49 end
50 fprintf(' \n')
51 save ([ 'z:\dofs\intra\gmwm\le\whole\pvols\' , files(f).name] , 'pvols'
        ')
52 end
53
54 %%
55 %Make the distribution of Hotelling's T-square statistics for
    volumes
56 %subdivided into lobe volumes:
57 %Load the mean and cov of each of the lobe volumes
58 load z:\dofs\intra\gmwm\le\lobes\stats %(from areastats.m)
59 files = dir('z:\dofs\intra\gmwm\le\lobes\*.mat'); %(from areastats.
    m)
60 for f=1:length(files)-1
61     fprintf('%d ',f)
62     load ([ 'z:\dofs\intra\gmwm\le\lobes\' , files(f).name] ) %(from
        le_convert.m)
63     tsqs = zeros(length(labeldatale),1);
64     for i=1:size(labeldatale,1)
65         tsqs(i)=(labeldatale(i,:)'-mle(:,f))'/cle(:, :, f)*(
            labeldatale(i,:)'-mle(:,f));
66     end
67     meantsq(f)=mean(log(tsqs));
68     stdtsq(f)=std(log(tsqs));
69 end
70 fprintf(' \n')
71 save z:\dofs\intra\gmwm\le\lobes\tsqstats meantsq stdtsq
72
73
74 %%

```

```

75 %Transform the Log-Euclidean volume to p-values via Hotelling's T-
    square
76 %statistic.
77 %For volumes subdivided into lobe volumes:
78 %Load the mean and cov of each of the Log-Euclidean lobe volumes
79 load z:\dofs\intra\gmwm\le\lobes\stats %(from areastats.m)
80 %Load the mean and cov of the t-squared distribution of each of the
    lobe volumes
81 save z:\dofs\intra\gmwm\le\lobes\tsqstats
82 %Load the volume containing the position of the eight lobe labels
83 load z:/atlas_02/lobes.mat
84 files = dir('z:\dofs\intra\gmwm\le\whole\*.mat'); %(from le_convert
    .m)
85 for f=1:length(files)
86     load(['z:\dofs\intra\gmwm\le\whole\' , files(f).name]) %(from
        le_convert.m)
87     pvol=zeros([75 128 128]);
88     for i=1:size(le,1)
89         for j=1:size(le,2)
90             for k=1:size(le,3)
91                 if (le(i,j,k,1)&&lobes(i,j,k))
92                     lobe=lobes(i,j,k);
93                     let=squeeze(le(i,j,k,:));
94                     %Calculate T-squared statistics
95                     tsq=(let-mle(:,lobe))'/cle(:, :, lobe)*(let-mle
                        (:,lobe));
96                     %Transform into normal distribution
97                     Z=(log(tsq)-meantsq(lobe))/stdtsq(lobe);
98                     pvol(i,j,k)=normcdf(Z);
99                 end
100             end
101         end
102         fprintf('%d ', i)
103     end
104     fprintf('\n')
105     save(['z:\dofs\intra\gmwm\le\lobes\pvols\' , files(f).name], 'pvol
        ')
106 end
107
108 %%
109 %Make the distribution of Hotelling's T-square statistics for
    volumes

```



---

```

110 %subdivided into LPBA volumes:
111 %Load the mean and cov of each of the LPBA volumes
112 load z:\dofs\intra\gmwm\le\zones\stats %(from areastats.m)
113 files = dir('z:\dofs\intra\gmwm\le\zones\*.mat'); %(from areastats.
    m)
114 for f=1:length(files)-1
115     fprintf('%d ',f)
116     load(['z:\dofs\intra\gmwm\le\zones\' ,files(f).name]) %(from
        le_convert.m)
117     tsqs = zeros(length(labeldatale),1);
118     for i=1:size(labeldatale,1)
119         tsqs(i)=(labeldatale(i,:)'-mle(:,f))'/cle(:, :, f)*(
            labeldatale(i,:)'-mle(:,f));
120     end
121     meansq(f)=mean(log(tsqs));
122     stdtsq(f)=std(log(tsqs));
123 end
124 fprintf('\n')
125 save z:\dofs\intra\gmwm\le\zones\tsqstats meansq stdtsq
126
127 %%
128 %Transform the Log-Euclidean volume to p-values via Hotelling's T-
    square
129 %statistic.
130 %For volumes subdivided into lobe volumes:
131 %Load the mean and cov of each of the Log-Euclidean lobe volumes
132 load z:\dofs\intra\gmwm\le\zones\stats %(from areastats.m)
133 %Load the mean and cov of the t-squared distribution of each of the
    lobe volumes
134 save z:\dofs\intra\gmwm\le\zones\tsqstats
135 %Load the volume containing the position of the 52 LPBA labels
136 load z:/atlas_02/brainlabels.mat
137 %Load a vector containing the index of the 52 LPBA labels
138 load z:/atlas/arealabels.mat
139 files = dir('z:\dofs\intra\gmwm\le\whole\*.mat');
140 for f=1:length(files)
141     load(['z:\dofs\intra\gmwm\le\whole\' ,files(f).name]) %(from
        le_convert.m)
142     pvol=zeros([75 128 128]);
143     for i=1:size(le,1)
144         for j=1:size(le,2)
145             for k=1:size(le,3)

```

```
146         if (le(i,j,k,1)&&brainlabels(i,j,k))
147             bl=labels==brainlabels(i,j,k);
148             let=squeeze(le(i,j,k,:));
149             %Calculate T-squared statistics
150             tsq=(let-mle(:,bl))'/cle(:, :, bl)*(let-mle(:,bl)
                );
151             %Transform into normal distribution
152             Z=(log(tsq)-meantsq(bl))/stdtsq(bl);
153             pvol(i,j,k)=normcdf(Z);
154         end
155     end
156 end
157 fprintf('%d ',i)
158 end
159 fprintf('\n')
160 save(['z:\dofs\intra\gmwm\le\zones\pvols\' , files(f).name], 'pvol
    ')
161 end
```

Listing E.3: dofread.m

```

1 function [affine sz griddelta offset dx dy dz active] = dofread(
    fname)
2 %DOFREAD Read ITK dof file
3 % [affine sz griddelta offset dx dy dz active] = dofread(fname)
4 % fname: Path to .dof file
5 % affine: Struct containing the affine transformation
6 % sz: Size of control point grid
7 % griddelta: Spacing of control points
8 % offset: Offset of control points
9 % dx, dy, dz: Control point displacements in x, y, and z
10 % active: Active control points
11
12 fid = fopen(fname, 'r', 'ieee-be');
13 fseek(fid, 20, 'bof');
14 affsize = fread(fid, 1, 'int32');
15 affine = struct('tx', 0, 'ty', 0, 'tz', 0, ...
16               'rx', 0, 'ry', 0, 'rz', 0, ...
17               'sx', 100, 'sy', 100, 'sz', 100, ...
18               'xx', 0, 'xy', 0, 'xz', 0);
19 fseek(fid, 24, 'bof');
20 affine.tx = fread(fid, 1, 'float64'); affine.ty = fread(fid, 1, '
    float64'); affine.tz = fread(fid, 1, 'float64');
21 affine.rx = fread(fid, 1, 'float64'); affine.ry = fread(fid, 1, '
    float64'); affine.rz = fread(fid, 1, 'float64');
22 if affsize == 12
23     affine.sx = fread(fid, 1, 'float64'); affine.sy = fread(fid, 1,
        'float64'); affine.sz = fread(fid, 1, 'float64');
24     affine.xx = fread(fid, 1, 'float64'); affine.xy = fread(fid, 1,
        'float64'); affine.xz = fread(fid, 1, 'float64');
25 end
26 fseek(fid, 24+8*affsize+8, 'bof');
27 sz = flip1r(fread(fid, 3, 'int32'));
28 fseek(fid, 24+8*affsize+8+60, 'bof');
29 griddelta = fread(fid, 3, 'float64');
30 offset = fread(fid, 3, 'float64');
31 fseek(fid, 24+8*affsize+8+108, 'bof');
32 A = fread(fid, 3*prod(sz), 'float64');
33 perm = [3 2 1];
34 dx = flipdim(permute(reshape(A(1:3:prod(sz)*3-2), sz), perm), 2);
35 dy = flipdim(permute(reshape(A(2:3:prod(sz)*3-1), sz), perm), 2);
36 dz = flipdim(permute(reshape(A(3:3:prod(sz)*3), sz), perm), 2);

```

```
37 A = fread(fid, prod(sz), 'int32');
38 active = flipdim(~permute(reshape(A, sz), perm), 2);
39 sz = fliplr(sz);
40 fclose(fid);
```

Listing E.4: detconvert.m

```

1 function detconvert(dofinter , dofintra , sliceout , szsample , mask ,
   wholeout)
2 %DETCONVERT Convert dof files (from ITK) into relative volumes
3 % detconvert(dofinter , dofintra , sliceout , szsample , mask ,
   wholeout)
4 % dofintra: The cross-sectional registration
5 % dofintra: The longitudinal registration
6 % sliceout: filename for resulting volume in seperate slices
7 % szsample: The sample size (size of resulting volume)
8 % mask: The image mask
9 % wholeout: filename for resulting volume
10
11 % Read the transformations (returns b-spline control point
   displacement vectors)
12 [affineinter szinter griddeltainter offsetinter phixinter phiyinter
   phizinter] = dofread(dofinter);
13 [affineintra szintra griddeltaintra offsetintra phixintra phiyintra
   phizintra] = dofread(dofintra);
14 % Reverse the y-axis
15 phiyinter = -phiyinter;
16 phiyintra = -phiyintra;
17 % The affine transformation matrix
18 aff_mat_inter = spm_matrix([affineinter.tx -affineinter.ty
   affineinter.tz -affineinter.rx/180*pi -affineinter.ry/180*pi -
   affineinter.rz/180*pi affineinter.sx/100 affineinter.sy/100
   affineinter.sz/100 -tan(affineinter.xx*pi/180) tan(affineinter.
   xz*pi/180) -tan(affineinter.xy*pi/180)]);
19
20 % Mesh grid for the control points
21 [x y z] = ndgrid(linspace(0,griddeltainter(1)*(szinter(1)-1),
   szinter(1)),linspace(0,griddeltainter(2)*(szinter(2)-1),szinter
   (2)),linspace(0,griddeltainter(3)*(szinter(3)-1),szinter(3)));
22 phixinter = x + phixinter;
23 phiyinter = y + phiyinter;
24 phizinter = z + phizinter;
25 % Mesh grid for the control points
26 [x y z] = ndgrid(linspace(0,griddeltainter(1)*(szinter(1)-1),
   szsample(1)),linspace(0,griddeltainter(2)*(szinter(2)-1),
   szsample(2)),linspace(0,griddeltainter(3)*(szinter(3)-1),
   szsample(3)));
27 % Convert cross-sectional B-spline control points into actual

```

```

    displacements
28 [dxi dyi dzi] = tbspline3(phixinter , phiyinter , phizinter , x, y, z,
    griddeltainter , [0 0 0]);
29 fprintf('tbspline3c nr. 1\n')
30
31 %Do the affine transformation
32 x2 = reshape(dxi ,szsample)-griddeltainter(1)*(szinter(1)-1)/2;
33 y2 = reshape(dyi ,szsample)-griddeltainter(2)*(szinter(2)-1)/2;
34 z2 = reshape(dzi ,szsample)-griddeltainter(3)*(szinter(3)-1)/2;
35 for r=1:szsample(1)
36     for s=1:szsample(2)
37         for t=1:szsample(3)
38             temp = aff_mat_inter * [x2(r,s,t) y2(r,s,t) z2(r,s,t)
39                                     1]';
40             x2(r,s,t) = temp(1);
41             y2(r,s,t) = temp(2);
42             z2(r,s,t) = temp(3);
43         end
44     end
45 end
46 vec = [griddeltainter(1)*(szinter(1)-1)/2, griddeltainter(2)*
47         (szinter(2)-1)/2, griddeltainter(3)*(szinter(3)-1)/2, 1]';
48 x2 = x2 + vec(1);
49 y2 = y2 + vec(2);
50 z2 = z2 + vec(3);
51
52 % Convert the longitudinal B-spline control points into B-spline
53 % derivatives in atlas space (cross-sectional registered)
54 [adxdx adydx adzdx]=tbspline3(phixintra , phiyintra , phizintra , x2,
55     y2, z2, griddeltaintra , [1 0 0]);
56 fprintf('tbspline3c nr. 2\n')
57 [adxdy adydy adzdy]=tbspline3(phixintra , phiyintra , phizintra , x2,
58     y2, z2, griddeltaintra , [0 1 0]);
59 fprintf('tbspline3c nr. 3\n')
60 [adxdz adydz adzdz]=tbspline3(phixintra , phiyintra , phizintra , x2,
61     y2, z2, griddeltaintra , [0 0 1]);
62 fprintf('tbspline3c nr. 4\n')
63
64 dxdx = reshape(adxdx , szsample)/griddeltaintra(1)+1;
65 dxdy = reshape(adxdy , szsample)/griddeltaintra(1);
66 dxdz = reshape(adxdz , szsample)/griddeltaintra(1);
67 dydx = reshape(adydx , szsample)/griddeltaintra(2);

```

---

```

63 dydy = reshape(adydy, szsample)/griddeltaintra(2)+1;
64 dydz = reshape(adydz, szsample)/griddeltaintra(2);
65 dzdx = reshape(adzdx, szsample)/griddeltaintra(3);
66 dzdy = reshape(adzdy, szsample)/griddeltaintra(3);
67 dzdz = reshape(adzdz, szsample)/griddeltaintra(3)+1;
68 d = zeros(szsample);
69 for r=1:szsample(1)
70     fprintf('%d\n',r)
71     for s=1:szsample(2)
72         for t=1:szsample(3)
73             % The Jacobian matrix
74             temp = [dxdx(r,s,t) dxdy(r,s,t) dxdz(r,s,t); ...
75                   dydx(r,s,t) dydy(r,s,t) dydz(r,s,t); ...
76                   dzdx(r,s,t) dzdy(r,s,t) dzdz(r,s,t)];
77             d(r,s,t)=det(temp);
78         end
79     end
80     d(r, :, :) = d(r, :, :) .* mask(r, :, :);
81     if ~isempty(sliceout)
82         d2 = d(r, :, :);
83         save(sprintf('%02s_%03d.mat',matout,r), 'd2');
84     end
85 end
86 if ~isempty(wholeout)
87     save(wholeout, 'd');
88 end

```

## Listing E.5: leconvert.m

```

1 function leconvert(dofinter , dofintra , sliceout , szsample , mask ,
   wholeout)
2 %LECONVERT Convert dof files (from ITK) into Log-Euclidean
   volumes
3 % le_convert(dofinter , dofintra , sliceout , szsample , mask ,
   wholeout)
4 % dofinter: The cross-sectional registration
5 % dofintra: The longitudinal registration
6 % sliceout: filename for resulting volume in seperate slices
7 % szsample: The sample size (size of resulting volume)
8 % mask: The image mask
9 % wholeout: filename for resulting volume
10
11 % Read the transformations (returns b-spline control point
   displacement vectors)
12 [affineinter szinter griddeltainter offsetinter phixinter phiyinter
   phizinter] = dofread(dofinter);
13 [affineintra szintra griddeltaintra offsetintra phixintra phiyintra
   phizintra] = dofread(dofintra);
14 % Reverse the y-axis
15 phiyinter = -phiyinter;
16 phiyintra = -phiyintra;
17 % The affine transformation matrix
18 aff_mat_inter = spm_matrix([affineinter.tx -affineinter.ty
   affineinter.tz -affineinter.rx/180*pi -affineinter.ry/180*pi -
   affineinter.rz/180*pi affineinter.sx/100 affineinter.sy/100
   affineinter.sz/100 -tan(affineinter.xx*pi/180) tan(affineinter.
   xz*pi/180) -tan(affineinter.xy*pi/180)]);
19
20 % Mesh grid for the control points
21 [x y z] = ndgrid(linspace(0,griddeltainter(1)*(szinter(1)-1),
   szinter(1)),linspace(0,griddeltainter(2)*(szinter(2)-1),szinter
   (2)),linspace(0,griddeltainter(3)*(szinter(3)-1),szinter(3)));
22 phixinter = x + phixinter;
23 phiyinter = y + phiyinter;
24 phizinter = z + phizinter;
25 % Mesh grid for the control points
26 [x y z] = ndgrid(linspace(0,griddeltainter(1)*(szinter(1)-1),
   szsample(1)),linspace(0,griddeltainter(2)*(szinter(2)-1),
   szsample(2)),linspace(0,griddeltainter(3)*(szinter(3)-1),
   szsample(3)));

```



---

```

27 % Convert cross-sectional B-spline control points into actual
    displacements
28 [dxi dyi dzi] = tbspline3(phixinter , phiyinter , phizinter , x, y, z,
    griddeltainter , [0 0 0]);
29 fprintf('tbspline3c nr. 1\n')
30
31 %Do the affine transformation
32 x2 = reshape(dxi, szsample)-griddeltainter(1)*(szinter(1)-1)/2;
33 y2 = reshape(dyi, szsample)-griddeltainter(2)*(szinter(2)-1)/2;
34 z2 = reshape(dzi, szsample)-griddeltainter(3)*(szinter(3)-1)/2;
35 for r=1:szsample(1)
36     for s=1:szsample(2)
37         for t=1:szsample(3)
38             temp = aff_mat_inter * [x2(r,s,t) y2(r,s,t) z2(r,s,t)
39                                     1]';
39             x2(r,s,t) = temp(1);
40             y2(r,s,t) = temp(2);
41             z2(r,s,t) = temp(3);
42         end
43     end
44 end
45 vec = [griddeltainter(1)*(szinter(1)-1)/2, griddeltainter(2)*
46         (szinter(2)-1)/2, griddeltainter(3)*(szinter(3)-1)/2, 1]';
46 x2 = x2 + vec(1);
47 y2 = y2 + vec(2);
48 z2 = z2 + vec(3);
49
50 % Convert the longitudinal B-spline control points into B-spline
51 % derivatives in atlas space (cross-sectional registered)
52 [adxdx adydx adzdx]=tbspline3(phixintra , phiyintra , phizintra , x2,
53     y2, z2, griddeltaintra , [1 0 0]);
53 fprintf('tbspline3c nr. 2\n')
54 [adxdy adydy adzdy]=tbspline3(phixintra , phiyintra , phizintra , x2,
55     y2, z2, griddeltaintra , [0 1 0]);
55 fprintf('tbspline3c nr. 3\n')
56 [adxdz adydz adzdz]=tbspline3(phixintra , phiyintra , phizintra , x2,
57     y2, z2, griddeltaintra , [0 0 1]);
57 fprintf('tbspline3c nr. 4\n')
58
59 dxdx = reshape(adxdx, szsample)/griddeltaintra(1)+1;
60 dxdy = reshape(adxdy, szsample)/griddeltaintra(1);
61 dx dz = reshape(adxdz, szsample)/griddeltaintra(1);

```

```

62 dydx = reshape(adydx, szsample)/griddeltaintra(2);
63 dydy = reshape(adydy, szsample)/griddeltaintra(2)+1;
64 dydz = reshape(adydz, szsample)/griddeltaintra(2);
65 dzdx = reshape(adzdx, szsample)/griddeltaintra(3);
66 dzdy = reshape(adzdy, szsample)/griddeltaintra(3);
67 dzdz = reshape(adzdz, szsample)/griddeltaintra(3)+1;
68 le = zeros([szsample 6]);
69 for r=1:szsample(1)
70     fprintf('%d\n',r)
71     for s=1:szsample(2)
72         for t=1:szsample(3)
73             % The Jacobian matrix
74             temp = [dxdx(r,s,t) dxdy(r,s,t) dxdz(r,s,t); ...
75                   dydx(r,s,t) dydy(r,s,t) dydz(r,s,t); ...
76                   dzdx(r,s,t) dzdy(r,s,t) dzdz(r,s,t)];
77             % Transform into Log-Euclidean space
78             temp = logmd(sqrtmd(temp'*temp));
79             le(r, s, t, :) = [temp(1,1) temp(2,2) temp(3,3)...
80                             sqrt(2)*temp(1,2) sqrt(2)*temp(1,3)
81                             sqrt(2)*temp(2,3)];
82         end
83     end
84     le(r, :, :, :) = le(r, :, :, :).*repmat(mask(r, :, :), [1 1 1 6]);
85     if ~isempty(sliceout)
86         le2 = le(r, :, :, :);
87         save(sprintf('%02s_%03d.mat', matout, r), 'le2');
88     end
89 end
90 if ~isempty(wholeout)
91     save(wholeout, 'le');
92 end

```

Listing E.6: tbspline3.m

```

1 function [dx dy dz] = tbspline3(phix, phiy, phiz, x, y, z, delta,
   diff)
2 %TBSPLINE3 Converts tensor B-spline control point grid into b-
   spline mesh
3 % phix, phiy, phiz: B-spline control points in each direction
4 % x, y, z: Grid defining the sample point for the tensor B-spline
   control point grid
5 % delta: Spacing for tensor B-spline control point grid
6 % diff: Vector defining the directions to differentiate in
7 % dx, dy, dz: Tensor B-spline evaluated in x, y, and z
8
9 % Pad the array in order to eliminate boundary effects
10 sz = size(phix);
11 [phix2 phiy2 phiz2] = ndgrid(linspace(-delta(1)*2,delta(1)*(sz(1)
   +1),sz(1)+4),linspace(-delta(2)*2,delta(2)*(sz(2)+1),sz(2)+4),
   linspace(-delta(3)*2,delta(3)*(sz(3)+1),sz(3)+4));
12 phix2(3:end-2,3:end-2,3:end-2)=phix;
13 phiy2(3:end-2,3:end-2,3:end-2)=phiy;
14 phiz2(3:end-2,3:end-2,3:end-2)=phiz;
15 if diff(1)
16     phix = padarray(phix,[2 2 2],0,'both');
17 else
18     phix = phix2;
19 end
20 if diff(2)
21     phiy = padarray(phiy,[2 2 2],0,'both');
22 else
23     phiy = phiy2;
24 end
25 if diff(3)
26     phiz = padarray(phiz,[2 2 2],0,'both');
27 else
28     phiz = phiz2;
29 end
30 % Convert the B-spline control points (C-file)
31 [dx dy dz] = tbspline3c(phix, phiy, phiz, x, y, z, delta, diff);

```

Listing E.7: tbspline3c.c

```

1 #include "mex.h"
2 #include <math.h>
3
4 double B(double, int, int);
5
6 void mexFunction(int nlhs, mxArray *plhs [], int nrhs, const mxArray
    *prhs [])
7 {
8     double *phix, *phiy, *phiz, *x, *y, *z, *delta, *deriv;
9     int *sa, sn, sx, sy, sz, *sphi, sphix, sphiy, sphiz, d1, d2, d3
    , I, J, K;
10    mxArray *resxA, *resyA, *reszA;
11    double *resx, *resy, *resz;
12    int r, s, t, l, m, n, i, j, k, idx1, idx2;
13    double u, v, w, res;
14
15    /*B-spline control points in each direction*/
16    phix = mxGetPr(prhs [0]);
17    phiy = mxGetPr(prhs [1]);
18    phiz = mxGetPr(prhs [2]);
19
20    /*Grid defining the sample point for the tensor B-spline
    control point grid*/
21    x = mxGetPr(prhs [3]);
22    y = mxGetPr(prhs [4]);
23    z = mxGetPr(prhs [5]);
24
25    /*delta: Spacing for tensor B-spline control point grid*/
26    delta = mxGetPr(prhs [6]);
27    /*deriv: Vector defining the directions to differentiate in*/
28    deriv = mxGetPr(prhs [7]);
29    d1 = deriv [0];
30    d2 = deriv [1];
31    d3 = deriv [2];
32
33    /*Number of dimensions in sampling grid*/
34    sn = mxGetNumberOfDimensions(prhs [3]);
35    /*The size of the sampling grid*/
36    sa = mxGetDimensions(prhs [3]);
37    sx = sa [0];
38    sy = sa [1];

```

```

39     sz = sn > 2 ? sa[2] : 1;
40
41     /* Size of tensor B-spline control point grid */
42     sphix = mxGetDimensions(prhs[0]);
43     sphiy = sphix[0];
44     sphiz = sphix[1];
45     sphiz = sphix[2];
46
47     /* Initialize matrices for the result */
48     resxA = mxCreateDoubleMatrix(sx*sy*sz, 1, mxREAL);
49     resyA = mxCreateDoubleMatrix(sx*sy*sz, 1, mxREAL);
50     reszA = mxCreateDoubleMatrix(sx*sy*sz, 1, mxREAL);
51     resx = mxGetPr(resxA);
52     resy = mxGetPr(resyA);
53     resz = mxGetPr(reszA);
54
55     /* Evaluate tensor product B-spline in sample grid */
56     for (r = 0; r < sx; r++)
57     {
58         for (s = 0; s < sy; s++)
59         {
60             for (t = 0; t < sz; t++)
61             {
62                 idx1 = r + s*sx + t*sy*sx; /* Index of sampling
63                                     point */
64                 i = ((int) floor(x[idx1]/delta[0])) - 1;
65                 j = ((int) floor(y[idx1]/delta[1])) - 1;
66                 k = ((int) floor(z[idx1]/delta[2])) - 1;
67                 u = x[idx1]/delta[0] - (i + 1);
68                 v = y[idx1]/delta[1] - (j + 1);
69                 w = z[idx1]/delta[2] - (k + 1);
70                 for (l = 0; l <= 3; l++)
71                 {
72                     I = i + 1;
73                     if (I < -2)
74                     {
75                         I = -2;
76                     }
77                     else if (I >= sphix - 2)
78                     {
79                         I = sphix - 3;
80                     }

```

```

80         for (m = 0; m <= 3; m++)
81         {
82             J = j + m;
83             if (J < -2)
84             {
85                 J = -2;
86             }
87             else if (J >= sphiy - 2)
88             {
89                 J = sphiy - 3;
90             }
91             for (n = 0; n <= 3; n++)
92             {
93                 K = k + n;
94                 if (K < -2)
95                 {
96                     K = -2;
97                 }
98                 else if (K >= sphiz - 2)
99                 {
100                     K = sphiz - 3;
101                 }
102                 /* Tensor product of basis function
103                    values */
104                 res = B(u, l, d1) * B(v, m, d2) * B(w,
105                    n, d3);
106                 idx2 = (I+2) + (J+2)*sphix + (K+2)*
107                    sphiy*sphix;
108                 /* Store the result */
109                 resx[idx1] += (res * phix[idx2]);
110                 resy[idx1] += (res * phiy[idx2]);
111                 resz[idx1] += (res * phiz[idx2]);
112             }
113         }
114     }
115     plhs[0]=resxA;
116     plhs[1]=resyA;
117     plhs[2]=reszA;
118     nlhs=3;

```

---

```
119     return;
120 }
121
122 /* B-spline basis functions */
123 double B(double u, int l, int d)
124 {
125     switch (d)
126     {
127         case 0:
128             switch (l)
129             {
130                 case 0:
131                     return (1-u)*(1-u)*(1-u)/6;
132                 case 1:
133                     return (3*u*u*u - 6*u*u + 4)/6;
134                 case 2:
135                     return (-3*u*u*u + 3*u*u + 3*u + 1)/6;
136                 case 3:
137                     return u*u*u/6;
138             }
139         case 1:
140             switch (l)
141             {
142                 case 0:
143                     return -(1-u)*(1-u)/2;
144                 case 1:
145                     return (9*u*u - 12*u)/6;
146                 case 2:
147                     return (-9*u*u + 6*u + 3)/6;
148                 case 3:
149                     return u*u/2;
150             }
151         case 2:
152             switch (l)
153             {
154                 case 0:
155                     return 1 - u;
156                 case 1:
157                     return 3*u - 2;
158                 case 2:
159                     return -3*u + 1;
160                 case 3:
```

---

```
161             return u;
162         }
163     }
164     mexWarnMsgTxt("Illegal parameters in basis function evaluation.
165                 ");
165     return 0;
166 }
```



Listing E.8: detconvertinter.m

```

1 function detconvertinter(dofinter , sliceout , szsample , mask ,
   wholeout)
2 %DETCONVERTINTER Convert dof files (from ITK) into relative
   volumes
3 % det_convert_inter(dofinter , sliceout , szsample , mask , wholeout)
4 % dofinter: The cross-sectional registration
5 % sliceout: filename for resulting volume in seperate slices
6 % szsample: The sample size (size of resulting volume)
7 % mask: The image mask
8 % wholeout: filename for resulting volume
9
10 % Read the transformation (returns b-spline control point
   displacement vectors)
11 [affineinter szinter griddeltainter offsetinter phixinter phiyinter
   phizinter] = dofread(dofinter);
12 % Reverse the y-axis
13 phiyinter=-phiyinter;
14 % Mesh grid for the control points
15 [x y z]=ndgrid(linspace(0,griddeltainter(1)*(szinter(1)-1),szsample
   (1)),linspace(0,griddeltainter(2)*(szinter(2)-1),szsample(2)),
   linspace(0,griddeltainter(3)*(szinter(3)-1),szsample(3)));
16 % Convert the cross-sectional B-spline control points into B-spline
   derivatives
17 [adxdx adydx adzdx]=tbspline3(phixinter , phiyinter , phizinter , x, y
   , z, griddeltainter , [1 0 0]);
18 fprintf('tbspline3c nr. 1\n')
19 [adxdy adydy adzdy]=tbspline3(phixinter , phiyinter , phizinter , x, y
   , z, griddeltainter , [0 1 0]);
20 fprintf('tbspline3c nr. 2\n')
21 [adxdz adydz adzdz]=tbspline3(phixinter , phiyinter , phizinter , x, y
   , z, griddeltainter , [0 0 1]);
22 fprintf('tbspline3c nr. 3\n')
23
24 adxdx = reshape(adxdx , szsample)/griddeltainter(1)+1;
25 adxdy = reshape(adxdy , szsample)/griddeltainter(1);
26 adxdz = reshape(adxdz , szsample)/griddeltainter(1);
27 adydx = reshape(adydx , szsample)/griddeltainter(2);
28 adydy = reshape(adydy , szsample)/griddeltainter(2)+1;
29 adydz = reshape(adydz , szsample)/griddeltainter(2);
30 adzdx = reshape(adzdx , szsample)/griddeltainter(3);
31 adzdy = reshape(adzdy , szsample)/griddeltainter(3);

```

```

32 adzdz = reshape(adzdz, szsample)/griddeltainter(3)+1;
33 d = zeros(szsample);
34 for r=1:szsample(1)
35     fprintf('%d\n',r)
36     for s=1:szsample(2)
37         for t=1:szsample(3)
38             % The Jacobian matrix
39             temp = det([adxdx(r,s,t) adxdy(r,s,t) adxdz(r,s,t); ...
40                       adydx(r,s,t) adydy(r,s,t) adydz(r,s,t);
41                       ...
42                       adzdx(r,s,t) adzdy(r,s,t) adzdz(r,s,t)
43                       ]);
44             d(r,s,t)=det(temp);
45         end
46     end
47     d(r, :, :) = d(r, :, :) .* mask(r, :, :);
48     if ~isempty(sliceout)
49         d2 = d(r, :, :);
50         save(sprintf('%02s_%03d.mat', sliceout, r), 'd2');
51     end
52 end
53 if ~isempty(wholeout)
54     save(wholeout, 'd');
55 end

```

Listing E.9: leconvertinter.m

```

1 function leconvertinter(dofinter, sliceout, szsample, mask,
   wholeout)
2 %LECONVERTINTER Convert dof files (from ITK) into Log-Euclidean
   volumes
3 % le_convert_inter(dofinter, sliceout, szsample, mask, wholeout)
4 % dofinter: The cross-sectional registration
5 % sliceout: filename for resulting volume in separate slices
6 % szsample: The sample size (size of resulting volume)
7 % mask: The image mask
8 % wholeout: filename for resulting volume
9
10 % Read the transformation (returns b-spline control point
   displacement vectors)
11 [affineinter szinter griddeltainter offsetinter phixinter phiyinter
   phizinter] = dofread(dofinter);
12 % Reverse the y-axis
13 phiyinter=-phiyinter;
14 % Mesh grid for the control points
15 [x y z]=ndgrid(linspace(0,griddeltainter(1)*(szinter(1)-1),szsample
   (1)),linspace(0,griddeltainter(2)*(szinter(2)-1),szsample(2)),
   linspace(0,griddeltainter(3)*(szinter(3)-1),szsample(3)));
16 % Convert the cross-sectional B-spline control points into B-spline
   derivatives
17 [adxdx adydx adzdx]=tbspline3(phixinter, phiyinter, phizinter, x, y
   , z, griddeltainter, [1 0 0]);
18 fprintf('tbspline3c nr. 1\n')
19 [adxdy adydy adzdy]=tbspline3(phixinter, phiyinter, phizinter, x, y
   , z, griddeltainter, [0 1 0]);
20 fprintf('tbspline3c nr. 2\n')
21 [adxdz adydz adzdz]=tbspline3(phixinter, phiyinter, phizinter, x, y
   , z, griddeltainter, [0 0 1]);
22 fprintf('tbspline3c nr. 3\n')
23
24 adxdx = reshape(adxdx, szsample)/griddeltainter(1)+1;
25 adxdy = reshape(adxdy, szsample)/griddeltainter(1);
26 adxdz = reshape(adxdz, szsample)/griddeltainter(1);
27 adydx = reshape(adydx, szsample)/griddeltainter(2);
28 adydy = reshape(adydy, szsample)/griddeltainter(2)+1;
29 adydz = reshape(adydz, szsample)/griddeltainter(2);
30 adzdx = reshape(adzdx, szsample)/griddeltainter(3);
31 adzdy = reshape(adzdy, szsample)/griddeltainter(3);

```

```

32 adzdz = reshape(adzdz, szsample)/griddeltainter(3)+1;
33
34 le = zeros([szsample 6]);
35 for r=1:szsample(1)
36     fprintf('%d\n',r)
37     for s=1:szsample(2)
38         for t=1:szsample(3)
39             % The Jacobian matrix
40             temp = [adxdx(r,s,t) adxdy(r,s,t) adxdz(r,s,t); ...
41                   adydx(r,s,t) adydy(r,s,t) adydz(r,s,t); ...
42                   adzdx(r,s,t) adzdy(r,s,t) adzdz(r,s,t)];
43             temp = logmd(sqrtmd(temp'*temp));
44             % Transform into Log-Euclidean space
45             le(r, s, t, :) = [temp(1,1) temp(2,2) temp(3,3) temp
46                             (1,2) temp(1,3) temp(2,3)];
47         end
48     end
49     le(r, :, :, :) = le(r, :, :, :).*repmat(mask(r, :, :), [1 1 1 6]);
50     if ~isempty(sliceout)
51         le2 = le(r, :, :, :);
52         save(sprintf('%02s_%03d.mat', sliceout, r), 'le2');
53     end
54 end
55 if ~isempty(wholeout)
56     save(wholeout, 'le');
57 end

```

## Listing E.10: logmd.m

```
1 function L = logmd(M)
2 % L = logmd(M)
3 % Matrix logarithm of a diagonalizable matrix M.
4 [v d] = eig(M);
5 L = v*diag(log(diag(d)))/v;
```

## Listing E.11: sqrtmd.m

```
1 function S = sqrtmd(M)
2 % S = sqrtmd(M)
3 % Matrix square root of a diagonalizable matrix M.
4 [v d] = eig(M);
5 S = v*diag(sqrt(diag(d)))/v;
```

Listing E.12: makemanovaanalysis.m

```

1 load data/malefemale.mat
2 load data/leftright.mat
3 load data/fazekas.mat
4 load pareas
5 areavols = areavols(:,2:end-2); % Remove removed areas
6 [p s l] = princomp(areavols); % Perform principal component
   analysis
7 lcum = cumsum(1)/max(cumsum(1));
8 % Find principal components where at least 95% variance is
   explained
9 maxcomp = find(lcum > .8, 1);
10 % Project data onto the chosen principal components
11 varimaxed = areavols * p(:,1:maxcomp);
12 % Perform MANOVA male/female
13 [dmf pmf statsmf] = manoval(varimaxed, M);
14 % Perform MANOVA right/left/both-handed
15 [drlb prlb statsrlb] = manoval(varimaxed, L + R*2 + B*3);
16 % Perform MANOVA 1/2/3 Fazekas score
17 [dfaz pfaz statsfaz] = manoval(varimaxed, faz);
18
19 % Plot results
20 figure,hold on
21 plot(statsmf.canon(M,1),statsmf.canon(M,2),'xb','LineWidth', 2);
22 plot(statsmf.canon(F,1),statsmf.canon(F,2),'or','LineWidth', 2);
23 title('Sex')
24 legend('Male', 'Female')
25 box on
26
27 % Plot results
28 figure,hold on
29 plot(statsrlb.canon(R,1),statsrlb.canon(R,2),'xb','LineWidth', 2);
30 plot(statsrlb.canon(L,1),statsrlb.canon(L,2),'or','LineWidth', 2);
31 plot(statsrlb.canon(B,1),statsrlb.canon(B,2),'*g','LineWidth', 2);
32 title('Handedness')
33 legend('Right', 'Left', 'Both')
34 box on
35
36 % Plot results
37 figure,hold on
38 plot(statsfaz.canon(faz==1,1),statsfaz.canon(faz==1,2),'xb',
   LineWidth', 2);

```

```
39 plot(statsfaz.canon(faz==2,1), statsfaz.canon(faz==2,2), 'or', '  
    LineWidth', 2);  
40 plot(statsfaz.canon(faz==3,1), statsfaz.canon(faz==3,2), '*g', '  
    LineWidth', 2);  
41 title('Fazekas score')  
42 legend('1', '2', '3')  
43 box on
```





# Bibliography

---

- [1] Joseph P. Hornak. The Basics of MRI, <http://www.cis.rit.edu/htbooks/mri/>. 1996–2007.
- [2] *LADIS protocol: Impact of Age-related brain white matter changes on transition to disability in the elderly. Leukoaraiosis And DISability. Call identifier: 1999/C361106. Proposal no: QLRT-2000-00446.*
- [3] Reetta Kälviäinen and Tuuli Salmenperä. *Do recurrent seizures cause neuronal damage? A series of studies with MRI volumetry in adults with partial epilepsy.*, volume 135 of *Progress in Brain Research*, pages 279–295. Elsevier, 2002.
- [4] V. I. Skvortsova, P. A. Slominsky, L. V. Gubskii, E. A. Koltsova, I. M. Shetova, I. A. Platonova, T. I. Tupitsyna, A. V. Khrunin, and S. A. Limborska. Connection between p53 gene Bam HI RFLP polymorphism with the volume of brain infarction in patients with carotid atherothrombotic ischemic stroke. *Restorative Neurology and Neuroscience*, 22(2):81–85, 2004.
- [5] E. H. Aylward, A. M. Codori, P. E. Barta, G. D. Pearlson, G. J. Harris, and J. Brandt. Basal ganglia volume and proximity to onset in presymptomatic Huntington disease. *Archives of Neurology*, 53(12):1293–1296, 1996.
- [6] I. C. Wright, P. K. McGuire, J.-B. Poline, J. M. Travere, R. M. Murray, C. D. Frith, R. S. J. Frackowiak, and K. J. Friston. Gray and white matter density applied to schizophrenia. *NeuroImage*, 2:244–252, 1995.
- [7] John Ashburner and Karl J. Friston. Why voxel-based morphometry should be used. *NeuroImage*, 14:1238–1243, 2001.

- [8] Yasuyuki Taki, Ryoji Goto, Alan Evans, Alex Zijdenbos, Peter Neelin, Jason Lerch, Kazunori Sato, Shuichi Ono, Shigeo Kinomura, Manabu Nakagawa, Motoaki Sugiura, Jobu Watanabe, Ryuta Kawashima, and Hiroshi Fukuda. Voxel-based morphometry of human brain with age and cerebrovascular risk factors. *Neurobiology of Aging*, 25:455–463, 2004.
- [9] Christian Gaser, Igor Nenadic, Bradley R. Buchsbaum, Erin A. Hazlett, and Monte S. Buchsbaum. Deformation-based morphometry and its relation to conventional volumetry of brain lateral ventricles in MRI. *NeuroImage*, 13:1140–1145, 2001.
- [10] David W. Shattuck and Richard M. Leahy. Brainsuite: An automated cortical surface identification tool. *Medical Image Analysis*, 6(2):129–142, 2002.
- [11] Colin Studholme, Derek L. G. Hill, and David J. Hawkes. An overlap invariant entropy measure of 3d medical image alignment. *Pattern Recognition*, 32(1):71–86, 1999.
- [12] Jan Modersitzki. *Numerical Methods for Image Registration*. Oxford University Press, 2004.
- [13] D. Rueckert, L. I. Sonoda, C. Hayes, D. L. G. Hill, M. O. Leach, and D. J. Hawkes. Non-rigid registration using free-form deformations: Application to breast MR images. *IEEE Transactions on Medical Imaging*, 18(8):712–721, 1999.
- [14] Julia A. Schnabel, Daniel Rueckert, Marcel Quist, Jane M. Blackall, Andy D. Castellano-Smith, Thomas Hartkens, Graeme P. Penney, Walter A. Hall, Haiying Liu, Charles L. Truwit, Frans A. Gerritsen, Derek L. G. Hill, and David J. Hawkes. A generic framework for non-rigid registration based on non-uniform multi-level free-form deformations. In *Proceedings of the 4th International Conference on Medical Image Computing and Computer-Assisted Intervention*, pages 573–581, Utrecht, NL, October 2001. MICCAI, Springer-Verlag.
- [15] Jens Gravesen. Differential geometry and design of shape and motion. <http://www2.mat.dtu.dk/education/01243/cagd.pdf>, 2002.
- [16] David R. Forsey and Richard H. Bartels. Hierarchical b-spline refinement. In *SIGGRAPH '88: Proceedings of the 15th annual conference on Computer graphics and interactive techniques*, pages 205–212, New York, NY, USA, 1988. ACM Press.
- [17] Seungyong Lee, George Wolberg, and Sung Yong Shin. Scattered data interpolation with multilevel B-splines. *IEEE Transactions on Visualization and Computer Graphics*, 3(3):228–244, 1997.

- [18] Milan Sonka and J. Michael Fitzpatrick. *Handbook of Medical Imaging*, volume 2. SPIE Press, 2000.
- [19] Jorge Nocedal and Stephen J. Wright. *Numerical Optimization*. Springer, 1999.
- [20] John Ashburner. *Computational Neuroanatomy*. PhD thesis, University College London, 2000.
- [21] Vincent Arsigny, Pierre Fillard, Xavier Pennec, and Nicholas Ayache. Log-Euclidean metrics for fast and simple calculus on diffusion tensors. *Magnetic Resonance in Medicine*, 56(2):411–421, August 2006.
- [22] Natasha Lepore, Caroline A. Brun, Ming-Chang Chiang, Yi-Yu Chou, Rebecca A. Dutton, Kiralee M. Hayashi, Oscar L. Lopez, Howard Aizenstein, Arthur W. Toga, James T. Becker, and Paul M. Thompson. Multivariate statistics of the jacobian matrices in tensor based morphometry and their application to hiv/aids. In *MICCAI (1)*, pages 191–198, 2006.
- [23] Knut Conradsen. *En introduktion til statistik*, volume 2. IMM, DTU, 6th edition, 2003.
- [24] Richard A. Johnson. *Probability and Statistics for Engineers*. Prentice Hall, 6th edition, 2000.
- [25] David W. Shattuck, M. Mirza, V Adisetiyo, C. Hojatkashani, G. Salamon, K. L. Narr, R. A. Poldrack, R. M. Bilder, and A. W. Toga. Construction of a 3d probabilistic atlas of human brain structures. Submitted to *NeuroImage*, Dec. 2006.
- [26] Ming-Chang Chiang, Rebecca A. Dutton, Kiralee M. Hayashi, Oscar L. Lopez, Howard J. Aizenstein, Arthur W. Toga, James T. Becker, and Paul M. Thompson. 3D pattern of brain atrophy in HIV/AIDS visualized using tensor-based morphometry. *NeuroImage*, 34:44–60, 2007.
- [27] Michael A. Paradiso Mark F. Bear, Barry W. Connors. *Neuroscience: Exploring the Brain*. Lippincott Williams and Wilkins, 3. edition, 2001.
- [28] Michio Ono, Stefan Kubik, and Chad D. Abarnathey. *Atlas of the Cerebral Sulci*. Thieme Medical Publishers, New York, March 1990.
- [29] Naftali Raz and Karen M. Rodrigue. Differential aging of the brain: Patterns, cognitive correlates and modifiers. *Neuroscience and Biobehavioral Reviews*, 30(6):730–748, 2006.
- [30] F. Fazekas, J. B. Chawluk, A. Alavi, H. I. Hurtig, and R. A. Zimmerman. MR signal abnormalities at 1.5T in Alzheimer’s dementia and normal aging. *American Journal of Neuroradiology*, 8:421–426, 1987.

- [31] M. P. Lawton and E. M. Brody. Assessment of older people: Self-maintaining and instrumental activities of daily living. *Gerontologist*, 9:179–186, 1969.